



Title	ゲルマニウム中の電子-正孔液体に不純物がかかわるダイナミクス
Author(s)	小川, 憲介
Citation	大阪大学, 1987, 博士論文
Version Type	VoR
URL	<a href="https://hdl.handle.net/11094/1130">https://hdl.handle.net/11094/1130</a>
rights	
Note	

*The University of Osaka Institutional Knowledge Archive : OUKA*

<https://ir.library.osaka-u.ac.jp/>

The University of Osaka

IMPURITY-RELATED DYNAMICS  
ON ELECTRON-HOLE LIQUID  
IN GERMANIUM

by

Kensuke Ogawa

( 1987 )

DISSERTATION IN PHYSICS



THE OSAKA UNIVERSITY  
GRADUATE SCHOOL OF SCIENCE  
TOYONAKA, OSAKA

IMPURITY-RELATED DYNAMICS  
ON ELECTRON-HOLE LIQUID  
IN GERMANIUM

by

Kensuke Ogawa

( 1987 )

## CONTENTS

- §1. Introduction
- §2. Theoretical Backgrounds
  - 2.1. Strain-confinement of the electron-hole liquid
  - 2.2. Magneto-acoustic oscillation of SCEHL
  - 2.3. Thermal expansion of SCEHL
  - 2.4. Photoluminescence lineshape of SCEHL and free excitons
  - 2.5. Drift motion and spatial distribution of e-h droplets
  - 2.6. Rate equations for SCEHL coexisting with free excitons
  - 2.7. Alfvén wave dimensional resonance of SCEHL
- §3. Experimental Procedures
  - 3.1. Samples
  - 3.2. Magneto-acoustic attenuation measurements
  - 3.3. Photoluminescence measurements
  - 3.4. Millimeter waves magneto-absorption measurements
- §4. Experimental Results
  - 4.1. Magneto-acoustic oscillation of SCEHL
  - 4.2. Photoluminescence spectra of SCEHL and excitons
  - 4.3. Spatial distribution of SCEHL, ordinary droplets and excitons
  - 4.4. Time-decay profile of luminescence intensity from SCEHL in pure Ge
  - 4.5. Free-exciton capture rate by neutral impurities
  - 4.6. Impurity effects on recombination process in SCEHL
  - 4.7. Transient behavior of Alfvén wave dimensional resonance of SCEHL
  - 4.8. Temperature dependence of the AWDR

## §5. Discussion

5.1. Impurity-induced recombination in SCEHL

5.2. Scattering by impurities in SCEHL

5.3. Mott's criterion for ionization of an impurity in  
SCEHL

## §6. Conclusion

Acknowledgements

References

Figure Captions

Figures

Tables

## Abstract

Dynamical properties of impurities in electron-hole liquid in Ge are studied in transport and recombination phenomena. Impurities embedded in the electron-hole liquid are expected to play an important role in scattering and recombination process for electrons and holes in the e-h liquid. By inhomogeneously compressing a Ge specimen, a giant size strain-confined electron-hole liquid (SCEHL) is produced on photoexcitation.

Three kinds of acceptor impurities, In, Be and Zn are studied. Indium impurity forms a hydrogenic shallow-level well-described by the effective mass approximation. Beryllium and Zn impurities are double acceptors, having deep-levels. These impurities have been pictured by a helium-like model, of which natures have not been so well-known as shallow-level impurities. Direct comparison on impurity-induced effects on SCEHL properties is possible between shallow and deep acceptors.

Impurity-induced recombination in SCEHL is monitored by time-resolved photoluminescence experiments. Alfvén wave dimensional resonance experiments using circular- or linear-polarized millimeter waves provide an observation of impurity-induced scattering. Deep acceptors Be and Zn are found to increase the scattering and the recombination in SCEHL drastically. Effects of the shallow acceptor, In, on the other hand, are found really small.

Difference between deep and shallow impurities is qualitatively predictable from the Mott criterion for ionization of impurities. The orbital radius of Be or Zn double acceptor is

smaller than the average distance of e-h pairs in SCEHL so that carriers will see quite deep or high potentials due to these impurities. The Bohr radius of In acceptor meanwhile is nearly equal to the average distance of e-h pairs, so that the potential of In impurity is screened.

Before observing the impurity effects, the properties of SCEHL in pure Ge are examined by magneto-acoustic measurements. Quantum oscillations inherent to Fermi liquid are observed in magneto-acoustic attenuation by SCEHL. From the oscillations, scattering is found to be dominated by carrier-carrier interaction within SCEHL in pure Ge. The e-h pair density decreases with increasing temperature on account of the thermal expansion of SCEHL. The density shows a considerable increase in strong magnetic fields.

In addition, transport of ordinary e-h droplets is investigated by spatial resolution experiments for steady-state luminescence from the droplets. Spatial distribution profiles of free and bound excitons are also presented.

## §1. Introduction

At low temperatures, non-equilibrium electrons and holes excited in a semiconductor can be bound into a hydrogenic state, called an exciton.<sup>1)</sup> In an elemental semiconductor such as Si or Ge, this bound state extends over thirty times of the lattice distance or so, owing to a large dielectric constant and small effective masses of electrons and holes. The binding energy of an exciton is about 4 meV in Ge or about 15 meV in Si.<sup>3)</sup> Silicon and germanium are indirect-gap semiconductors. The electron-hole recombination requires participation of a momentum-conserving phonon. Then, the lifetime of excitons becomes relatively long up to an order of microseconds. High densities of excitons can be generated in those semiconductors using an intense light source.

In 1968, Keldysh proposed that excitons condense into a metallic phase forming compensated drops at a certain density.<sup>4)</sup> His proposal was based on the photoconductivity measurement by Asnin and Rogachev for Ge at 4.2 K with varying optical excitation power.<sup>5)</sup> In their experiment, photoconductivity showed a plateau around exciton densities  $\sim 10^{16} \text{ cm}^{-3}$ , which was regarded as a sign of nucleation of metallic drops. The subsequent work by Pokrovskii and Svistunova supported Keldysh's idea.<sup>6)</sup> They measured photoluminescence spectra of Ge at various temperatures, observed a new line at a spectral energy lower than that of excitons and found the onset temperature for the new line. Since then, a great deal of works have been devoted to the new metallic phase, today well-known as electron-hole liquid or electron-hole

drops. Several reviews have been presented.<sup>7-10)</sup>

Electron-hole liquid is a Fermi liquid having Fermi energies of a few millielectron volts for electrons and holes in Ge.<sup>7)</sup> Quite different from usual Fermi liquid like that for electrons in a metal, e-h liquid is a non-equilibrium plasma. When the excitation source is switched off, it decays with a typical lifetime of 40  $\mu$ s in Ge.<sup>11)</sup> This liquid makes a good system for studying intrinsic features of the Fermi liquid because of the following reasons. Recent marvellous development of materials control enables us to obtain such ultra-high pure semiconductors, in which we can examine properties of the liquid practically free from any disturbance by impurities. The liquid in an elemental semiconductor has nothing to do with positive ions. Owing to a small Fermi energy, the quantum limit is easily achieved and experiments under this condition are possible. The liquid has many attractive aspects, which cannot be seen in any other Fermi liquid.

Theoretical evidence for liquid condensation was presented by calculations of the ground state energy of the e-h plasma.<sup>12-15)</sup> The ground state energy per e-h pair is expressed as an addition of kinetic, exchange and correlation interaction energies of electrons and holes. Fortunately, the level degeneracy at conduction band minima in Si and Ge reduces the kinetic energy. The liquid state is found more stable than the exciton state. It is characterized by the so-called work function—the relevant energy difference, or the binding energy of the liquid.

A lot of experimental methods have been employed to investi-

gate the excitonic condensation and properties of e-h drops. Drop radius has been measured by means of light scattering experiment,<sup>16)</sup> typically to be  $\sim 5 \mu\text{m}$  in Ge. Photoluminescence spectroscopy has been widely used to get information of the e-h density,<sup>7)</sup> work function,<sup>7)</sup> transport,<sup>17-19)</sup> nucleation<sup>7,20,21)</sup> and recombination in the drop.<sup>7,22)</sup> In Ge, the e-h density is  $2.2 \times 10^{17} \text{ cm}^{-3}$  and the work function is 1.7 meV. Far-infrared magneto-plasma resonance technique has given knowledge on plasma modes and transport properties within the drop.<sup>23-25)</sup> Transport of carriers in the drops has also been studied by techniques of acoustic attenuation by drops<sup>26,27)</sup> and time-of-flight detection of phonon pulses.<sup>28)</sup> Kinetics based on the cyclotron resonance of electrons coexisting with drops has also been discussed.<sup>29,30)</sup>

One of the remarkable phenomena characteristic of charged carriers in Fermi liquid is the quantum oscillation under magnetic fields, caused by Landau levels crossing the Fermi level. A typical example of the quantum oscillation is the de Haas-van Alphen effect in a metal. We can observe such an oscillation in the e-h liquid. Oscillation in magneto-luminescence intensity,<sup>31)</sup> and linewidth<sup>32)</sup>, as well as far-infrared magneto-absorption intensity<sup>33)</sup>, have been investigated for e-h drops in Ge. Intensity oscillation in magneto-acoustic attenuation by a giant size e-h drop in strained Ge has been another remarkable topic of the quantum oscillation.

It was in 1974, when a giant electron-hole liquid was caught by Alfvén wave dimensional resonance in an inhomogeneously strained Ge crystal. That was a kind of resonant absorption of

millimeter electromagnetic waves in standing wave conditions within a liquid sphere.<sup>35)</sup> Compressional strain along a  $\langle 111 \rangle$  type direction lowers one of the four conduction band minima and lifts the rest. The bottom of the valence band is also lifted—that is to say, the hole energy is decreased through the deformation potential coupling.<sup>36)</sup> Electrons favor to get populated in the single valley that is energetically lower than three others in the compressed Ge crystal. When the strain is spatially non-uniform, a potential well is formed around the strain-maximum point. Photoexcited carriers migrate to the well and a strain-confined electron-hole liquid (SCEHL) is generated in the well. Its spatial profile can be presented in a display of the infrared vidicon image. The image detection is made by monitoring recombination luminescence from SCEHL.<sup>37)</sup> The radius of SCEHL amounts to  $\sim 400 \mu\text{m}$  in high-strain condition.<sup>38)</sup> Vidicon images of SCEHL taken at our laboratory are shown in Fig. 1. Single valley population of electrons reduces the density of states in the conduction band and raises the kinetic energy. Consequently, the e-h density in SCEHL decreases to  $\sim 6 \times 10^{16} \text{ cm}^{-3}$  in Ge.<sup>38)</sup> Decrease in the density decelerates e-h recombination in SCEHL and the lifetime of SCEHL is prolonged, reaching  $\sim 500 \mu\text{s}$ .<sup>38)</sup> As pointed out by Nozieres,<sup>39)</sup> SCEHL has an advantage that just one drop exists in the sample so that there is no such complication as arising from fluctuation in size and distribution of drops.

After the discovery of SCEHL in Ge, many works have been done to clarify its physical properties. Potential shape investigation of the strain well as well as the condition of

space-confinement of the liquid have been made in detail.<sup>40)</sup> One has been able to determine strain dependence of the e-h pair density and the drop lifetime. Spatial resolution of photoluminescences spectra from SCEHL has also been performed.<sup>38)</sup> Quantum oscillation in the magneto-acoustic attenuation has been demonstrated and the Fermi level has been determined.<sup>34)</sup> Dynamical properties of SCEHL and atmospheric excitons surrounding SCEHL have been investigated by millimeter and submillimeter waves in magneto-absorption measurements.<sup>41,42)</sup> Spatial distribution of electrons and holes around SCEHL has been clarified by millimeter waves cyclotron resonance experiments.<sup>43)</sup>

Based on the well-studied properties of e-h drops in a pure sample, we can step into the impurity effect on the e-h drop in a doped material. Interaction of impurities with a Fermi liquid raises a basic interest like the Kondo effect in a metal.<sup>†</sup> It should be stressed that the e-h liquid in Si or Ge is the best material for studying the interaction, since in no other substances such a well-controlled doping as achieved in Si and Ge is possible.

Effects of impurities and defects on drops have been studied by a number of authors both experimentally<sup>44-62)</sup> and theoretically.<sup>63-68)</sup> Excitonic condensation<sup>44-47)</sup> and spectral lineshape<sup>48-51)</sup> have been examined in Si and Ge. Results ob-

---

<sup>†</sup>For a general review of the Kondo effect, see J. Kondo: Solid State Physics 23 (1969) p.183.

tained do not necessarily agree with each other. Recombination lifetime of drops in Ge doped with shallow impurities has been found unchanged compared with that in undoped Ge.<sup>52,53)</sup> Valley-to-valley transfer of electrons in the drop in Si under uniaxial stress has been studied. Transfer probability due to phosphorus impurities is available.<sup>54)</sup> It has been said that e-h drops are negatively charged. That is due to a difference in probability of non-radiative recombination when becoming a state to have an extra electron or hole.<sup>55)</sup> In the presence of dopants, the sign of the drop charge is dominated by conductive type of dopants, either donors or acceptors.<sup>69)</sup> Enlarged drop radius has been reported in shallow-donor-doped Ge.<sup>56)</sup> Effect of defects and dislocation on the nucleation of e-h drops is also discussed.<sup>21,57,58)</sup> A special theoretical concern has been about the impurity effect on the ground state properties of the liquid.<sup>63-67)</sup> Impurity scattering within the drop has so far been studied <sup>68)</sup> only in connection with the intervalley transfer.<sup>54)</sup>

Most of the experimental works are concerned with photoluminescence and dealing with shallow impurities. No noticeable effects have been observed. In case of deep-level impurities, practically nothing was known for long. Only recently, attempts have been made to study the effect of deep impurities.<sup>59-62)</sup> A drastic lifetime shortening of the drop is found by means of transient measurements of photoluminescence.<sup>59,60)</sup> Anomaly in Alfvén wave dimensional resonance of SCEHL in Ge doped with deep impurities shows up.<sup>61)</sup> Suppression of drop movement by deep

impurities has also been observed.<sup>62)</sup>

In this work, impurity effects on e-h drops in Ge are studied using photoluminescence and magneto-absorption techniques. More emphasis will be put on SCEHL because of the above-mentioned reasons. As dopants, Be, Zn and In impurities are chosen. All of them make substitutional impurities in Ge. Beryllium and zinc are double acceptors. The former has level energies of 24.77, 24.87 meV ( $\text{Be}^0$ ) and 58.02 meV ( $\text{Be}^-$ ),<sup>70)</sup> while the latter 32.98 meV ( $\text{Zn}^0$ )<sup>71)</sup> and 86.514 meV ( $\text{Zn}^-$ ).<sup>72)</sup> These are deeper than the ground level of In, that is 11.2 meV.<sup>73)</sup> Latest works report that free excitons can be bound by these deep impurities. Either bound single excitons (BE) or bound double excitons can be formed.<sup>74-76)</sup> A positively charged acceptor, called  $\text{A}^+$ -center has also been discovered in Be or Zn-doped Ge.<sup>77,78)</sup> This is a bound state of an additional hole around a neutral acceptor. The deep impurities are, thus, found to act strongly on electronic states. In case of SCEHL in Zn-doped Ge, it has been observed that e-h recombination and carrier scattering are enhanced by Zn impurities.<sup>59,61)</sup> Deep impurities Be and Zn embedded in SCEHL in Ge are studied on the basis of transport and recombination phenomena, and compared with shallow impurities like In. Linewidth of the Alfvén wave dimensional resonance gives information of the carrier scattering within SCEHL. From the temperature dependence of luminescence duration, recombination dynamics in SCEHL can also be discussed. By these two independent measurements, profiles of impurities in SCEHL will be clarified. Before going into these procedures, the

properties of SCEHL in pure Ge are examined further in detail by magneto-acoustic techniques.<sup>34,79)</sup> That is to make any impurity-induced effect distinct as much as possible. Magneto-acoustic oscillation due to SCEHL in In-doped Ge is then observed. In Be or Zn-doped Ge, however, the oscillation is not found, probably due to large damping by the deep impurities.

In section 2, basic theories and models are reviewed. In section 3, samples and experimental set-ups are described. Experimental data and analyzed results are presented in section 4 and discussed further in section 5. Conclusion and future perspective are mentioned in section 6.

## §2. Theoretical Backgrounds

### 2.1. Strain-confinement of the electron-hole liquid<sup>36,40,80)</sup>

Mechanical strain introduced in a semiconductor changes the energies of electrons and holes. In many-valley cubic semiconductors the shift of each valley of the conduction band due to strain is written as <sup>81)</sup>

$$\Delta E_c^i = \Xi_d \text{Tr} \hat{\epsilon} + \Xi_u \vec{a}_i \hat{\epsilon} \vec{a}_i, \quad (2-1)$$

where  $\Xi_d$  and  $\Xi_u$  are dilation and shear - deformation potentials,  $\hat{\epsilon}$  is a strain tensor,  $\vec{a}_i$  is a unit vector parallel to the wave vector  $k_i$  extending to the center of the  $i$ -th valley, and  $\text{Tr} \hat{\epsilon}$  can be written as

$$\text{Tr} \hat{\epsilon} = \epsilon_{11} + \epsilon_{22} + \epsilon_{33}. \quad (2-2)$$

In Ge, four valleys in the conduction band lie at the L-points, the Brillouin-zone edges along the  $\langle 111 \rangle$  type directions. Then the index  $i$  runs from 1 to 4, and  $\vec{a}_i$  is taken along four body diagonals in the reciprocal-lattice space. The mean energy shift of valleys can be written

$$\Delta E_c^0 = \left( \Xi_d + \Xi_u / 3 \right) \text{Tr} \hat{\epsilon}. \quad (2-3)$$

The shift of the  $i$ -th valley relative to the mean shift  $\Delta E_c^0$  becomes

$$\Delta E_c^i - \Delta E_c^0 = \Xi_u \epsilon_o^i, \quad (2-4)$$

with

$$\varepsilon_0^i = \vec{a}_i \hat{\varepsilon} \vec{a}_i - \text{Tr} \hat{\varepsilon} / 3 . \quad (2-5)$$

This shift is usually much larger than the mean shift of the conduction and the valence bands.<sup>36)</sup> The sign of  $\hat{\varepsilon}$  is defined plus for a tensile strain and minus for a compressional strain. In  $\langle 111 \rangle$ -strained Ge, the valley parallel to the  $\langle 111 \rangle$  direction goes down in energy, while the rest go up for compression.

The valence bands in Ge have a four-fold degeneracy at the maximum  $\vec{k}=0$ , under no strain application, consisting of two-fold heavy hole bands and two-fold light hole bands. When a stress is applied to Ge, the top of the valence bands splits into two doubly degenerate bands. For a compression, the bands  $M_J = \pm 1/2$  go up and those  $M_J = \pm 3/2$  go down. The shift of the valence band with strain is expressed

$$\Delta E_{\hbar}^{\pm} = a \text{Tr} \hat{\varepsilon} \mp |E_{\varepsilon}| , \quad (2-6)$$

with

$$E_{\varepsilon}^2 = b^2 [(\varepsilon_{11} - \varepsilon_{22})^2 + \text{c.p.}] / 2 + d^2 [\varepsilon_{12}^2 + \text{c.p.}] / 4 , \quad (2-7)$$

where  $a$ ,  $b$  and  $d$  are valence band deformation potentials,<sup>82)</sup> and c.p. stands for cyclic permutation.

The increase of the indirect gap in strained Ge is given by

$$\begin{aligned} E_g^{i,\pm} &= E_g^0 + \Delta E_c^i - \Delta E_{\hbar}^{\pm} \\ &= E_g^0 + \Delta E_g^0 + (\Delta E_c^i - \Delta E_c^0) \pm |E_{\varepsilon}| , \end{aligned} \quad (2-8)$$

with

$$\Delta E_g^0 = \Sigma_d + \Sigma_u / 3 - a. \quad (2-9)$$

The last term  $|E_c|$  in eq.(2-8) is small compared to the third term  $\Delta E_c^i - \Delta E_c^0$ , and can be neglected except for at high-strain condition.<sup>80)</sup> The situation in the present experiment allows us to neglect  $|E_c|$ . We can consider, within SCEHL, electrons are populated in a single valley, while holes in heavy and light hole bands. Deformation potentials in Ge<sup>36)</sup> are tabulated in table 1. Under an inhomogeneous strain such as introduced by a contact of a rod,  $E_q^{i\pm}$  changes spatially. A potential well with decreased band gap is created inside the sample near the contact by a rod. The shape of the well is well approximated by a parabolic potential expressed as  $U(r) = \alpha_S r^2$ , with  $r$  measured from the center of the well.<sup>40)</sup> The coefficient  $\alpha_S$  depends on the magnitude of the strain.

## 2.2. Magneto-acoustic oscillation of SCEHL

Theoretical formulation of magneto-acoustic oscillation of SCEHL in Ge is considered here. Quantum oscillations inherent to a Fermi liquid in magnetic fields have been observed in metals<sup>83,84)</sup> and semimetals<sup>85-89)</sup> using magneto-acoustic methods. Magneto-acoustic oscillation of SCEHL was first demonstrated by Ohyama et al.<sup>34)</sup> They used ultrasonic pulses with a wavelength much smaller than the diameter of SCEHL to observe quantum oscillations with negligible size effect. By using acoustic pulses short compared with the lifetime of SCEHL,

acoustic attenuation by SCEHL can be treated in analogy with that by electrons in a metal. That is essentially like phonon absorption by metallic electrons quantized in Landau levels. The energy of an acoustic phonon excited by an ultrasonic pulse is  $\hbar\omega_q$ . Here  $\omega_q$  is an angular frequency of the ultrasound. In magnetic fields where the quantum oscillation is observed clearly, the energy  $\hbar\omega_q$  is much smaller than the spacing of electron Landau levels. It can be absorbed by an electron in its transition within a Landau level.<sup>79)</sup> This transition takes place with a change in an electron momentum  $\hbar k_z$  along the field direction, like that appearing in a DC longitudinal magneto-resistance.<sup>90)</sup> The acoustic attenuation coefficient due to the transition is written as <sup>91,92)</sup>

$$\alpha = (4\pi / \hbar v_s n_q) \sum_{n, k_z, k'_z} |\langle n, k'_z | H' | n, k_z \rangle|^2 \times [f(E_n(k_z))\{1 - f(E_n(k'_z))\} - f(E_n(k'_z))\{1 - f(E_n(k_z))\}] \times D_{\Gamma_e}(E_n(k_z) - E_n(k'_z) + \hbar\omega_q) \quad (2-10)$$

Here  $v_s$  is the sound velocity,  $n_q$  is the phonon occupation number,  $k_z$  and  $k'_z$  are initial and final wave vector components parallel to the magnetic field, respectively, and  $f(E)$  is the Fermi-Dirac distribution function. The Landau-level broadening  $\Gamma_e$  is taken into consideration and we define

$$D_{\Gamma_e}(E) = \Gamma_e / \pi (E^2 + \Gamma_e^2) \quad (2-11)$$

In the limit of  $\Gamma_e \rightarrow 0$ ,  $D_{\Gamma_e}(E)$  becomes a  $\delta$ -function. Only the

oscillation due to electrons will be considered here. The valence band Landau levels are so much complicated under a strain,<sup>91)</sup> that the magneto-acoustic attenuation by holes seems to contribute merely a constant background.<sup>34,79)</sup> Hamiltonian  $H'$  denotes the electron-phonon interaction through the deformation potential coupling, i.e.,

$$H' = C D_e \sum_{\vec{q}} \{ b_{\vec{q}} \exp(i\vec{q} \cdot \vec{r}) - b_{\vec{q}}^{\dagger} \exp(-i\vec{q} \cdot \vec{r}) \} , \quad (2-12)$$

where  $C$  is a constant,  $D_e$  is the deformation potential for an electron, that can be written as<sup>92)</sup>

$$D_e = \bar{\epsilon}_d + \bar{\epsilon}_u / 3 . \quad (2-13)$$

We denote phonon wave vector  $\vec{q}$ . As usually the case,  $b_{\vec{q}}$  and  $b_{\vec{q}}^{\dagger}$  represent phonon annihilation and creation operators, respectively.

Ultrasonic frequency used in the experiment is ~100 MHz and the energy  $\hbar\omega_{\vec{q}}$  is quite small in comparison with thermal energy  $k_B T$  even at liquid helium temperatures. Only electrons having energy within  $\sim k_B T$  around the Fermi level  $E_{F_e}$  are allowed to take part in the transition. The term related to  $f(E)$  is reduced to

$$\begin{aligned} & f(E_n(k_z)) \{ 1 - f(E_n(k'_z)) \} - f(E_n(k'_z)) \{ 1 - f(E_n(k_z)) \} \\ & = - \hbar\omega_{\vec{q}} \, df(E) / dE . \end{aligned} \quad (2-14)$$

The energy of electron Landau levels is

$$E_n(k_z) = \hbar \omega_c (n + 1/2) + \hbar^2 k_z^2 / 2 m_{\parallel} , \quad (2-15)$$

where

$$\omega_c = e B / m_c c , \quad (2-16)$$

with magnetic field  $B$  and cyclotron mass  $m_c$ , and  $m_{\parallel}$  is an electron translational mass. Density of states  $\rho(E_n(k_z))$  of the Landau levels has an extremum at  $k_z=0$ , diverging as the broadening  $\Gamma_e$  diminishes. Attenuation coefficient  $\alpha$ , accordingly, has a maximum around a field satisfying  $E_{Fe} = E_n(0)$ ; or equivalently, when

$$n + 1/2 = E_{Fe} \cdot m_c c / \hbar e B . \quad (2-17)$$

If the magnetic field is increased, the Landau levels cross the Fermi level in the order of decreasing quantum number  $n$ , and a series of peaks are observed in magneto-acoustic attenuation due to SCEHL. As expected from eq.(2-17), these peaks appear periodic in the inverse of the magnetic field,  $1/B$ . The basic feature expected is shown in Fig. 2.

The matrix element in eq.(2-10) seems to be weakly dependent on the wave vector, and can be taken out of the summation. Expressed in the integral form, eq.(2-10) is reduced to

$$\begin{aligned} \alpha(B) = & (2^{3/2} \pi \omega_c m_{\parallel}^{3/2} |M_g|^2 / \hbar^3 v_s n_g) \\ & \times \int_0^{\infty} dE \left\{ [ \rho_+(E, B) g_+(E) + \rho_-(E, B) g_-(E) ] \right. \\ & \left. \times (df(E)/dE) \right\} . \end{aligned} \quad (2-18)$$

Here  $M_q$  is the matrix element in eq.(2-10),  $\rho_{\pm}(E, B)$  is density of states having the form

$$\rho_{\pm}(E, B) = \left\{ (2m_{//})^{1/2} / 4\pi^2 \hbar^2 \ell_c^2 \right\} \times \sum_n \left[ E + i\Gamma_e - \left\{ (n+1/2)\hbar\omega_c \pm g^* \mu_B B / 2 \right\} \right]^{-1/2}, \quad (2-19)$$

with

$$1/\ell_c^2 = eB/\hbar c, \quad (2-20)$$

and

$$g_{\pm}^*(E) = \sum_{n'} \left[ E + i\Gamma_e - \left\{ (n'+1/2)\hbar\omega_c \pm g^* \mu_B B / 2 \right\} \right]^{1/2}. \quad (2-21)$$

The term  $\pm g^* \mu_B B / 2$  reveals the spin-splitting of the Landau levels and  $g^*$  is the effective g-factor of the conduction bands, or

$$g^* = \left( g_{//}^2 \cos^2 \varphi + g_{\perp}^2 \sin^2 \varphi \right)^{1/2}, \quad (2-22)$$

where the angle  $\varphi$  is measured from the principal axis of the valley with  $g_{//} = 0.87$  and  $g_{\perp} = 1.91$ .<sup>93)</sup> The single valley population of electrons allows definite determinations of translational and cyclotron masses:  $m_{//} = 0.584m_0$  and  $m_c = 0.135m_0$  for  $B//\langle 110 \rangle$ .

In SCEHL, the Fermi energies  $E_{Fe}$ ,  $E_{Fh}$  for electrons and for holes are not very large compared with the thermal energy  $k_B T$ . A careful treatment is needed in carrying out the calculation of eq.(2-18). According to Dingle's approach for the de Haas-van Alphen type susceptibility,<sup>94)</sup>  $df(E)/dE$  is calculated exactly,

and we have

$$\alpha(B) = \alpha(0) [1 + \Phi(B)], \quad (2-23)$$

with

$$\begin{aligned} \Phi(B) = & \left\{ (\hbar\omega_c / E_{Fe})^{1/2} / 2 \right\} \\ & \times \sum_{r=1} \left[ (-1)^r r^{-1/2} \left\{ 2\pi^2 r k_B T / \sinh(2\pi^2 r k_B T / \hbar\omega_c) \right\} \right. \\ & \times \left( \cos \left\{ 2\pi r (E_{Fe} - g^+ \mu_B B/2) / \hbar\omega_c - \pi/4 \right\} \right. \\ & \quad \left. + \cos \left\{ 2\pi r (E_{Fe} + g^+ \mu_B B/2) / \hbar\omega_c - \pi/4 \right\} \right) \\ & \left. \times \exp(-2\pi r \Gamma_e / \hbar\omega_c) \right] . \end{aligned} \quad (2-24)$$

Here  $\alpha(0)$  is the attenuation coefficient in the absence of a magnetic field. Equations (2-23) and (2-24) yield theoretical lineshapes under an assumption that Fermi energies are independent of magnetic field. This assumption is justified in metals having a Fermi energy of  $\sim 1$  eV. In SCEHL, however, Fermi energies are too small, a few meV. The cyclotron energy  $\hbar\omega_c$  is comparable with Fermi energies even at a few tesla. The quantum limit condition that all the carriers are populated in the lowest Landau level can be satisfied at reasonable fields. Effect of magnetic field is, thus, quite strong for SCEHL. Increase in the e-h density with magnetic field, for example, is indeed observed as will be seen in section 4.

### 2.3. Thermal expansion of SCEHL

Thermal expansion as observed for a normal liquid is expected also for SCEHL. The expansion is considered within the

framework of the Landau theory for Fermi liquids.

Let us write the free energy  $F(n,T)$  per an e-h pair as follows:

$$F(n,T) = E_0(n) - TS, \quad (2-25)$$

where  $E_0(n)$  is the total interval energy per pair and  $S$  is the entropy. To express  $E_0(n)$ , it is convenient to replace  $n$  by  $r_s$ , a non-dimensional quantity defined as <sup>95)</sup>

$$r_s = r_0 / a_B^*, \quad (2-26)$$

with the mean distance between e-h pairs,

$$r_0 = (3 / 4\pi n)^{1/3} \quad (2-27)$$

and the exciton Bohr radius,<sup>1)</sup>

$$a_B^* = \kappa \hbar^2 / \mu e^2. \quad (2-28)$$

In eq.(2-28),  $\kappa$  is the dielectric constant of the lattice and  $\mu$  is the reduced mass of an exciton. The total interval energy  $E_0(r_s)$  consists of two terms:

$$E_0(r_s) = E_{kin}(r_s) + E_{xc}(r_s). \quad (2-29)$$

The first term is the kinetic energy of an e-h pair, expressed as

$$E_{\text{kin}}(r_s) = 3(E_{Fe} + E_{Fh})/5$$

$$= 0.468 / r_s^2, \quad (2-30)$$

for Ge.<sup>13)</sup> The second is the exchange and correlation and can be written as the following universal form,<sup>96)</sup>

$$E_{xc}(r_s) = (a + br_s) / (c + dr_s + r_s^2), \quad (2-31)$$

with  $a = -4.8316$ ,  $b = -5.0879$ ,  $c = 0.0152$  and  $d = 3.0426$ . Using  $a_B^* = 127 \text{ \AA}^8$ ) and  $n = 6.5 \times 10^{16} \text{ cm}^{-3}$ ,<sup>79)</sup> we obtain  $r_s = 1.2$  for SCEHL in Ge. For the entropy, a form similar to that for metal, being proportional to temperature  $T$ , is taken, namely,

$$S = \gamma k_B^2 T / 2 \quad (2-32)$$

Equation (2-25) is rewritten, in terms of the e-h density  $n$ , as the following<sup>9)</sup>:

$$F(n, T) = E_0(n) - \gamma(n) (k_B T)^2 / 2, \quad (2-33)$$

with

$$\gamma(n) = (\pi/3n)^{2/3} (m_e + m_h) / \hbar^2 \quad (2-34)$$

Here  $m_e$  and  $m_h$  represent the density-of-state mass of electrons and holes, respectively. The energy  $E_0(n)$  can be expanded about the density at the absolute zero temperature  $n_0$ , to the second

order as

$$E_o(n) = E_o(n_o) + E_o''(n_o) (n - n_o)^2 / 2, \quad (2-35)$$

with

$$E_o''(n_o) = (d^2 E_o / dn^2)_{n=n_o}. \quad (2-36)$$

Substituting eqs. (2-35) and (2-36) in (2-33), we get

$$F(n, T) = E_o(n_o) + E_o''(n_o) (n - n_o)^2 / 2 - r(n) (k_B T)^2 / 2. \quad (2-37)$$

at a finite temperature, the equilibrium pair density  $n(T)$  is determined by minimized  $F(n, T)$  and becomes

$$n(T) = n_o + [\delta'(n) / 2 E_o''(n_o)] (k_B T)^2. \quad (2-38)$$

Here, the density derivative  $r'(n)$  is negative, and  $n(T)$  decreases quadratically with temperature. As seen in section 4, temperature dependence of the density in SCEHL is well fitted by the thermal-expansion term in eq.(2-38). We can define the isothermal compressibility  $K_T$  of SCEHL as

$$K_T = -V^{-1} dV/dp = 1 / [n_o^3 E_o''(n_o)], \quad (2-39)$$

where  $V$  is the volume and  $p$  the pressure of SCEHL.

#### 2.4. Photoluminescence lineshape of SCEHL and free excitons

Photoluminescence from SCEHL occurs when electrons and holes recombine radiatively in SCEHL. The recombination scheme is depicted in Fig. 3. Photon energy  $h\nu$  emitted in the recombination is

$$h\nu = E_G' + \epsilon_e + \epsilon_h, \quad (2-40)$$

where  $E_G'$  is the band gap reduced by the liquid binding energy. At low temperatures, recombination by emitting phonons is dominant. Energies of electrons and holes,  $\epsilon_e$  and  $\epsilon_h$  are measured from the bottom of each band. At the absolute zero temperature, the conduction and valence bands are filled up to the Fermi levels  $E_{Fe}$  and  $E_{Fh}$ . At a finite temperature, occupation in each band is described by the Fermi-Dirac distribution function,  $f(\epsilon_e, E_{Fe})$  or  $f(\epsilon_h, E_{Fh})$ . Luminescence line width from SCEHL is determined by the Fermi levels, since the emitted photon energy lies within the energetic region between  $E_G'$  and  $E_G' + E_{Fe} + E_{Fh}$ . The lineshape is given as a convolution of the densities of states and the distribution functions. Theoretical lineshape of the luminescence from SCEHL is represented as <sup>7,9)</sup>

$$I_{EHL}(h\nu) = I_0 \int_0^\infty d\epsilon_e d\epsilon_h D_e(\epsilon_e) D_h(\epsilon_h) \\ \times f(\epsilon_e, E_{Fe}) f(\epsilon_h, E_{Fh}) \delta(\epsilon_e + \epsilon_h + E_G' - h\nu) \quad (2-41)$$

with the densities of states,

$$D_e(\epsilon_e) = (1/2\pi^2) (2m_e/\hbar^2)^{3/2} \sqrt{\epsilon_e} , \quad (2-42a)$$

for electrons and

$$D_h(\epsilon_h) = (1/2\pi^2) (2m_h/\hbar^2)^{3/2} \sqrt{\epsilon_h} , \quad (2-42b)$$

for holes with the distribution functions,

$$f(\epsilon_e, E_{Fe}) = (1 + \exp[(\epsilon_e - E_{Fe})/k_B T])^{-1} , \quad (2-43a)$$

for electrons and

$$f(\epsilon_h, E_{Fh}) = (1 + \exp[(\epsilon_h - E_{Fh})/k_B T])^{-1} . \quad (2-43b)$$

for holes. Equation (2-41) is reduced to

$$I_{EHL}(h\nu) = I_0' \int_0^{h\nu - E_G'} d\epsilon \sqrt{\epsilon} \sqrt{h\nu - E_G' - \epsilon} \\ \times (1 + \exp[(\epsilon - E_{Fe})/k_B T])^{-1} (1 + \exp[(h\nu - E_G' - \epsilon - E_{Fh})/k_B T])^{-1} \quad (2-44)$$

Fitting eq.(2-44) to the experimental data, we obtain the Fermi energies. From the Fermi energies, the e-h pair density in SCEHL is given by the following relation:

$$n = (1/2\pi^2) (2m_e/\hbar^2)^{3/2} \int_0^\infty d\epsilon \sqrt{\epsilon} (1 + \exp[(\epsilon - E_{Fe})/k_B T])^{-1} \\ = (1/2\pi^2) (2m_h/\hbar^2)^{3/2} \int_0^\infty d\epsilon \sqrt{\epsilon} (1 + \exp[(\epsilon - E_{Fh})/k_B T])^{-1} \quad (2-45)$$

Charge neutrality within SCEHL is assumed here, and the evidence for the charge neutrality is given by observation of the Alfvén wave dimensional resonance characteristic of a compensated plasma. Chemical potential of SCEHL is defined as

$$\mu_{\text{EHL}} = E_G' + E_{Fe} + E_{Fh} \quad . \quad (2-46)$$

Distribution of free exciton is well approximated by a Boltzmann function with the exciton density of states,

$$D_x(\epsilon) = \nu_x \left( m_x^{3/2} / \sqrt{2} \pi^2 \hbar^3 \right) \sqrt{\epsilon} \quad , \quad (2-47)$$

where  $\nu_x$  is the degeneracy of the exciton states and  $m_x$  is the density-of-states mass of excitons. In strained Ge, valley degeneracy in the conduction bands is lifted, and  $\nu_x$  is reduced from 16 in unstrained Ge to 4. The density-of-states masses of electrons and holes are  $m_e = 0.22m_0$  and  $m_h = 0.33m_0$ , respectively.<sup>96)</sup> The mass of a heavy-hole-like exciton is  $0.55m_0$ .<sup>2)</sup> The luminescence lineshape of excitons is denoted as

$$I_x(h\nu) = I_0^x D_x(h\nu - E_G^x) \exp[-(h\nu - E_G^x)/k_B T] \quad , \quad (2-48)$$

with the reduced band gap  $E_G^x$  for excitons. The entire luminescence line shape is the sum of eqs.(2-44) and (2-48). The work function  $\phi$  of SCEHL is given by subtracting  $\mu_{\text{EHL}}$  from  $E_G^x$ , or

$$\phi = E_G^x - \mu_{\text{EHL}} \quad . \quad (2-49)$$

Here,  $E_G'$  and  $E_G^x$  must be measured at luminescence replicas involving the same kind of phonons, since these quantities are actually shifted by an energy lost by emission of phonons.

## 2.5. Drift motion and spatial distribution of e-h droplets

Migration of photoexcited carriers into the strain well generates SCEHL. Since exciton formation and condensation into e-h drops are very rapid process,<sup>7,22)</sup> photoexcited carriers are immediately transformed into free excitons and drops near the illuminated spot of the sample. Spatial resolution measurements of photoluminescence exhibits the distribution of excitons and drops throughout the sample as will be mentioned in section 4. In a doped sample, the distribution of bound excitons is also observed. Migrating flow into the well is, thus, considered to consist mainly of free excitons and e-h droplets. A part of free excitons are captured and lost by impurities to form bound excitons in the course of migration under strain gradients. From the spatial profile of strain-induced motion of excitons and droplets, we can investigate the transport of these systems in a drift motion. A model to derive a drift mobility of e-h droplets is constructed, based on one-dimensional drift equation for droplets.<sup>62)</sup> The model is only valid at such low temperatures that the number of excitons is quite small and the flow is limited by the droplet drift. Photon energy of the excitation light used in the present measurement is much higher than the band-gap energy of Ge. The light is absorbed just near the exposed surface, where e-h drops are created. The droplets in

weakly strained region have almost the same properties as those of ordinary e-h droplets ( $\alpha$ -drops) in a strain-free crystal. It has been confirmed that the flow of  $\alpha$ -drops toward the well is linear in dimension.<sup>97)</sup> In the present experimental scheme, the distance between the excited spot and the center of the well is  $\sim 0.3$  cm. This is larger than the depth from the excited surface to the center of the well,  $\sim 0.07$  cm. Then, a one-dimensional drift model for the motion of  $\alpha$ -drops can be taken along the sample diameter. The strain gradient is assumed constant in the whole sample. The assumption fails as  $\alpha$ -drops approach the well, because the strain potential changes its shape quadratically with distance.<sup>40)</sup> Drift motion of  $\alpha$ -drops is also caused by phonon winds<sup>98)</sup> produced by carrier thermalization around the excited spot. Forces due to phonon winds may be excluded because of a weak contribution at 0.03 cm off the illuminated region.<sup>97)</sup> Spatial profiles of  $\alpha$ -drops in drift and SCEHL are pictured in Fig. 4.

The drift equation for e-h pairs within  $\alpha$ -drops under the strain force  $F$  is

$$\begin{aligned}
 & -v(x)/\tau_{\alpha} - v_{\alpha} \, dv(x)/dx \\
 & + (G_0 / \sqrt{\pi} \beta) \exp [-(x-x_I)^2 / \beta^2] = 0 \quad . \quad (2-50)
 \end{aligned}$$

Here,  $v(x)$  is the number of constituent e-h pairs of  $\alpha$ -drops per unit length at the position  $x$ . The coordinate  $x$  runs along the sample diameter and its origin is taken at the end of the diameter on the opposite side of the strain well. The first term

is the e-h recombination rate in  $\alpha$ -drops with a recombination lifetime  $\tau_{\alpha}$ . The second term represents the drift of e-h pairs characterized by the velocity  $v_d$ . The last term is the effective generation rate of e-h pairs in  $\alpha$ -drops per unit length by the laser beam focussed around  $x = X_I$ . The factor  $G_0$  corresponds to the generation rate integrated over the laser spot. It is supposed that the distribution of e-h pairs around the spot is Gaussian.

Strain-confined EHL is located around  $x = X_S$  with radius  $R$ . When  $\alpha$ -drops reach the surface of SCEHL at  $x = X_S - R$ , they flow into SCEHL. At the surface, the e-h pair distribution in  $\alpha$ -drops determined by eq.(2-50) is associated with that in SCEHL by the following equations:

$$- N_0 / \tau_0 + v_d v(x_S - R) = 0 \quad , \quad (2-51)$$

and

$$N_0 = (4\pi/3) R^3 n \quad . \quad (2-52)$$

Here, SCEHL has the e-h pair density  $n$ , total number of e-h pairs  $N_0$  and lifetime  $\tau_0$ . The first term in eq.(2-51) denotes the e-h recombination in SCEHL and the second term represents the reinforcing flow of  $\alpha$ -drops. Strain-confined EHL grows into a size determined by combining eqs.(2-51) with (2-50). It is assumed that the radiative efficiency of an e-h pair in SCEHL is the same as in  $\alpha$ -drops. This assumption is justified both by the density dependence of the lifetime of SCEHL presented in section

4 and by the work of Betzler et al.<sup>31)</sup> for  $\alpha$ -drops. The luminescence intensity distribution, accordingly, directly reflects the e-h pair distribution. Fitting the equations to the data, the drift velocity of  $\alpha$ -drops is obtained. The drift mobility  $\mu_d$  is given by

$$\mu_d = v_d / F \quad (2-53)$$

The strain force  $F$  acting on an e-h pair can be estimated from the luminescence peak shift  $\Delta E$  of e-h drops over a distance  $\Delta x$ , using the relation<sup>97)</sup>

$$F = \Delta E / \Delta x \quad (2-54)$$

The experimental data for spatial resolution of luminescence from e-h drops at 1.8 K is well explained by the above model. At higher temperatures, however, the drift of excitons has to be included and it is necessary to solve coupled equations for e-h drops and excitons instead of the above equations. The distribution of drops and excitons is observed at 4.2 K and will be discussed later in this thesis.

## 2.6. Rate equations for SCEHL coexisting with free excitons and bound excitons

Time-resolved measurements of photoluminescence from SCEHL and coexisting excitonic systems gives valuable information on e-h

recombination processes in SCEHL. Especially, examining the temperature dependence of the luminescence decay time, one can characterize the recombination process. Approximate solution of rate equations for  $\alpha$ -drops coexisting with free excitons was discussed by several investigators and compared with the photoluminescence data<sup>7)</sup> and with the millimeter waves cyclotron resonance data of electrons around the drops.<sup>29,30)</sup> An exact treatment of the relevant equations and comparison with time-resolved luminescence were first made by Westervelt et al.<sup>22)</sup> However, some complications existed in front of them. Determination of the number of drops was ambiguous. Volume occupied by free excitons was set to be in the cubic power of the exciton diffusion length, using the diffusion constant  $D_x = 1500 \text{ cm}^2 \text{ s}^{-1}$  measured in ref.7, and supposed to be independent of delay time after the excitation photopulse. In case of  $\alpha$ -drops, volume of the cloud occupied by the drops actually expands with the time after the excitation.<sup>97)</sup>

Such complications can be removed in SCEHL. Furthermore, the volume of the excitonic cloud around SCEHL is easily estimated. By means of submillimeter and millimeter waves magneto-absorption technique, dynamics between SCEHL and coexisting excitons has been studied by Ohyama et al.<sup>41,42)</sup> They have found the number of excitons decays with almost the same lifetime as the radial lifetime of SCEHL after the pulsed light excitation. Simple Boltzmann statistics for the excitons around SCEHL in the parabolic potential show that the excitons are also confined in the strain well and exist in a volume of a thin shell

around SCEHL having a thickness of

$$\Delta R = k_B T / 2\alpha_s R, \quad (2-55)$$

where  $\alpha_s$  is the strain coefficient of the parabolic potential described above.<sup>40)</sup> In this model, the density distribution of excitons in the shell decays nearly exponentially as a function of a distance from the surface of SCEHL just like the atmospheric pressure around the earth.<sup>41)</sup> The volume of the shell is shown to be proportional to the radius of SCEHL. Since the exciton density is supposed constant, the decay time of the number of the excitons is governed by the decay of volume. It is experimentally confirmed that the decay time of the excitonic cloud and that of the radius of SCEHL coincide. General forms of the rate equations for SCEHL and free excitons are

$$dV/dt = -V/\tau_0 - \pi R^2 [4A_R T^2 \exp(-\phi/k_B T) - v_x N_x/V_x], \quad (2-56a)$$

and

$$dN_x/dt = -N_x/\tau'_x + \pi R^2 [4A_R T^2 \exp(-\phi/k_B T) - v_x N_x/V_x], \quad (2-56b)$$

where  $N_x$  and  $N_x$  are the total numbers of e-h pairs in SCEHL and in the excitonic cloud, respectively. The volume of the excitonic atmosphere is  $V_x$ , and  $v_x$  is the exciton thermal velocity written as

$$v_x = (8 k_B T / \pi m_x)^{1/2} \quad (2-57)$$

Strain-confined EHL is assumed to have a uniform pair density  $n$  and  $v$  is equal to

$$V = 4\pi R^3 n / 3 \quad (2-58)$$

Each term in the rate equations is depicted in Fig. 5. The first term in eq.(2-56a) is e-h recombination within SCEHL with a lifetime  $\tau_0$ . The term corresponds to the process (1) in Fig. 5. The recombination rate defined as the inverse of the lifetime is given by

$$1/\tau_0 = A + B n + C n^2, \quad (2-59)$$

where  $A$  denotes recombination through impurities or traps,  $Bn$  is radiative recombination and  $Cn^2$  corresponds to nonradiative recombination by passing a recombination energy to an additional electron or hole.<sup>31)</sup> The second terms in eqs.(2-56a) and (2-56b) represent evaporation of free excitons from the surface of SCEHL, having the form of thermionic emission with a Richardson-Dushman coefficient  $A_p$  and a work function  $\phi$ , shown as the process (2) in Fig. 5. The last terms are reverse process of the second terms, known as back flow of free excitons into SCEHL, the process (3) in Fig. 5. In eq.(2-56b), the first term is given as an addition of recombination of free excitons (the process (4) in Fig. 5) and free-exciton capture by neutral impurities (the

process (5)), namely

$$-N_x / \tau_x' = -N_x (1/\tau_x + C_x N_A) \quad (2-60)$$

Here,  $C_x$  is the capture rate of free excitons by neutral impurities<sup>99,100</sup>) and  $N_A$  is a concentration of doped impurities. Free excitons captured by neutral impurities form bound excitons. It is natural to consider impurities are neutralized, since temperature is quite low and a large number of free carriers exist in the excitonic atmosphere. The capture term in eq.(2-60) will actually be  $-C_x(N_A - n_{BX})N_x$  with a density of bound excitons,  $n_{BX}$ . In the luminescence spectra, intensity of the bound exciton line is small, compared with those of SCEHL and free excitons. It is not so unreasonable, accordingly, to replace  $N_A - n_{BX}$  by  $N_A$ . Generation source for excitons is neglected in eq.(2-56b), since the decay behavior is studied, here, after the illumination is cut off.

The volume of the excitonic cloud is calculated from the following equation:

$$\begin{aligned} V_x &= \int_0^{\Delta R} dr \quad 4\pi (R+r)^2 \\ &= 4\pi \left[ R^2 \Delta R + R (\Delta R)^2 + (\Delta R)^3 / 3 \right] \quad (2-61) \end{aligned}$$

The above assumption that the free-exciton density remains unchanged as SCEHL shrinks through several decay channels becomes invalid in solving the rate equations exactly. It is because that a constant density of excitons does not satisfy the rate

equations. Then, the exciton density has to be allowed to depend on delay time. Thickness  $\Delta R$  of the excitonic cloud is estimated by a somewhat different way from that of Ohyama et al.<sup>41)</sup> The way stands, however, on the similar basis to their idea in the aspect that the excitonic atmosphere is treated as an ideal gas having a finite lifetime of free excitons. The thickness is determined by a balance between a drift motion of excitons towards the center of the well and a reverse drift escaping from the well. The up-stream diffusion length  $L_u$  characterizing an upward flow in a constant potential gradient  $F$  is expressed as<sup>101)</sup>

$$L_u = (2k_B T / |F|) \left[ 1 + (1 + 4k_B T / L_p |F|)^{1/2} \right]^{-1} \quad (2-62)$$

Here,  $L_p$  is a diffusion length under zero force. The strain well extends over so a wide distance, that at each point the formula (2-62) may be used with the strain force,

$$\begin{aligned} F &= - \left[ \partial U(r) / \partial r \right]_{r=R} \\ &= - 2\alpha R \end{aligned} \quad (2-63)$$

We then have for the thickness of the cloud

$$\Delta R = (k_B T / \alpha R) \left[ 1 + (1 + 2k_B T / (D_x \tau_x') \alpha R)^{1/2} \right]^{-1}, \quad (2-64)$$

where  $D_x$  is the diffusion coefficient of free excitons, and free excitons, and  $\tau_x'$  is an free-exciton effective lifetime given in eq.(2-60). Impurity effect on exciton transport is considered only for the lifetime  $\tau_x'$  on the supposition that exciton capture

by impurities is dominant, and that exciton scattering by impurities is small. Diffusion coefficient is, thus, set free from impurity effects. Recently, the exciton diffusion coefficient,  $300 \text{ cm}^2/\text{s}$  has been derived from spatial resolution measurements of exciton luminescence in pure Ge at 4.2 K.<sup>102)</sup> In pure Si, temperature dependence of free-exciton transport has been studied and found that exciton mobility  $\mu_x$  is limited by scattering by phonons showing  $T^{-3/2}$  dependence and that Einstein's relation,  $D_x = \mu_x k_B T$ , holds well.<sup>103)</sup> Temperature dependence of  $D_x$  in Si has been found to be  $D_x = 300 T^{-1/2} \text{ cm}^2/\text{s}$ .<sup>103)</sup> Silicon and germanium are quite similar to each other, so that  $T^{-1/2}$  - dependence of  $D_x$  may be available also in Ge. Using the value for  $D_x$  at 4.2 K,<sup>102)</sup> we obtain  $D_x = 614 T^{-1/2} \text{ cm}^2/\text{s}$ .

The capture rate  $C_x$  of free excitons by neutral Zn impurities has been available.<sup>99,100)</sup> No values have been reported, however, for the capture rates by another deep impurity Be and by a shallow impurity In. To obtain the capture rates by these impurities, free-exciton effective lifetime  $\tau_x'$  has to be measured in each sample doped either with Be impurities or with In impurities at such an excitation power that e-h drops may not be created. In this case, the rate equation for free excitons is simply

$$dn_x / dt = - n_x / \tau_x' \quad , \quad (2-65)$$

with the same  $n_x$  and  $\tau_x'$  as in eq.(2-60). Equation (2-65) tells that the decay form of free excitons is exponential in time with an effective lifetime  $\tau_x'$ . Collapse in the bound exciton peak

has been observed under uniaxial stress.<sup>76,104)</sup> The capture rates measured in unstrained Ge samples are used in the rate equations (2-56a) and (2-56b), though capture rates have strain dependence. In a strained sample, SCEHL is formed even under so weak an excitation power that time-resolved measurements are almost impossible. The free-exciton capture rates  $C_x$  is associated with a capture cross section  $\sigma_x$  by the relation

$$C_x = \sigma_x \nu_x \quad (2-66)$$

## 2.7. Alfvén wave dimensional resonance of SCEHL<sup>105-107)</sup>

Electromagnetic waves having a frequency lower than the plasma frequency associated with an interacting conducting medium cannot propagate into the medium. The plasma frequency  $\omega_p$  for a compensated electron-hole plasma is defined as <sup>105)</sup>

$$\omega_p^2 = 4\pi n e^2 / \kappa \mu \quad (2-67)$$

with

$$\mu^{-1} = m_e^{-1} + m_h^{-1} \quad (2-68)$$

For SCEHL in Ge with  $n = 6 \times 10^{16} \text{ cm}^{-3}$ ,  $m_e = 0.22m_0$ ,  $m_h = 0.33m_0$  and  $\kappa = 16$ , we have  $\omega_p/2\pi = 1500 \text{ GHz}$ . In a magnetic field, the dielectric function of a plasma is strongly modified. Low frequency waves can propagate in the plasma when the frequency of the waves is lower than the cyclotron frequency  $\omega_c$ .<sup>105)</sup> In a

single-component plasma such as an electron plasma, only the cyclotron-active circular-polarized waves can propagate. Such waves are called helicon waves. In a two-component plasma having equal numbers of opposite charges, on the other hand, waves with both polarizations can travel. These waves are called Alfvén waves. An example of such a compensated plasma is SCEHL in Ge.

Dispersion relations for propagation of helicon and Alfvén waves will now be considered. Let us start from the equation of motion for a carrier in one-component plasma corresponding to the helicon case. Supposing that the carrier has a scalar mass  $m$  and a momentum relaxation time  $\tau$ , the equation is described as <sup>105)</sup>

$$m \frac{d\vec{v}}{dt} = e(\vec{E} + \vec{v} \times \vec{B} / c) - m\vec{v} / \tau \quad (2-69)$$

where  $c$  is the light velocity, and  $\vec{E}$  and  $\vec{B}$  are the electric field of the electromagnetic waves and the static magnetic field applied to the plasma. These fields can be expressed as

$$\begin{aligned} \vec{E} &= \vec{E}_0 \exp(-i\omega t) \\ &= \begin{bmatrix} E_{x0} \\ E_{y0} \\ E_{z0} \end{bmatrix} \exp(-i\omega t) , \end{aligned} \quad (2-70)$$

and

$$\vec{B} = \begin{bmatrix} 0 \\ 0 \\ B \end{bmatrix} . \quad (2-71)$$

The angular frequency of the helicon waves is  $\omega$ , and the magnetic field is set parallel to z-direction. The solution of eq.(2-69)

has the form  $\vec{v} = \vec{v}_0 \exp(-i\omega t)$ , with  $\vec{v}_0$  given as a function of the electric field. Substituting  $\vec{v}$  into the current formula,

$$\begin{aligned} \vec{j} &= n e \vec{v} \\ &= \hat{\sigma} \vec{E} , \end{aligned} \quad (2-72)$$

we have for the conductivity tensor

$$\hat{\sigma} = \begin{bmatrix} \sigma_1 & \sigma_2 & 0 \\ -\sigma_2 & \sigma_1 & 0 \\ 0 & 0 & \sigma_3 \end{bmatrix} , \quad (2-73)$$

with

$$\left. \begin{aligned} \sigma_1 &= \sigma_0 (1 - i\omega\tau) / [(1 - i\omega\tau)^2 + \omega_c^2 \tau^2] , \\ \sigma_2 &= \sigma_0 \omega_c \tau / [(1 - i\omega\tau)^2 + \omega_c^2 \tau^2] , \end{aligned} \right\} (2-74)$$

and

$$\sigma_3 = \sigma_0 / (1 - i\omega\tau) .$$

Here,  $\sigma_0$  is the DC-conductivity, or

$$\sigma_0 = n e^2 \tau / m , \quad (2-75)$$

with a carrier density  $n$ . In a representation with the basis of circular polarizations, we have

$$\hat{\sigma} = \begin{bmatrix} \sigma_+ & 0 & 0 \\ 0 & \sigma_- & 0 \\ 0 & 0 & \sigma_3 \end{bmatrix} , \quad (2-76)$$

where

$$\begin{aligned} \sigma_{\pm} &= \sigma_1 \pm i\sigma_2 \\ &= \sigma_0 / [1 - i(\omega \mp \omega_c)\tau] \end{aligned}$$

$$= n e^2 \tau / m [1 + (\omega \mp \omega_c)^2 \tau^2] \\ + i n e^2 \tau^2 (\omega \mp \omega_c) / m [1 + (\omega \mp \omega_c)^2 \tau^2] \quad (2-77)$$

In the Faraday configuration that the wave propagation is parallel to the magnetic field, propagation constants  $k_{\pm}$  have the forms,

$$k_{\pm}^2 = (\omega/c)^2 (\kappa - 4\pi \sigma_{\pm} / i \omega) \\ = (\omega/c)^2 \kappa \left( 1 - \omega_p^2 (\omega \mp \omega_c) / \omega [(1/\tau)^2 + (\omega \mp \omega_c)^2] \right. \\ \left. + i \omega_p^2 / \omega \tau [(1/\tau)^2 + (\omega \mp \omega_c)^2] \right) \quad (2-78)$$

with

$$\omega_p^2 = 4\pi n e^2 / \kappa m \quad (2-79)$$

Dispersion relation for dielectric functions  $\epsilon_{\pm}$  in case of helicon waves are as follows:

$$\text{Re}(\epsilon_{\pm}) = \kappa \left( 1 - (\omega \mp \omega_c) \omega_p^2 / \omega [(1/\tau)^2 + (\omega \mp \omega_c)^2] \right) \quad (2-80a)$$

and

$$\text{Im}(\epsilon_{\pm}) = \kappa \omega_p^2 / \omega \tau [(1/\tau)^2 + (\omega \mp \omega_c)^2] \quad (2-80b)$$

In the helicon limit,  $\omega_c \gg \omega$ ,  $1/\tau$ , dielectric constants as a function of the magnetic field can be written as <sup>106)</sup>

$$\text{Re}(\epsilon_{\pm}) = \pm 4\pi n c e / \omega B \quad (2-81a)$$

and

$$I_m(\epsilon_{\pm}) = 4\pi n c^2 m / \omega \tau B^2 \quad (2-81b)$$

It is found, from eq.(2-81a), that right-circular-polarized waves can travel for positive charge, while left-circular-polarized waves can travel for negative charge. Quite similar argument leads to the following dispersion relation for an e-h plasma:<sup>105)</sup>

$$Re(\epsilon_{\pm}) = \kappa \left( 1 - (\omega \mp \omega_{ce}) \frac{\omega_{pe}^2}{\omega} \left[ \frac{1}{\tau_e} \right]^2 + (\omega \mp \omega_{ce})^2 \right] - (\omega \mp \omega_{ch}) \frac{\omega_{ph}^2}{\omega} \left[ \frac{1}{\tau_h} \right]^2 + (\omega \mp \omega_{ch})^2 \right) \quad (2-82a)$$

and

$$I_m(\epsilon_{\pm}) = \kappa \left( \frac{\omega_{pe}^2}{\omega \tau_e} \left[ \frac{1}{\tau_e} \right]^2 + (\omega \mp \omega_{ce})^2 \right) + \frac{\omega_{ph}^2}{\omega \tau_h} \left[ \frac{1}{\tau_h} \right]^2 + (\omega \mp \omega_{ch})^2 \right) \quad (2-82b)$$

In the Alfvén limit,  $\omega_c \gg \omega \gg 1/\tau$ , eq.(2-82a) is reduced to

$$Re(\epsilon_{\pm}) = \pm (\kappa/\omega) \left( \frac{\omega_{pe}^2}{\omega_{ce}} + \frac{\omega_{ph}^2}{\omega_{ch}} \right) + \kappa \left( \frac{\omega_{pe}^2}{\omega_{ce}^2} + \frac{\omega_{ph}^2}{\omega_{ch}^2} \right) \quad (2-83)$$

Here, the first term is to vanish in a compensated plasma where  $n_e = n_h = n$ ; then we have <sup>106)</sup>

$$Re(\epsilon_{\pm}) = 4\pi n c^2 (m_e + m_h) / B^2 \quad (2-84a)$$

The imaginary part is

$$\text{Im}(\epsilon_{\pm}) = 4\pi h c^2 (m_e + m_h) / B^2 \omega \tau_{av} , \quad (2-84b)$$

with

$$\tau_{av} = \tau_e \tau_h (m_e + m_h) / (m_e \tau_h + m_h \tau_e) . \quad (2-85)$$

In SCEHL, electrons are populated in a single valley and the density of light holes is negligible in comparison with that of heavy holes on account of the small mass of light holes. Therefore, SCEHL is regarded as a two-component compensated plasma.<sup>107)</sup>

In the above discussion, boundary conditions have not been taken into consideration. The wavelength of electromagnetic waves changes as a function of magnetic field through the real part of the dielectric function represented in (2-81a) for the helicon case or in (2-84a) for the Alfvén case. When half integral multiples of the wavelength stand in the dimension of the plasma, a power of electromagnetic waves is resonantly absorbed through the imaginary part of the dielectric function in (2-81b) for the helicon waves or in (2-84b) for the Alfvén waves. The dimensional resonance can intuitively be schemed in a slab with a thickness  $d$ . The resonance occurs at wavelengths satisfying the condition,

$$d = N \cdot \lambda / 2 , \quad (2-86)$$

where  $N$  is a positive integer, and  $\lambda$  is a wavelength inside the plasma that can be written, using the wavelength  $\lambda_0$  outside the plasma, as

$$\lambda = \lambda_0 / [\text{Re}(\epsilon_{\pm})]^{1/2}$$

$$= \left\{ \begin{array}{ll} \lambda_0 (\omega B / 4\pi n c e)^{1/2} & : \text{helicon waves} \\ \lambda_0 (B^2 / 4\pi n c^2 (m_e + m_h))^{1/2} & : \text{Alfvén waves} \end{array} \right\} \quad (2-87)$$

combining eq.(2-86) with with eq.(2-87), we have for the size dependence of the resonance fields:

$$B_{\text{res}} \propto \left\{ \begin{array}{ll} d^2 & : \text{helicon waves} \\ d & : \text{Alfvén waves} \end{array} \right\} \quad (2-88)$$

In the case of SCEHL, spherical boundary conditions have to be imposed. Anisotropy of the conduction band in Ge requires a tensorial form for the electron mass.<sup>107)</sup> Then, the calculation of the dimensional resonance of SCEHL becomes too complicated to solve analytically. So a calculation using a spherical mass will be adopted here. In that case the absorbed power  $P$  due to the dimensional resonance in SCEHL can be expressed as<sup>106)</sup>

$$P = (\gamma c^2 / 4\pi) R^3 \omega^2 \tau_{av} (B / B_{Aef})^2 |\vec{H}_{AC}|^2$$

$$/ ( [(B / B_{Aef})^2 - 1]^2 (\omega \tau_{av})^2 + 1 ) \quad (2-89)$$

where  $\vec{H}_{AC}$  is an AC-magnetic field of the waves, and

$$B_{\text{Alf}}^2 = (16\pi/21) (\omega R/c)^2 n (m_e + m_h) . \quad (2-90)$$

Resonance field  $B_{\text{res}}$  is connected with  $B_{\text{Alf}}$  as

$$B_{\text{res}} = B_{\text{Alf}} [ 1 + 1 / (\omega \tau_{\text{av}})^2 ]^{1/4} . \quad (2-91)$$

This equation is valid only in the high field limit, so that deviation from a simple Alfvén scheme arises at lower fields. The deviation comes from difference in mass or in scattering rate between electrons and holes in SCEHL. The situation will be discussed in sections 4 and 5.

### §3. Experimental Procedures

#### 3.1. Samples

Germanium single crystals with or without dopants were used. Undoped Ge samples had ultrahigh purity containing less impurities than  $\sim 10^{11} \text{ cm}^{-3}$ . Indium-doped Ge and Zn-doped Ge samples were those employed in earlier works and denoted Ge/In-1, Ge/In-2 and Ge/In-3; Ge/Zn-1, Ge/Zn-2 and Ge/Zn-3 in the order of increasing impurity concentration. These specimens were supplied by Toshiba Corporation. Beryllium-doped samples, Ge/Be 722-21.5 and Ge/Be 727-15.0 were supplied by Prof. E.E. Haller at Lawrence Berkeley Laboratory at U.C. Berkeley. Dopants studied in this work were all acceptors. Classification and concentration of the impurities in the doped Ge are listed in Table 2. Samples had a cylindrical shape with a diameter of 4 mm for In-doped and Zn-doped Ge, or 3 mm for Be-doped and with a height of  $\lesssim 3.5$  mm. It was found that the magnitude of the produced strain was larger in samples having smaller radii. The axis of the cylinder was almost parallel to the  $\langle 001 \rangle$ -crystallographic axis for one of the two pure Ge specimens and for all of the Zn-doped ones. On the other hand, the axis was almost along the  $\langle \bar{1}10 \rangle$ -axis for the other pure sample and for In-doped and Be-doped ones. Samples were mechanically polished, etched with a CP-4 solution and rinsed with methanol. Each sample was installed in a Kel-F (polychloro-trifluoroethylene resin) ring-shaped holder. Permanent strain was introduced into each sample by a nylon screw along the  $\langle 110 \rangle$ -direction for the  $\langle 001 \rangle$ -oriented samples, or along the  $\langle 111 \rangle$ -direction for the rest. Examples of the mounted

samples are shown in Figs. 1, 4 and 6.

### 3.2. Magneto-acoustic attenuation measurement<sup>79)</sup>

Ultrasonic frequencies used in acoustic measurements were in a range of 30 - 700 MHz. The X-cut quartz transducer having a fundamental frequency of 20 MHz was attached to one of the flat sample faces with silicone grease. Pulse-echo technique was employed. Longitudinal ultrasonic pulses were generated by the transducer. The pulses propagated through a sample along the magnetic field direction and brought forth several echoes. The transducer had a rectangular shape and effectively covered an area around a strain well (Fig. 6). A block diagram of the experimental setup is depicted in Fig. 7. This system is a unification of ultrasonic measurement with optical modulation. The transducer was connected to the MATEC-RF pulse generator and to the receiver unit (Model 6600) with a coaxial cable. Ultrasonic waves were generated by a 800 V RF pulse with a pulse width of 0.5  $\mu$ s. An optical excitation source was provided by a Xe flash lamp having 1  $\mu$ s pulse width driven at 15 Hz. The pumping light was guided to the sample through a dual core glass rod. The sample was immersed in liquid He. To vary temperature in a range of 4.2 - 1.7 K, liquid He was pumped out. Magnetic fields were applied to the sample with a superconducting solenoid and swept to measure the magneto-acoustic attenuation due to SCEHL at a fixed temperature and at a fixed delay time. Echo signals were sent to a two channel boxcar integrator (PAR 162). The magneto-acoustic attenuation signals by SCEHL were obtained as  $\ln(I/I')$ ,

where  $I'$  was the echo intensity with an optical excitation and  $I$  without the excitation. The attenuation coefficient  $\alpha$  of SCEHL was proportional to  $\ln(I/I')$ .

### 3.3. Photoluminescence measurements<sup>59,60,62)</sup>

Experimental scheme for photoluminescence measurements are shown in Fig. 8. Photoexcitation source was provided by a 488.0 nm or 514.5 nm line of  $\text{Ar}^+$  laser. The laser beam was chopped by a mechanical chopper in cw-measurements, or by an A/O modulator with a rise time of 0.1  $\mu\text{s}$  in time-resolved measurements. The laser beam was focussed onto a sample face with a spot radius of 220  $\mu\text{m}$ . The sample was set in an optical dewar and directly immersed in liquid He. Incident power  $P_{\text{inc}}$  of the laser beam was calibrated with reflectivity of mirrors and transmittance of the lens, window and liquid He. Absorbed power  $P_{\text{abs}}$  was obtained after an estimation of absorption coefficient of Ge by Wolfe et al.<sup>38)</sup> The recombination luminescence was collected from the opposite face of the sample. Spatial resolution was made by a 1 mm  $\times$  1 mm aperture unit mounted in front of the entrance slit of a SPEX-1269 spectrometer and by moving the collector lens. The sample image was magnified by five times on the aperture (denoted as X in Fig. 4) and scanned along the sample diameter in respect of the aperture. A glass filter (TOSHIBA VR-D2) excluded the excitation light. The luminescence radiation was dispersed through the spectrometer with a 600 grooves/mm grating blazed at 1.2  $\mu\text{m}$ , and detected by a Ge-PIN photodiode (NORTH COAST EO 817P) having a response time of 0.2  $\mu\text{s}$

and kept cool at 77 K. Amplified signals were sent to a lock-in amplifier (PAR 5205) in steady-state measurements and to a boxcar integrator (PAR 162) in time-resolved measurements. The spectrometer and the lock-in amplifier were controlled by a personal computer.

A dual modulation method was sometimes used to obtain time-resolved luminescence spectra. In this method, the laser beam was chopped both by the chopper and by the A/O modulator. Signals were sent to the boxcar and to the lock-in amplifier in sequence.

### 3.4. Millimeter waves magneto-absorption measurements<sup>41,61,108)</sup>

Two kinds of experiments were utilized in millimeter wave measurements: one was circular-polarized waves experiment and the other was linear-polarized waves experiment. Nonresonant reflection-type waveguide system was designed for circular-polarized 35 GHz millimeter waves as depicted in Fig. 9.<sup>61, 108)</sup> For linear-polarized waves, a rectangular waveguide of nonresonant reflection-type, also working at 35 GHz, was used.<sup>41)</sup> The experimental equipments for circular-polarized measurements are shown in Fig. 10. Multichannellization of time-resolution of millimeter waves magneto-absorption was made possible by a combination of a digital boxcar with a personal computer.<sup>109)</sup> The excitation source was a Xe flash lamp—the same as used in the magneto-acoustic experiments, and guided through a bent dual core glass rod. Magnetic fields were supplied by a superconducting solenoid up to 6 T. The sample was directly immersed in the

liquid He both. Alfvén wave dimensional resonance of SCEHL in pure Ge was observed using this method, as will be described in section 4. Only a few doped samples showed the dimensional resonance, because of the power loss in photoexcitation in the circular-polarizing waveguide system. For the linear-polarizing system, an ordinary split electromagnet capable of producing up to 2.5 T was employed.<sup>41)</sup> The external static field produced by this magnet could be rotated around the cylindrical axis of the sample placed in the waveguide cavity. A usual analog boxcar (PAR 162) was employed at a fixed delay time in case more appropriate than using a digital unit.

## §4. Experimental Results

### 4.1. Magneto-acoustic oscillation of SCEHL

Magneto-acoustic attenuation by SCEHL in pure Ge is shown in Fig. 11 at various temperatures between 1.7 and 4.2 K for the acoustic frequency of 140 MHz and at the geometry of  $\vec{B} // \langle 001 \rangle$ . The peaks of the magneto-acoustic attenuation are due to electrons and almost periodic in the inverse of the magnetic field  $1/B$ . The unresolved and overlapping Landau level of holes<sup>91)</sup> seem to give no convincing structures of the magneto-acoustic oscillation. The line shape of the attenuation shows a drastic change even in such a narrow temperature range as presented in Fig. 11. As temperature decreases, the quantum oscillations become more distinct, and the peaks shift to higher magnetic fields and become sharper. The peak position yields the direct determination of the electron Fermi energy, while the peak shift indicates the increase in the Fermi energy with decreasing temperature. The peak width as well as height reflect a thermal broadening of the Fermi surface. The oscillations also depend on carrier scattering processes within SCEHL, which broaden the energy levels of carriers. If the magnetic field is so weak that the Landau-level interval  $\hbar\omega_c$  is comparable with the energy broadening  $\Gamma_e$  of the electron level or with the thermal energy  $k_B T$ , no oscillation will be observable. If, on the contrary, the field is so strong that the conditions  $\hbar\omega_c \gg \Gamma_e, k_B T$  is satisfied, the oscillatory behavior will be quite enhanced. The amplitude of the oscillation, consequently, grows large as the magnetic field increases and as temperature decreases. Numerical

fitting of eq.(2-23) to the experimental data is carried out with fitting parameters of the Fermi energy of electrons  $E_{Fe}$  and the level broadening  $\Gamma_e$ . Fitting examples are shown in Fig. 12.

From the fitting procedure, the e-h pair density  $n(T, B)$  and the scattering rate  $1/\tau_e$  of electrons can be determined by:

$$n(T, B) = \int_0^{\infty} d\varepsilon [\rho_+(\varepsilon, B) + \rho_-(\varepsilon, B)] f(\varepsilon, E_{Fe}) , \quad (4-1)$$

and

$$1/\tau_e = \Gamma_e / \hbar , \quad (4-2)$$

respectively. The density of states  $\rho_{\pm}(\varepsilon, B)$  is defined in eq.(2-19), and  $f(\varepsilon, E_{Fe})$  is the distribution function. If the density is plotted against  $T^2$  as in Fig. 13, the density is found to be well described by the relation,

$$n(T) = n_0 [1 - \delta_n (k_B T)^2] , \quad (4-3)$$

with  $n_0 = (6.7 \pm 0.1) \times 10^{16} \text{ cm}^{-3}$  and  $\delta_n = (5.2 \pm 0.3) \times 10^{29} \text{ erg}^{-2}$ . Equation (4-3) has the same form as eq.(2-38) with

$$n_0 \delta_n = -\delta'(n) / E_0''(n_0) . \quad (4-4)$$

The decrease in the density with increasing temperature is, thus, explained by the thermal expansion of SCEHL mentioned in section 2. The isothermal compressibility defined in eq.(2-39) is calculated from the values of  $n_0$  and  $\delta_n$ , using eq.(4-4), and we

obtain  $K_T = 7.8 \times 10^{-3} \text{ cm}^2 \text{ dyn}^{-1}$ . From the Alfvén wave dimensional resonance experiments,<sup>41,42)</sup> the compressibility has been given as  $K_T = 1.2 \times 10^{-2} \text{ cm}^2 \text{ dyn}^{-1}$ .

The carrier scattering rate plotted against  $T^2$  is shown in Fig. 14. The scattering rate can be fitted in a linear form in  $T^2$  expressed as

$$1/\tau_e = a + b T^2 \quad (4-5)$$

Here  $a$  is the temperature-independent part presumably due to residual impurities and defects, and  $bT^2$  is characteristic of the carrier-carrier scattering in Fermi liquids.<sup>110)</sup> The number of initial and final states in the scattering is proportional to the thermal broadening  $k_B T$  around the Fermi level. A simple product of the number of the initial states and that of the final states gives  $T^2$ -dependence. The electron-phonon scattering rate in Fermi liquids yields  $T^5$ -dependence<sup>111)</sup> and is less dominant than the carrier-carrier scattering rate at very low temperatures. The least square fitting gives  $a = (5.6 \pm 0.2) \times 10^{11} \text{ s}^{-1}$  and  $b = (2.9 \pm 0.2) \times 10^{10} \text{ K}^{-2} \text{ s}^{-1}$ . Both electron-electron and electron-hole scatterings may contribute to the carrier-carrier scattering, but the scattering rate between electrons and holes has been suggested to be larger than e-e and h-h scatterings.<sup>23)</sup> From the Alfvén wave resonance,<sup>41,42)</sup> the carrier scattering rate has been obtained to give  $a = (1.4 \pm 0.1) \times 10^{10} \text{ s}^{-1}$  and  $b = (1.2 \pm 0.2) \times 10^9 \text{ K}^{-2} \text{ s}^{-1}$ . The difference between the two measurements is due possibly to that individual transitions of electrons

take part in the magneto-acoustic attenuation and, while a collective motion of the e-h plasma is observed in the Alfvén wave resonance.

The magneto-acoustic attenuation at various delay times at 1.7 K is traced in Fig. 15. The geometry of the acoustic propagation and the magnetic field is the same as in Fig. 11. The long life of SCEHL enables us to observe the oscillation even at 450  $\mu$ s after the photoexcitation. The lineshape fitting based on eq.(2-23) gives the delay-time dependence of the density and the scattering rate as plotted in Fig. 16. They tend to decrease with delay time, in other words, with shrinking radius of SCEHL. For a large radius, compression by the potential gradient in eq.(2-63) is strong, and the density is increased. As the radius shrinks, the force gets weaker and the density is practically unchanged.<sup>38)</sup> The change in the scattering rate is also small. Density dependence of the scattering rate can be derived from the time variation of the density and the scattering rate, and is depicted in Fig. 17. The carrier-carrier scattering rate increases with the e-h pair density as one expects.

A remarkable deviation of the magneto-acoustic oscillation from the periodic type in  $1/B$  appears in the geometry of  $\vec{B} // \langle 110 \rangle$  above 3T. Figure 18 contains a typical magneto-acoustic attenuation for  $\vec{B} // \langle 110 \rangle$ , in which a pair of spin split levels are observed for the peak coming from the  $n=1$  Landau level. The peaks labelled  $1_+$  and  $1_-$  correspond to the levels of  $E_{1+} = 3\hbar\omega_c/2 + g^* \mu_B B/2$  and  $E_{1-} = 3\hbar\omega_c/2 - g^* \mu_B B/2$ , respectively. If the upper trace in Fig. 18 is fitted by eq.(2-23) at the  $n=2$  peak,

with a constant Fermi energy, the  $n=1_+$  and  $1_-$  peaks appear at much higher fields than expected. The non-periodic oscillation in the  $\vec{B} // \langle 110 \rangle$  geometry, then, suggests the Fermi energy to increase with magnetic field. According to the luminescence experiment near the quantum limit, Fermi energies within ordinary e-h droplets in unstrained Ge have been found to increase almost linearly with magnetic field.<sup>32)</sup> This has been understood due to increase in the e-h density of droplets with the field, which is induced by decrease in the kinetic energy in eq.(2-30) originating from the large density of states at the bottom of the Landau levels in the magnetic field. Assuming that the Fermi energy in SCEHL has a field dependence similar to that in droplets, we may write a simple relation,

$$E_{Fe} = E_{Fe}^0 + \eta B, \quad (4-6)$$

where  $E_{Fe}^0$  is the field-independent Fermi energy and  $\eta$  is a constant. Introducing eq.(4-6) into eq.(2-23), we obtain  $E_{Fe}^0 = 2.5$  meV and  $\eta = 0.18$  T<sup>-1</sup> meV at the peaks  $n=1_+$  and  $1_-$  in Fig. 18. Field dependence of the density in SCEHL derived at each peak is plotted in Fig. 19.

The magneto-acoustic oscillation by SCEHL in Ge/In-1 is observed as shown in Fig. 20. In Be or Zn-doped Ge, no oscillation is observed, probably because the oscillation undergoes a large damping due to scatterings induced by the deep impurities.

#### 4.2. Photoluminescence spectra of SCEHL and excitons

Steady-state spectra of photoluminescence from SCEHL and free excitons in pure Ge are shown in Fig. 21. Luminescence radiation from the strain well has been picked up by the spatial resolution technique described in section 3. The luminescence line denoted  $EHD_{LA}$  corresponds to a replica of the luminescence from SCEHL including an LA (longitudinal acoustic)-phonon emitted in radiative recombination. The line denoted  $FE_{LA}$  is that from free excitons around SCEHL. Relative intensity of the exciton line to that of SCEHL decreases as temperature decreases, because the excitonic evaporation from the liquid surface in eqs.(2-56a) and (2-56b) diminishes with decreasing temperature. In a doped sample, luminescence lines from the bound excitons, biexcitons and multiexcitons captured by neutral impurities can be observed. Comparison of luminescence spectra is made between pure Ge and Ge/Zn-1 at 4.2 K as shown in Fig. 22. The phonon replicas including an LA-or TA (transverse acoustic)-phonon is observed in pure Ge. Luminescence lines marked  $\gamma_0$ ,  $\alpha_0$  and  $\alpha_{TA}$  in Ge/Zn-1 are no-phonon lines of bound excitons and bound double excitons, and a TA-phonon assisted line of bound double excitons, respectively.<sup>74)</sup> The replicas such as  $\gamma_{TA}$ ,  $\alpha_{LA}$  and  $\gamma_{LA}$  overlap with the phonon replicas of e-h drops and free excitons. These data are spatially integrated spectra; then  $EHD_{LA}$  and  $EHD_{TA}$  lines include luminescence from  $\alpha$ -drops, outside the strain potential, as well as that from SCEHL.

Spatially integrated spectra of e-h drops in pure Ge, in Ge/Zn-1 and in Ge/Zn-2 are depicted in Fig. 23 at 1.7 K with a

constant laser power of 400 mW corresponding to an incident power of 240 mW. The LA- and TA-phonon assisted lines of e-h drops are observed. The intensity of these lines decrease with increasing concentration of Zn impurities. The decrease suggests nonradiative recombination in e-h drops enhanced by Zn impurities. The luminescence from ordinary e-h droplets outside the well and that from SCEHL are mixed with each other in these lines. The illumination spot is focussed near the well, however, so that SCEHL is expected to mainly contribute to the luminescence lines. Time-resolved measurements have been performed to obtain the luminescence spectra from e-h drops in those three samples. Examples of the spectra in pure Ge and in Ge/Zn-1 are shown in Figs. 24 and 25, respectively. The luminescence intensity decays in each case with delay time after the pulsed excitation, while the width remains almost unchanged. The width yields the Fermi energy, or the e-h density. This is consistent with the result in the magneto-acoustic measurement obtained for pure Ge. Time decay of the LA-line intensity in the pure sample and that in Zn-doped samples are displayed in Fig. 26. The lifetime of SCEHL, 150  $\mu$ s, is much larger than that of an ordinary drop, 40  $\mu$ s,<sup>9)</sup> in unstrained Ge. The lifetime in Ge/Zn-1 decreases to 30  $\mu$ s and is consistent with the radius decay time 90  $\mu$ s from Alfvén wave resonance which will be presented in this section. In Ge/Zn-2, the lifetime is 10  $\mu$ s. Lifetimes of SCEHL in Zn-doped Ge samples are very similar to those of ordinary drops, 25  $\mu$ s in Ge/Zn-1 and 8  $\mu$ s in Ge/Zn-2.<sup>60)</sup> Analysis based on rate equations (2-56a) and (2-56b) will be made for the time decay of the

luminescence from SCEHL resolved by the spatial resolution technique.

Examples for lineshape fitting of eqs.(2-44) and (2-48) to the experimental spectra in pure Ge at 4.2 K are shown in Fig. 27. Fitting procedure has been made for the LA-phonon assisted lines. In an unstrained sample, ordinary e-h droplets and free excitons are observed (the upper trace). Within an ordinary droplet, electrons are populated in all four valleys, and the density of states. in eq.(2-42a) should be multiplied by 4. Theoretical lineshape fitted by the equations is indicated by open circles with fitting parameters of the Fermi energies and the reduced bandgaps. Using eq.(2-45), we obtain the e-h density in the ordinary droplet,  $n = 1.9 \times 10^{17} \text{ cm}^{-3}$ , which agrees well with the previous results.<sup>7,9)</sup> The work function of the droplet is derived as  $\phi = 2.0 \text{ meV}$  from eq.(2-49). The TO (transverse optical)-phonon assisted line of free excitons overlaps with the low-energy tail of the LA-phonon assisted line of ordinary droplets. The lower trace in Fig. 27 is the luminescence spectra in a strained sample taken at 30  $\mu\text{s}$  after the excitation. By the spatial resolution procedure, luminescence observation is restricted to the region at and near the well. The laser spot is apart from the well and the size of SCEHL is fairly small. As expected from the parabolic shape of the well, the luminescence peak of SCEHL shifts to the lower photon energy with decreasing radius. Open circles provide the total theoretical lineshape built up by the two components denoted as  $\gamma$  and  $\alpha$  (see the caption for Fig. 27). The e-h density and the work function of

SCEHL are determined by the fitting to be  $n = 5.5 \times 10^{16} \text{ cm}^{-3}$  and  $\phi = 1.1 \text{ meV}$ , respectively. The density obtained here is consistent with the temperature dependence of the density in eq.(4-3) obtained by the magneto-acoustic oscillation.

Luminescence spectra in pure Ge and in Ge/Be 722-21.5 at 1.8 K are shown in Fig. 28. The spectra are observed only from the strain well and its periphery. Exciton lines as seen at 4.2 K are almost invisible. The spectra in each sample consist of SCEHL ( $\gamma$ ) and ordinary droplets ( $\alpha$ ). Introduced strain is higher and the peak shift of the  $\gamma$ -line is larger in Ge/Be 722-21.5 than in pure Ge. Fitting of these data gives the e-h density of SCEHL as  $6.5 \times 10^{16} \text{ cm}^{-3}$  in pure Ge, which agrees well with eq.(4-3), and as  $4.1 \times 10^{16} \text{ cm}^{-3}$  in Ge/Be 722-21.5. The energy shift  $\Delta E$  in the peak of SCEHL measured from that of the ordinary droplets is  $\sim 2.0 \text{ meV}$  in pure Ge or  $\sim 4.0 \text{ meV}$  in Ge/Be 722-21.5. Spatial extent of the strain potential may be estimated as  $\sim 600 \text{ }\mu\text{m}$  from the result in ref. 40. Then, the potential range  $R_s$  of a strain well is equated to  $600 \text{ }\mu\text{m}$ . Using the relation,

$$\begin{aligned} \Delta E &= U(R_s) \\ &= \alpha_s R_s^2 \end{aligned} \quad (4-7)$$

we obtain the values for the strain coefficient  $\alpha_s$ <sup>40)</sup> mentioned in section 2 as  $550 \text{ meV/cm}^2$  in pure Ge and  $1100 \text{ meV/cm}^2$  in Ge/Be 722-21.5.

### 4.3. Spatial distribution of SCEHL, ordinary droplets and excitons

Spatial distribution of photoluminescence intensity from SCEHL, ordinary droplets and excitons are measured along the sample diameter in pure Ge and in Ge/Zn-1 under steady-state condition. The intensity distribution of SCEHL, ordinary droplets and free excitons is observed at the LA-phonon assisted lines. For bound excitons, on the other hand, the distribution is measured at the no-phonon line, for the phonon assisted lines of bound excitons overlap with other lines as mentioned in connection with Fig. 22. At 1.8 K, spatial distribution of SCEHL and droplets are observed, while that of excitons is hardly detectable. In Fig. 29, the distribution of SCEHL and the ordinary droplets is plotted (solid circles) against the position  $X$  on the diameter. The compressing screw is attached to the sample at  $X = 0.4$  cm. The laser beam is focussed around  $X_I = 0.08$  cm. The center of the well is located at  $X_S = 0.36$  cm. The solid line is a fitting curve by eqs.(2-50) - (2-52), with  $\tau_\alpha = 40 \mu\text{s}$ ,<sup>7,9)</sup>  $\tau_0 = 240 \mu\text{s}$ , which will be given in the later argument, and  $n = 6.5 \times 10^{16} \text{ cm}^{-3}$ . From the fitting, the drift velocity  $v_d$  is obtained as  $(6.0 \pm 0.2) \times 10^3 \text{ cm s}^{-1}$ , the e-h generation rate is  $G_0 \sim 1.0 \times 10^{17}$  per second, and the radius of SCEHL is 250  $\mu\text{m}$ . Owing to the long life of SCEHL and the high velocity of droplets, the intensity of SCEHL relative to that at the laser spot is very high. In the pure Ge,  $\Delta E = 2.0 \text{ meV}$  has been obtained with  $\Delta x = X_S - X_I \approx 0.28 \text{ cm}$ . From eq.(2-54), we have  $F = 1.2 \times 10^{-14} \text{ dyn/pair}$ . The drift mobility multiplied by

the electronic charge  $e$  is calculated as  $(8.2 \pm 0.3) \times 10^5 \text{ cm}^2 \text{ V}^{-1} \text{ s}^{-1}$  by eq.(2-53). The mobility is related to the momentum relaxation rate through the relation

$$1/\tau = 1/m^* \mu_d \quad (4-8)$$

The translational mass of an e-h pair is taken as  $m^* = m_e + m_h = 0.58 m_0$  for  $\langle 110 \rangle$  motion. The relaxation rate is  $(3.7 \pm 0.1) \times 10^9 \text{ s}^{-1}$ . This is comparable in the order of magnitude with the value  $1.7 \times 10^9 \text{ s}^{-1}$  obtained by Tamor et al.<sup>97)</sup> at 1.8 K under a higher strain force than ours. In  $\langle 111 \rangle$ -strained Ge, they derived the drift mobility at various temperatures by measuring the transit time in the droplet propagation from the excited region. They found the mobility inversely proportional to the temperature, confirming the theoretical results for relaxation due to carrier-phonon interaction by Keldysh et al.<sup>112)</sup>

The experimental data of the luminescence distribution in Fig. 29 is larger than the calculated curve in the region between  $x \sim 0.15$  and  $\sim 0.3$  cm. This difference is probably attributable to two causes. First, SCEHL has a much longer lifetime than ordinary droplets, so that accumulation of e-h pairs is quite large near the well. This permits backward flow of e-h pairs that is neglected in eq.(2-50). Second, the assumption of a constant strain gradient is crude. Actually, as shown in Fig. 30, the difference grows more markedly as the absorbed power is increased. The apparent luminescence observed outside the sample contains stray light reflected from the sample edge as well as

from the outer sample holder, as SCEHL shines too brightly.

A drastic change in the spatial distribution can be recognized in Ge/Zn-1 through Fig. 31. A greater portion of e-h pairs is populated in the vicinity of the laser spot,  $X_I \sim 0.08$  cm. The radius of SCEHL shrinks remarkably to  $25 \mu\text{m}$ , an order of magnitude smaller than that in pure Ge. The relative luminescence intensity of SCEHL compared with that at the irradiated region is much weaker than in the case of pure Ge. This is attributed solely to the lifetime shortening from  $240 \mu\text{s}$  to  $28 \mu\text{s}$ , which is to be given later. A decrease in the drift velocity has to be taken into account for reproduction of the data. Putting  $\tau_\alpha = 25 \mu\text{s}$ <sup>60)</sup> and  $\tau_0 = 28 \mu\text{s}$  as well as  $n_0 = 6.5 \times 10^{16} \text{ cm}^{-3}$  into eqs.(2-50) - (2-52),  $v_d = (2.6 \pm 0.1) \times 10^3 \text{ cm s}^{-1}$  and  $G_0 \sim 9.2 \times 10^{15}$  pairs/s are obtained. The luminescence spectra in Ge/Zn-1 similar to Fig. 28 give  $n = 6.5 \times 10^{16} \text{ cm}^{-3}$ ,  $\Delta E \sim 2.0 \text{ meV}$  with  $\Delta x \sim 0.28 \text{ cm}$ , and  $F = 1.2 \times 10^{-14} \text{ dyn/pair}$ , the same as in pure Ge. Then the mobility is  $(3.6 \pm 0.2) \times 10^5 \text{ cm}^2 \text{ V}^{-1} \text{ s}^{-1}$  from eq.(2-53), less than half of that in the pure sample. The momentum relaxation rate reaches  $(8.5 \pm 0.3) \times 10^9 \text{ s}^{-1}$  in Ge/Zn-1. Subtracting the rate in pure Ge from this, the Zn-impurity contribution is estimated to be  $(4.8 \pm 0.3) \times 10^9 \text{ s}^{-1}$ .

At 4.2 K, exciton lines have been clearly observed. Analysis with eqs.(2-50) - (2-52) is no longer valid. Free excitons are quite mobile on account of their small translational mass. The limiting factor for the generation of SCEHL is the exciton drift rather than the droplet drift. Coupled equations for excitons and droplets will stand instead of the above equa-

tions. Here, spatial distribution of SCEHL, ordinary droplets and excitons at 4.2 K are just qualitatively studied. Figure 32 shows the spatial resolution of LA-phonon assisted lines from SCEHL, droplets and free excitons in pure Ge. The laser spot is focussed around  $X_I = 0.13$  cm. The high mobility of excitons shifts the peak of the exciton distribution towards the well. An excitonic atmosphere coexisting with SCEHL is observed. In Ge/Zn-1, the intensity distribution of bound excitons as well as that of SCEHL, droplets and free excitons is plotted in Fig. 33. Droplets and free excitons are localized near the laser spot, while bound excitons are spread over the sample. This suggests that a considerable amount of free excitons are captured by Zn impurities. A cloud of free excitons surrounding SCEHL is still observed. However, bound exciton reveal no peak corresponding to the excitonic atmosphere. It is presumably due to a stress-induced collapse of bound excitons<sup>104)</sup> in the highly strained region.

#### 4.4. Time-decay profile of luminescence intensity from SCEHL in pure Ge

On the basis of rate equations (2-56a) and (2-56b), one can analyze time decay of the luminescence intensity from SCEHL. Recombination dynamics with or without impurities in SCEHL can also be discussed. Time decay of the LA-phonon assisted line of SCEHL in pure Ge is depicted in Fig. 34 at temperatures between 4.2 and 1.8 K (open circles). The delay time means a time interval after the laser pulse is switched off. The luminescence

from SCEHL is selected by the spatial resolution technique. The experimental data are taken with a variable gate sampling at a fixed spectral position after the excitation pulse. The luminescence decay of SCEHL gets slower as the temperature decreases. This is because excitonic evaporation from SCEHL diminish with decreasing temperature. Above ~3 K, the evaporation term of excitons in eqs.(2-56a) is large, compared with the first term yielding the internal e-h recombination. The decay of SCEHL at temperatures  $\geq 3$  K is strongly affected by the exciton evaporation. Below 2 K, the decay is almost unchanged with temperature, suggesting that the internal recombination is the dominant factor and the decay profile will be well fitted by an exponential decay. At 1.8 K, the decay is like an exponential type but reveals a slight deviation from the exponential at long delay times.

Theoretical fitting is carried out to give a solid line for the decay process at each temperature. Fitting parameters are the lifetime  $\tau_0$ , the radius R at 4.2 K and the Richardson coefficient  $A_R$ . The lifetime is expected to change with temperature from eq.(2-59), since the e-h density depends on temperature as expressed in eq.(4-3). Radius of SCEHL below 4.2 K is determined by the intensity relative to that at 4.2 K,  $I_T/I_{4.2}$ , using the

$$R_T^3 n(T) / R_{4.2}^3 n(4.2) = I_T / I_{4.2} \quad , \quad (4-9)$$

where invariance of the radiative efficiency with temperature is assumed. The Richardson coefficient is independent of

temperature as usual.<sup>7,22,29,41)</sup> The work function is  $\phi=1.1$  meV, and the strain coefficient is  $\alpha=550$  meV from the spectral fitting as shown in Figs. 27 and 28. The volume of the excitonic atmosphere  $V_x$  is uniquely determined by eq.(2-64), if the radius of SCEHL is given. Time decay measurements for free excitons surrounding SCEHL is hardly performable, because the luminescence line from the excitonic atmosphere is quite weak and unresolved as seen in Fig. 27. Theoretical line for the excitons at 4.2 K (denoted as  $I_x$  in Fig. 34) qualitatively agrees with the result in far-infrared magneto-absorption measurements by Ohyama et al.<sup>41,42)</sup>

The Richardson coefficient used in the fitting procedure is  $\sim 5 \times 10^{17} \text{ K}^{-2} \text{ cm}^{-2} \text{ s}^{-1}$ , while the value up to  $1.4 \times 10^{20} \text{ K}^{-2} \text{ cm}^{-2} \text{ s}^{-1}$  has been reported for ordinary droplets in unstrained Ge.<sup>22)</sup> Theoretical estimation under an assumption of thermodynamical equilibrium between excitonic evaporation and back flow predicts

$$A_R = v_x m_x k_B^2 / 4\pi^2 \hbar^3 \quad (4-10)$$

For the excitons in the shell, we have  $A_R = 5.1 \times 10^{20} \text{ K}^{-2} \text{ cm}^{-2} \text{ s}^{-1}$ , using  $m_x=0.335m_0$ <sup>2)</sup> and  $v_x=4$  from eq.(4-10). In unstrained Ge, on the other hand,  $A_R = 2.0 \times 10^{21} \text{ K}^{-2} \text{ cm}^{-2} \text{ s}^{-1}$  is obtained with  $v_x=16$ . In the present case, the estimation based on the equilibrium is likely to fail, since the strain force always brings the excitons towards the bottom of the well.

Temperature dependence of the recombination lifetime  $\tau_0$  is shown in Fig. 35. The lifetime tends to increase as the e-h

density decreases with increasing temperature. These data enable us to obtain the coefficients for radiative and nonradiative-Auger process, B and C, with the help of the temperature dependence of the density in eq.(2-59). Recombination rate  $1/\tau_0$  defined as the inverse of the lifetime is connected with the density at each temperature and plotted in Fig. 36. In a pure sample, the term due to various imperfections, A, in eq.(2-59) can be ignored, and a fitting with the remaining two terms is carried out. The solid line is the fitting curve to give  $B \approx 2 \times 10^{-14} \text{ cm}^3 \text{ s}^{-1}$  and  $C \approx 8 \times 10^{-31} \text{ cm}^6 \text{ s}^{-1}$ . The radiative efficiency  $Q_r$  is expressed as

$$\begin{aligned}
 Q_r &= B n \tau_0 \\
 &= B n / (B n + C n^2) \quad . \quad (4-11)
 \end{aligned}$$

The efficiency does not vary noticeably in the range of densities in Fig. 36. It lies between 0.2 and 0.3. The assumption that  $Q_r$  is independent of temperature is, thus, justified. From time-resolved measurements of the magneto-oscillation of the luminescence intensity from ordinary droplets in unstrained Ge, Betzler et al.<sup>31)</sup> have obtained  $B = 3 \times 10^{-14} \text{ cm}^3 \text{ s}^{-1}$ ,  $C = 4 \times 10^{-31} \text{ cm}^6 \text{ s}^{-1}$  and  $Q_r=0.25$ . Their values are somewhat different from the present estimate, but lie in the same order. Using their values for B and C,  $Q_r$  of SCEHL leads to  $0.5 \approx 0.6$ . It has been reported that the coefficients, B and C depend on e-h pair density in e-h liquid.<sup>12-15,113,114)</sup>

#### 4.5. Free-exciton capture rate by neutral impurities

The rate equations (2-56a) and (2-56b) include a free-exciton capture rate  $C_x$  through eq.(2-60). The value for  $C_x$  is necessary to make theoretical fitting for doped samples. The capture rate in Zn-doped Ge has been given by Nakata et al.<sup>115,116)</sup> From time-resolved measurements of far-infrared magneto-absorption by bound excitons in Zn-doped Ge,<sup>116)</sup> they have derived a capture rate of  $5.4 \times 10^{-9} \text{ cm}^3 \text{ s}^{-1}$  due to a Zn impurity. Capture cross section  $\sigma_x$  by the impurity is calculated from eq.(2-66) to be  $2.5 \times 10^{-15} \text{ cm}^2$  with  $m_x=0.335m_0$ . To obtain capture rate by a Be or an In impurity, free exciton effective lifetime  $\tau_x'$  has to be measured in Be- or In-doped Ge in the absence of e-h droplets.

Photoluminescence spectra from free and bound excitons in unstrained Ge samples are shown in Fig. 37. The LA- and TO-phonon replicas are observed for free excitons, while LA-phonon replicas for bound excitons and bound excitonic complexes are found. Incident power is lower than the threshold power  $P_{th}$  for droplet creation. Threshold power is  $\sim 85 \text{ mW}$  in pure Ge without strain as shown in Fig. 38. In In-doped Ge, the lines from bound multiexcitons overlap and are unresolved.<sup>117,118)</sup> In Be-doped Ge, closed-hole-shell state stabilizes the bound double excitons captured by double acceptors.<sup>74-76)</sup>

Time-decay of the LA-phonon assisted line of free excitons is observed at 4.2 K as shown in Fig. 39. The lifetime  $\tau_x$  of free excitons in pure Ge is 4.2  $\mu\text{s}$ . The effective lifetime  $\tau_x'$  of free excitons in Ge/Be 722-21.5 or in Ge/IN-1 is 1.7  $\mu\text{s}$  or 3.8

μs, respectively. Dopant concentrations in these samples are tabulated in Table 2. From the equation

$$1/\tau_x' = 1/\tau_x + C_x N_A, \quad (4-12)$$

free-exciton capture rate  $C_x$  is obtained to be  $7.7 \times 10^{-9} \text{ cm}^3 \text{ s}^{-1}$  for Be impurity, or  $3.3 \times 10^{-10} \text{ cm}^3 \text{ s}^{-1}$  for In impurity at 4.2 K. The smaller capture rate for In is consistent with the smaller intensity of the bound-exciton line in In-doped Ge. Capture cross section derived from eq.(2-66) is listed in Table 3 for each impurity with  $m_x=0.335 m_0$ .

#### 4.6. Impurity effects on recombination process in SCEHL

Using the capture rates listed in Table 3, time-decay of the luminescence intensity of SCEHL in doped Ge is analyzed. Figure 40 shows the decay profiles of the luminescence from SCEHL in Ge/In-1 at temperatures between 4.2 and 1.8 K. Delay time corresponds to a time interval between cut-off time of the laser and the time position of a sampling gate. The decay at each temperature is similar to that in pure Ge. The spectroscopically determined work function and Richardson coefficient are similar to those in pure Ge, 1.1 meV and  $\sim 5 \times 10^{17} \text{ K}^{-2} \text{ cm}^{-2} \text{ s}^{-1}$ , respectively. Temperature dependence of the lifetime of SCEHL in Ge/In-1 is shown in Fig. 41. This is almost the same as that in pure Ge, although low-temperature values of the lifetime is slightly shorter. Lifetime of SCEHL is a little affected by strain conditions. It seems that In shallow acceptors contribute

to e-h recombination within SCEHL to an invisible extent at a concentration of  $6.0 \times 10^{13} \text{ cm}^{-3}$ .

At a higher In concentration of  $3.7 \times 10^{14} \text{ cm}^{-3}$  in Ge/In-2, however, the lifetime is found to be shortened as shown in Fig. 42. The scale of the abscissa is expanded twice as that in Figs. 34 and 40. We can obtain an induced recombination rate by the In impurities in the following way: the e-h density of SCEHL in Ge/In-1 is almost the same as in pure Ge, and the intrinsic recombination rate consisting of the radiative and nonradiative terms,  $B_n$  and  $C_n^2$ , is the same as in pure Ge. Then subtracting the intrinsic part from obtained value as the inverse of the fitting lifetime, we have extrinsic recombination rate induced by In impurities as shown in Fig. 43. The induced rate is likely to be constant at temperatures below 3.2 K to be  $8.3 \times 10^3 \text{ s}^{-1}$  (dashed line), and decreases abruptly as temperature rises from 3.2 to 4.2 K. Using the concentration of  $3.7 \times 10^{14}$ , e-h recombination rate per In impurity is obtained as  $2.2 \times 10^{-11} \text{ cm}^3 \text{ s}^{-1}$ .

Luminescence decay of SCEHL in Ge/In-3 with an In concentration of  $1.8 \times 10^{15} \text{ cm}^{-3}$  is also observed. The decay profiles at 4.2 and 1.8 K are shown in Fig. 44. The full scale of the abscissa is 250  $\mu\text{s}$ . The intensity decay at 1.8 K is well fitted by an exponential decay indicated as a solid line with a lifetime of 46  $\mu\text{s}$ . Impurity-induced recombination rate in Ge/In-3 is  $1.7 \times 10^4 \text{ s}^{-1}$  at 1.8 K.

Remarkable shortening of the lifetime of SCEHL is found in Be-doped samples. Time decay of the luminescence from SCEHL in

Ge/Be 722-21.5 with a Be concentration of  $4.5 \times 10^{13} \text{ cm}^{-3}$  is given in Fig. 45 for temperatures between 4.2 and 1.8 K. The full scale of the abscissa corresponds to 100  $\mu\text{s}$ , one tenth of that for pure Ge and for Ge/In-1 having a doping level of the same order. Decay time of the luminescence intensity of SCEHL at 3.2 K in Ge/Be 722-21.5 is not so longed as those in pure Ge and in Ge/In-1, when compared with decay time at 4.2 K in each sample. Considerable shortening in lifetime of SCEHL in Ge/Be 722-21.5 is expected around at 3.2 K. The e-h pair density and the work function in Ge/Be 722-21.5 are found to be  $4.1 \times 10^{16} \text{ cm}^{-3}$  and 0.9 meV, respectively, from spectroscopic measurement. In eq.(4-3),  $n_0$  should be replaced by  $4.2 \times 10^{16} \text{ cm}^{-3}$ . The same value for the Richardson coefficient,  $\sim 5 \times 10^{17} \text{ K}^{-2} \text{ cm}^{-2} \text{ s}^{-1}$ , is used as in pure and In-doped samples. Induced recombination rate by Be impurities in SCEHL is derived by taking the intrinsic rate composed of  $Bn$  and  $Cn^2$  from the inverse of a fitted lifetime. Temperature dependence of the induced recombination rate is displayed in Fig. 46. The rate is quite prompted around at 3 K and tends to increase with rising temperature. Recombination rate per Be-impurity in SCEHL is estimated as  $7.2 \times 10^{-10} \text{ cm}^3 \text{ s}^{-1}$  at 1.8 K, more than 30 times as large as that per In impurity.

Intensity decay of LA-phonon assisted line of SCEHL in Ge/Be 727-15.0 with a Be concentration of  $1.0 \times 10^{15} \text{ cm}^{-3}$  is observed at 4.2 and 1.8 K as shown in Fig. 47. The lifetime from a fitting with an exponential decay is 24  $\mu\text{s}$  at 1.8 K, comparable with that in Ge/Be 722-21.5 having  $4.5 \times 10^{13} \text{ cm}^{-3}$  Be impurities. Alfvén

wave dimensional resonance has not been observed in Ge/Be 727-15.0. There is a possibility that the observed intensity from the strain-well region is not wholly due to SCEHL.

Temperature dependence of time decay of LA-phonon assisted line intensity of SCEHL in Ge/Zn-1 is shown in Fig. 48. Line shape fitting is performed with the same rate equations as before. Fitted lifetime is by  $1.2 \times 10^{14}$  Zn impurities  $28 \mu\text{s}$  and that corresponds to an impurity-induced recombination rate of  $3.1 \times 10^4 \text{ s}^{-1}$ . recombination rate per Zn deep-impurity is, then,  $2.6 \times 10^{-10} \text{ cm}^3 \text{ s}^{-1}$ . At temperatures below 2.2 K, the lifetime of SCEHL in Ge/Zn-1 is almost constant. At higher temperatures, on the other hand, SCEHL is quite unstable and the lifetime appears to be shortened as evidenced from absence of the dimensional resonance.

In summary, electron-hole recombination in SCEHL is enhanced by impurities. The magnitude of induced recombination rate is largely dependent on impurity nature. The effect is considerably large for deep-level impurities such as Be or Zn double acceptors, compared to shallow impurities like In acceptors. Nonradiative recombination is noticeably accelerated by deep impurities, since the luminescence intensity from SCEHL decreases with increasing concentration of the impurities. For In impurities, the intensity decrease is not so marked. Recombination rate at 1.8 K per each impurity in SCEHL is tabulated in Table 4.

#### 4.7. Transient behavior of Alfvén wave dimensional resonance of SCEHL

As mentioned in section 2, dimensional resonance occurs within SCEHL at magnetic fields where half integral multiples of Alfvén wavelength coincide with the linear dimension of SCEHL. After the excitation light pulse is turned off, we can observe Alfvén wave dimensional resonance (AWDR) of SCEHL at decreasing magnetic fields with shrinking radius. Figure 49 shows AWDR peaks observed in 35 GHz magneto-absorption measurements at 1.6 K in various samples. Delay times after the excitation pulse are so adjusted that AWDR peaks may be observed almost at the same field position in each sample. Mode separation of AWDR is found in Ge/Be 722-21.5 and in Ge/Zn-1. The peak denoted as e or as h corresponds to e- or h-like mode. The field position gives information on radius of SCEHL. The linewidth is a direct measure for the carrier scattering rate within SCEHL.

Circular-polarized magneto-absorption of 35 GHz waves at 1.8 K due to photoexcited systems in pure Ge is exhibited in Fig. 50 for various delay times. Sharp peaks below 0.3 T are cyclotron resonances of electrons and holes around SCEHL. Anisotropic masses of carriers make each cyclotron resonance more or less active in both polarizations. Broad peaks appearing at higher fields are AWDR signals. With increasing delay time, these peaks shift to lower fields because of shrinkage of the radius. The largest peak in each trace corresponds to the fundamental AWDR. The linewidth of AWDR reveals a characteristic behavior of being proportional to the field position of AWDR. The resonance line-

width  $\Delta B$  is expressed as <sup>106)</sup>

$$\Delta B = B_{res} / \omega \tau_{av} , \quad (4-13)$$

in the high-field limit. Equation (4-13) states that AWDR has no difference between both polarizations. Experimentally, however, the field is not so high, and imbalance between the two modes, such as difference in mass or scattering rate between electrons and holes in SCEHL, causes the mode separation.<sup>107)</sup> The fundamental AWDR in the h-active mode appears at a higher field than in the e-active, since, in this field direction, cyclotron mass of heavy holes is larger than that of electrons. Resonance field of AWDR has been found to follow a change in cyclotron resonance field.<sup>107)</sup> The linewidth in the h-active mode is broader than that in the e-active, probably owing to a warping nature of the valence bands.<sup>91)</sup>

The AWDR in Ge/Zn-1 by linear-polarized millimeter waves is shown in Fig. 51. Two major peaks above 0.5 T in each trace correspond to the AWDR. Linear-polarized waves can be divided into the right- and the left-circular-polarized waves. Cyclotron resonance of heavy holes is observed at a higher field than that of electrons. One of the two AWDR peaks at a higher field is identified as the AWDR in the h-active mode, while the other at a lower field as that in the e-active mode. The linewidths of the peaks are almost proportional to the resonance fields. The widths are, however, broader than those in pure Ge. Broadening of the h-active peak, in particular, is remarkable. The reso-

nance amplitude of the h-active peak decays faster than that of the e-active as the resonance field decreases with delay time. The Alfvén wave mode in Ge/Zn-1 seems to be largely modified by enhancement of carrier scattering in SCEHL. Such a behavior is also recognized for the AWDR in Ge/Be 722-21.5 as will be mentioned later.

Although eq.(2-89) contains an averaged relaxation time  $\tau_{av}$  between electrons and holes, the equation is fitted to the e- and h-active AWDR peaks to give different values for the resonance field, the relaxation time and the resonance amplitude between the both polarization modes. Carrier scattering rate is defined as the inverse of the relaxation time. The scattering rates in the e- and the h-active modes are regarded to yield scattering rates of electrons and of holes in SCEHL, respectively. Variation of these scattering rates in pure Ge and in Ge/Zn-1 is displayed in Fig. 52. The scattering rates tend to decrease with delay time in qualitative agreement with the result obtained in the magneto-acoustic measurements that carrier-carrier scattering decreases with delay time on account of the decreasing density, as shown in Fig. 16. Apparent increase in the hole scattering rate in pure Ge is connected with the warped nature of the valence bands.<sup>91)</sup> The e-h density in Ge/Zn-1 is found almost the same as in pure Ge from the above photoluminescence measurements. Scattering rate induced by Zn impurities can be estimated by removing the intrinsic part due to carrier-carrier scattering from the total scattering rate in Ge/Zn-1. This estimate is made at a delay time region in which the density remains constant

(horizontal lines in Fig. 52). The induced scattering rates by  $1.2 \times 10^{14} \text{ cm}^{-3}$  Zn impurities are  $1.2 \times 10^{10} \text{ s}^{-1}$  for electrons and  $2.7 \times 10^{10} \text{ s}^{-1}$  for holes in SCEHL. The induced scattering rate for holes is more than twice as large as that for electrons. Assuming the induced rate to be simply proportional to Zn concentration, we obtain the induced scattering rates per Zn impurity to be  $1.0 \times 10^{-4} \text{ cm}^3 \text{ s}^{-1}$  for electrons and  $2.3 \times 10^{-4} \text{ cm}^3 \text{ s}^{-1}$  for holes at 1.6 K.

Linear-polarized 35 GHz waves magneto-absorption data in Ge/In-1 are depicted at delay times between 400 and 1200  $\mu\text{s}$  in Fig. 53. The most intense peak in each trace is the fundamental mode of the AWDR. The mode separation as seen in Ge/Zn-1 is not observed. The linewidth of the AWDR is the same as that in pure Ge reported in refs.41 and 42. Effect of scattering by In impurities in SCEHL is quite small at a concentration of  $6.0 \times 10^{13} \text{ cm}^3$ . The radius decay rate in Ge/In-1 obtained by time dependence of the resonance field is not different from that in pure Ge. In Ge/In-2, having a higher In concentration of  $3.7 \times 10^{14} \text{ cm}^{-3}$ , however, the linewidth of the AWDR is broadened, suggesting carrier-scattering is brought forth by In impurities as shown in Fig. 54. The resonance field decays more rapidly than in pure Ge, indicating the radius decay rate is accelerated. The mode separation into the e- and h-active resonances is not seen even in Ge/In-2. From a lineshape fitting, delay-time dependence of the total scattering rates in Ge/In-1 and in Ge/In-2 is depicted at 1.6 K in Fig. 55. The scattering rate in Ge/In-1 is the same as in pure Ge,<sup>42)</sup>  $\sim 1.6 \times 10^{10} \text{ s}^{-1}$ . The e-h density of SCEHL in

Ge/In-2 is almost equal to the density in pure Ge. Scattering rate induced by  $3.7 \times 10^{14} \text{ cm}^{-3}$  In impurities is  $1.8 \times 10^{10} \text{ s}^{-1}$  and an In impurity has a scattering rate of  $4.9 \times 10^{-5} \text{ cm}^3 \text{ s}^{-1}$  at 1.6 K.

The AWDR at 1.6 K in Ge/Be 722-21.5 is displayed in Fig. 56 for delay times between 80 and 120  $\mu\text{s}$ . Two large peaks in each trace are the AWDR signals. One at lower field is identified as the h-active mode, while the other at higher field as the e-active mode by means of circular-polarized AWDR measurements as shown in Fig. 57. Sharp peaks below 0.5 T are due to cyclotron resonance of electrons. Cyclotron resonance of holes is invisible. The e-active AWDR peak appears at a higher field than the h-active resonance field. The linewidth of the e-active AWDR is narrower than that of the h-active. The peak at higher field in each trace in Fig. 56 is thus assigned to be the e-active resonance. The total scattering rates obtained by theoretical fitting in Ge/Be 722-21.5 are plotted in Fig. 58. Delay-time dependence of the rates is quite similar to that in Ge/Zn-1. In Ge/Be 722-21.5, the e-h pair density within SCEHL is  $4.1 \times 10^{16} \text{ cm}^{-3}$  at 1.6 K, smaller than the density in pure Ge,  $6.5 \times 10^{16} \text{ cm}^{-3}$ . Carrier-carrier scattering rate is scaled down by the ratio of the density. This procedure is not so bad compared with the density dependence of the carrier-carrier scattering rate given by the magneto-acoustic measurements in Fig. 17. The difference in scattering rate between electrons and holes in Fig. 58 coincides with the apparent increase due to the warping nature of the valence bands. The induced scattering rate by  $4.5 \times 10^{13} \text{ cm}^{-3}$

Be impurities is  $1.9 \times 10^{10} \text{ s}^{-1}$  both for electrons and for holes. The induced scattering rate per Be impurity is reduced to  $4.2 \times 10^{-4} \text{ cm}^3 \text{ s}^{-1}$  at 1.6 K. The induced scattering rate per impurity is listed in Table 5.

In Ge/Zn-2, AWDR is observed with quite weak intensity as shown in Fig. 59. The peak appearing at  $\sim 1.8 \text{ T}$  corresponds to AWDR, since it shifts to lower fields with delay time. Amount of the shift is small and the peak disappears very rapidly. Detailed analysis, accordingly, is impossible. Sharp peaks below  $0.7 \text{ T}$  are due to cyclotron resonance of electrons. Hole resonance probably contributes to a nonresonant background.

Radius of SCEHL is proportional to resonance field of AWDR as expressed in eq.(2-91). Time dependence of the resonance field is given by the fitting as shown in Figs. 50, 51, 53, 54 and 56. Radius-decay profile can be obtained by replacing the resonance field by radius. Delay-time dependence of radius of SCEHL in doped samples is displayed in Figs. 60 and 61. Radius decay shows dual decay times in Ge/Zn-1 and likely in Ge/Be 722-21.5. With a large radius, compression by the strain force in eq.(2-63) acts on SCEHL to increase the e-h density. The lifetime of SCEHL is, then, shortened. The compression is weak, on the other hand, with a small radius and the lifetime is not shortened. Radius-decay times are 90 and 180  $\mu\text{s}$  in Ge/Zn-1, and 75 and 250  $\mu\text{s}$  in Ge/Be 722-21.5. The lifetime of SCEHL has been measured at 1.8 K from time-resolved luminescence measurement to be 28  $\mu\text{s}$  in Ge/Zn-1 and 29  $\mu\text{s}$  in Ge/Be 722-21.5 for delay time within 100  $\mu\text{s}$ , consistent with the radius decay. The radius-

decay times are 1000  $\mu\text{s}$  in Ge/In-1 and 210  $\mu\text{s}$  in Ge/In-2. In these samples, compression effect is not seen and may appear at shorter delay times.

Resonance field dependence of the AWDR amplitude is plotted in Fig. 62. Remarkable separation between the e- and h-active modes is well evidenced in Ge/Zn-1 and in Ge/Be 722-21.5. The field dependence of the h-active modes in both samples is well fitted by the fifth power of the field. While the e-active modes show the fourth-power dependence on the field. The e- and h-active modes in pure Ge are quite similar to each other and fitted by the fourth power of the field. No separation is observed in In-doped samples, and the amplitudes agree well with the fourth-power dependence on the field. The hole-active modes have stronger dependence on the resonance field than the e-active when the mode separation is large. In this case, the h-active mode decays rapidly compared with the e-active as the resonance field decreases.

#### 4.8. Temperature dependence of the AWDR

Temperature dependence of AWDR of SCEHL in Ge/In-1 is depicted in Fig. 63. Delay times are so fixed at each temperature that AWDR may be observed almost at the same field. Higher harmonics are seen at fields lower than that for the fundamental mode. As temperature is decreased, the AWDR peak becomes more distinct and narrower. The linewidth of AWDR in Ge/In-1 is quite similar to that in pure Ge at all temperatures studied. Scattering induced by  $6.0 \times 10^{13} \text{ cm}^{-3}$  In impurities in

SCEHL is small at all the temperatures. Drastic difference is found for temperature dependence of AWDR in Ge/Be 722-21.5 as exhibited in Fig. 64. Delay time at each temperature is fixed so that the AWDR peaks can be observed almost at the same field positions. Far from being narrowed, the peaks are observed to be broadened with decreasing temperature. Scattering by Be double acceptors is stronger at lower temperatures. The mode separation is observed at all temperatures.

By fitting eq.(2-89) to the experimental data, temperature dependence of carrier scattering rate in SCEHL is obtained. Fitted scattering rates are plotted in Fig. 65 against the square of temperature. The bold line corresponds to the temperature dependence of the carrier-carrier scattering found in pure Ge.<sup>42)</sup> The e-h pair density within SCEHL in Ge/In-1 has been found to be almost the same as in pure Ge. Scattering process in Ge/In-1 is solely due to the carrier-carrier scattering at low temperatures. At higher temperatures, however, the scattering rate increases in comparison with that in pure Ge. Indium shallow acceptors are more effective at higher temperatures in scattering process within SCEHL. This will be due to weakened screening by decreasing e-h density with increasing temperature.

Carrier scattering is quite enhanced by Be deep acceptors. Since the doping level of Be impurities in Ge/Be 722-21.5 is very close to that of In impurities in Ge/In-1, Be impurities are understood to have a strong influence on carrier transports in SCEHL. Contrary to the behavior of In impurities, Be impurities increases the scattering for holes as temperature is lowered.

The scattering for electrons remains almost constant. Removing the part of the carrier-carrier scattering with the observed e-h pair density from the scattering rates in Fig. 65, we have temperature dependence of the induced scattering rates by  $4.5 \times 10^{13}$  cm<sup>-3</sup> Be impurities. If the induced scattering rates are plotted against temperature in logarithmic scale, the rates are found to be well fitted by a log T-dependence, as shown in Fig. 66. The both lines fitted to the induced scattering rates seem to converge and to tend to zero. Such an unusual behavior of the scattering rates has never been observed else in any system composed of photoexcited carriers in semiconductors.

## §5. Discussion

### 5.1. Impurity-induced recombination in SCEHL

As seen from Table 4, deep impurities such as Be and Zn have a significant influence, compared to a shallow impurity In, on e-h recombination process in SCEHL. The induced recombination rate, however, is not expressed by a simple form as a function of the impurity activation energy. Despite the fact that the activation energy of Be impurity is smaller than that of Zn impurity as listed in Table 2, Be impurity has a larger recombination rate than Zn impurity. Such a reversal in order is also observed in free-exciton capture rate, bound-exciton binding energy and affinity energy for an additional hole bound to a neutral acceptor (an  $A^+$ -center). Free-exciton capture rate is tabulated in Table 3, larger for Be impurity than for Zn impurity. The binding energy of bound exciton captured by Be impurity is 5.6 meV,<sup>75,76)</sup> while that by Zn impurity is 3.2 meV.<sup>100)</sup> The binding energy of the Ge/Be  $A^+$ -center is 4.5 meV<sup>†</sup>. This is larger than the binding energy of the Ge/Zn  $A^+$ -center that is 1.9 meV.<sup>120)</sup> These reversals against the trend of the impurities activation energy will require a microscopic argument to be exactly understood.

---

†Unpublished value reported by E.E. Haller and R.E. McMurray, Jr. after a reexamination of the value in ref.77, which has been cited in ref.119.

Induced recombination rate by In impurities remain almost constant at low temperatures. The e-h density in SCEHL decreases with increasing temperature because of the thermal expansion, and the recombination rate is independent also of the density. The recombination through In impurity may be thought as a sort of recombination via a trap, like the Shockley-Read process.<sup>121)</sup> If so, the abrupt decrease in the induced recombination rate is attributable to thermal dissociation of trap-like states. For Be impurities, on the other hand, the recombination rate strongly depends on temperature. Increase with temperature is possibly due to nonradiative-multiphonon-emission process<sup>127)</sup> accompanied by local displacement of Be impurity. The multiphonon emission is enhanced as population of phonons grows with temperature. The process has been invoked to interpret nonradiative recombination of injected carriers through isolated Be impurities in Si.<sup>128)</sup> Anomalous increase about at 3 K is incapable of being explained with the multiphonon recombination. Investigation for electronic structures will be necessary for Be impurities within SCEHL. In Ge/Zn-1, SCEHL is unstable and detailed comparison with Zn impurities is not available.

Recombination through a virtual bound state such as a bound-exciton state was proposed to be responsible for e-h recombination within ordinary e-h droplets in As-doped Ge.<sup>52)</sup> This supposition was based on the observation of a strong line which, Benoit a la Guillaume and Voos claimed, was due to no-phonon assisted emission from the droplets. In the present experiments, the bound-excitonic state in recombination is excluded, since bound-exciton lines almost disappear at 1.8 K. Intensity diminution with dopand concentrations suggests a dominance of the

nonradiative process by deep acceptors. For ordinary droplets in Ge, Chen et al.<sup>51)</sup> have reported that the lifetime of droplets is unchanged by As or Ga shallow impurities up to As concentration of  $4 \times 10^{15} \text{ cm}^{-3}$  or Ga concentration of  $2 \times 10^{15} \text{ cm}^{-3}$  at 2 K. An ordinary e-h droplet in Ge has a higher e-h density of  $2.2 \times 10^{17} \text{ cm}^{-3}$ <sup>32)</sup> than that of SCEHL, and a higher recombination rate of  $2.5 \times 10^4 \text{ s}^{-1}$ . Furthermore, screening of a shallow impurity potential is more effective in ordinary droplets, as will be described later. To observe a lifetime shortening for ordinary droplets, higher concentration of shallow impurities is necessary. Actually, the lifetime has been found shortened by the impurities with a concentration more than  $10^{16} \text{ cm}^{-3}$  at 2 K.

## 5.2. Scattering by impurities in SCEHL

Scattering rates per impurity in SCEHL are listed in Table 5. The rates for Be and Zn deep acceptors are larger than that for In shallow acceptor. The reversal trend of the scattering rates against the activation energies is also observed between Be and Zn impurities. This implies that individual natures of deep acceptors are well-established even in SCEHL. In the case of Zn impurity, the scattering rate for holes is larger than that for electrons. It is similar to free-carrier scattering, in which donors scatter electrons more strongly than holes and the reverse is true for acceptors.<sup>122)</sup> Scattering rate per In impurity is  $3.3 \times 10^{-6} \text{ cm}^3 \text{ s}^{-1}$ <sup>122)</sup> for electrons at 1.5 K. The present values in SCEHL is much greater than that for electrons, possibly owing to the Fermi velocity in SCEHL two orders of magnitude larger than the thermal velocity of electrons. Electron scattering rate per Zn impurity has been obtained as  $9.8 \times 10^{-7} \text{ cm}^3 \text{ s}^{-1}$  at

1.5 K under such high stress as destroying the Zn bound excitons which act as donor-like scattering centers. In Be-doped Ge, scattering of holes is stronger than that of electrons. As seen in Fig. 58, the hole scattering rate is quite enhanced at short delay time. It gradually decreases with delay time and almost coincides with the electron scattering rate.

Difference in scattering rate between electrons and holes causes imbalance of millimeter-waves response between the two types of carriers. Theoretical calculation has predicted that the imbalance transforms the dimensional resonance of SCEHL from Alfvén-wave mode inherent to compensated plasma to helicon-wave mode to one component plasma.<sup>107)</sup> Such a behavior is well evidenced in Fig. 62. A large mode separation of AWDR is recognized in Ge/Be 722-21.5 and in Ge/Zn-1. In an Alfvén wave resonance, resonance amplitude depends on the cubic power of radius; namely, on the cubic power of the resonance field resulting from eqs.(2-90) and (2-91). In a helicon wave resonance, on the other hand, the magnitude is proportional to the fifth power of the resonance field.<sup>106)</sup> In both samples, the magnitude of the h-active mode exhibits the fifth-power dependence on the field, while that of the e-active shows the fourth-power dependence. The linewidth of each mode is still proportional to the resonance field. This is a characteristic behavior of AWDR. The helicon wave resonance has a constant linewidth independent of resonance field. If the hole scattering rate gets larger, the hole-active mode will disappear and the dimensional resonance will ultimately lead to the helicon wave resonance. In the present case for AWDR in Ge/Be 722-21.5 and Ge/Zn-1, a dual nature accounting for both Alfvén and helicon

waves is observed.

The log T-dependence of the induced scattering rates by Be impurities in Fig. 66 is too unusual to be explained with a simple model. Recently, it has been pointed out that log T-dependence can be observed in DC-resistivity of a metal without a spin interaction.<sup>123)</sup> In the case of the s-d interaction between a travelling spin of a conduction electron and a localized spin of a magnetic impurity, log T-dependence of DC-resistivity in a metal is quite well known as the Kondo effect. Instead of the spin interaction, dynamical state consisting of two levels, such as tunneling interaction between two levels may contribute to the log T-behavior in the resistivity.<sup>123,124)</sup> Frequency of millimeter waves is very small and scattering rate monitored by millimeter-waves magneto-absorption technique is usually equated to DC-scattering rate.<sup>122)</sup> One possible reasoning to explain the log T-dependence of the Be-induced scattering rates is such a "pseudo-Kondo effect" arising from a tunneling interaction in Fermi liquid. There is no evidence, however, that a Be double acceptor forms a tunneling-two-level system. Detailed investigation is necessary to clarify the unusual temperature dependence of the scattering rates.

### 5.3. Mott's criterion for ionization of an impurity in SCEHL

Consistent results are obtained between recombination properties from the time-resolved luminescence measurements and transport properties from the Alfvén wave dimensional resonance experiments. Indium shallow impurities have a small effect on e-h

recombination and carrier scattering in SCEHL. While Be and Zn impurities markedly affect the recombination and the scattering. Qualitative understanding of these results is made possible by considering ionization criterion for an impurity in SCEHL. Introducing a screening length  $\lambda_{TF}$  by the Thomas-Fermi formula as (125)

$$1/\lambda_{TF}^2 \simeq 4m^*e^2 n^{1/3} / \kappa \hbar^2, \quad (5-1)$$

where  $m^*$  is the effective mass of carriers,  $n$  is the carrier density and  $\kappa$  is the dielectric constant. For a hydrogenic impurity having a screened potential

$$-e^2 \exp[-\lambda_{TF}^{-1} r] / r, \quad (5-2)$$

an effective Bohr radius is defined as

$$a_B^* = \kappa \hbar^2 / m^* e^2 \quad (5-3)$$

A carrier bound in the potential (5-2) will be released, if the following condition is satisfied:

$$\lambda_{TF} \lesssim a_B^*,$$

namely

$$n^{-1/3} \lesssim 4a_B^*. \quad (5-4)$$

The relation (5-4) is called the Mott criterion for impurity

ionization.

In SCEHL, we have  $n^{-1/3} \approx 260$  A. Shallow acceptor In has  $a_B^* = 40$  A. Although the condition (5-4) is invalid,  $4a_B^*$  is not so small in comparison with  $n^{-1/3}$ . Then the potential of In impurity is effective on carriers in SCEHL, and we find that scattering and recombination are induced by In impurities but to a small extent. An ordinary e-h droplet in unstrained Ge has  $n^{-1/3} \approx 170$  A and the condition (5-4) almost holds.

The criterion (5-4) cannot be directly adopted for double acceptors, since a double acceptor is a helium-like impurity. For a double acceptor, we may put an outer orbital radius  $r_A^*$  in place of the effective Bohr radius  $a_B^*$ . First ionization energy of a real helium atom is 1.8 times as large as the Rydberg energy of a hydrogen, and the 1s-orbital radius 0.57 times as large as the hydrogen Bohr radius.<sup>126)</sup> As seen from Table 2, the first activation energy of Be double acceptor or Zn double acceptor is 2.2 times or 2.9 times as large as the effective Rydberg energy of In impurity. The relative activation energies of both deep impurities are larger than expected from the He-like model. By making a simple scaling adjustment, the impurity radius is estimated as 19 A for Be impurity or as 14 A for Zn impurity. For double acceptors, the Mott criterion is far from being valid in SCEHL. Potentials of these deep impurities will then have a short-range nature. Carriers will see nearly a bare impurity potential due to Be or Zn impurity. This is the reason why scattering and recombination in SCEHL are so augmented by the deep impurities. The strong potentials give rise to carrier

binding to the impurities. Probably holes are bound to Be and Zn double acceptors. Deep impurity such as Be or Zn acceptor is likely to be neutralized. The neutralized impurity in SCEHL might be somewhat different from an isolated neutral impurity. Carriers bound to the neutralized impurities might recombine with the other type of carriers. In that case, the pseudo-neutral impurity acts as a recombination center to decrease the lifetime of SCEHL. Transport properties in SCEHL will also be influenced by the neutralized impurities.

## §6. Conclusion

Experimental results are now summarized. From the magneto-acoustic measurements, the properties of SCEHL in pure Ge have been investigated:

1. Electron-hole pair density in SCEHL reflects thermal expansion effect and decreases with temperature.
2. Carrier-carrier scattering has been observed clearly.
3. The density increases at high magnetic fields.

Spatial resolution measurements for steady-state luminescence from ordinary droplets and SCEHL have been performed.

4. On the basis of the one-dimensional drift equation, momentum relaxation rate for an e-h pair in ordinary droplets is estimated. The relaxation rate induced by Zn deep impurities is  $(4.8 \pm 0.3) \times 10^9 \text{ s}^{-1}$  at 1.8 K.

Time-decay profile of the luminescence from SCEHL has been measured at temperatures at 4.2 and 1.8 K. The data have been analyzed by the rate-equation method.

5. Effect of shallow acceptor In on recombination process in SCEHL is small.
6. Double acceptors Be and Zn remarkably decrease the lifetime of SCEHL.
7. Temperature dependence of the induced recombination rate by Be impurities shows unusual behavior.
8. Radiative and nonradiative-Auger recombination coefficients have been obtained to be  $B \approx 2 \times 10^{-14} \text{ cm}^3 \text{ s}^{-1}$  and  $C \approx 8 \times 10^{-31} \text{ cm}^6 \text{ s}^{-1}$ , respectively. Corresponding radiative efficiency is between 0.2 and 0.3.

9. Free-exciton capture rate has been derived for Be, Zn and In impurities and listed in Table 3.

10. The impurity-induced recombination rate per impurity at 1.8 K has been tabulated in Table 4.

Alfvén wave dimensional resonance of SCEHL has clarified impurity effects on transport phenomena in SCEHL.

11. Shallow impurity In contributes to carrier scattering to a small extent.

12. Marked increase in scattering rate has been found in Ge doped with Be or In deep impurities.

13. Inbalance between electron and hole scatterings is caused by deep impurities. Dimensional resonance shows a dual nature of Alfvén waves and helicon waves.

14. The impurity-induced scattering rate per impurity at 1.6 K has been listed in Table 5.

15. The Be-induced scattering rates for electrons and for holes show the log T-dependence. One of the possible causes of the unusual dependence is the "pseudo-Kondo effect" due to dynamic-tunneling interaction in Fermi liquid.

High influence of the deep acceptors has been qualitatively recognized by the Mott criterion for impurity ionization. The potentials of the deep impurities have such a short-range nature that they are not screened.

Far-infrared magneto-absorption by SCEHL in pure Ge has been observed at 4.2 and 1.8 K as shown in Fig. 67. The peak around at 3.5 T becomes distinct at 1.8 K. Far-infrared magneto-

absorption technique has been widely used for ordinary droplets in unstrained Ge. While few works have been presented on submillimeter-waves magneto-absorption of SCEHL. Investigation in this field will be a subject for future study. In this thesis work, the effect of acceptors has been studied in detail and nothing has been attempted for donors. To examine effects of donors is expected to add a good deal of information to our knowledge on impurity effects on this nonequilibrium Fermi liquid in Ge.

## Acknowledgements

I would first like to thank Professor Eizo Otsuka for providing me not only the chance to work in this exciting area of condensed-matter physics, but also stimulating ideas and encouragements in the course of this work. I am also grateful and deeply indebted to Professor Tyuzi Ohyama, with whom I worked closely on the experiments. His instruction, ideas and technical as well as mental support so much helped me. Without their influence, quality of this work would certainly have been degraded.

I would like to thank Dr. Hiroyasu Nakata for his support in interfacing the computer to the photoluminescence apparatus and for fruitful discussions and comments. I am also indebted to Dr. Ken'ichi Fujii for his kind help in the experiments and for useful discussions and comments. I have also received a great deal of assistance from the other members of the Otsuka group.

I am further grateful to Prof. Eugene E. Haller of U.C. Berkeley for supplying Be-doped Ge samples of high quality (722-21.5 and 722-15.0). I also thank Prof. Shin'ichi Katayama of Niigata University for his interest and fruitful discussions.

I am so much grateful and indebted to Miss Hiroko Matsumura for her aid with typing the manuscript of this thesis.

## References

- 1) R.S. Knox: "Theory of Excitons" in Solid State Physics, eds. H. Ehrenreich, F. Seitz and D. Turnbull (Academic, New York, 1963) Suppl. 5.
- 2) A. Frova, G.A. Thomas, R.E. Miller and E.O. Kane: Phys. Rev. Lett. 34 (1975) 1572.
- 3) N.O. Lipari and A. Baldereschi: Phys. Rev. B3 (1971) 2497.
- 4) L.V. Keldysh: Proc. IX Int. Conf. Phys. Semicond., Moscow 1968 (Nauka, Leningrad, 1968) p.1303.
- 5) V.M. Asnin and A.A. Rogachev: Zn. Eksp. Teor. Fiz., Pis'ma Red. 7 (1968) 764. translation: JETP Lett. 7 (1968) 360.
- 6) Y.E. Pokrovskii and K.I. Svistunova: Zh. Eksp. Teor. Fiz., Pis'ma Red. 9 (1969) 435. translation: JETP Lett. 9 (1969) 261.
- 7) Y.E. Pokrovskii: Phys. Stat. Solidi a11 (1972) 385.
- 8) T.M. Rice: Solid State Physics, eds. H. Ehrenreich, F. Seitz and D. Turnbull (Academic, New York, 1977) 32, p.1.
- 9) J.C. Hensel, T.G. Phillips and G.A. Thomas: Solid State Physics, eds. H. Ehrenreich, F. Seitz and D. Turnbull (Academic, New York, 1977) 32, p.87.
- 10) "Electron-Hole Droplets in Semiconductors", eds. C.D. Jeffries and L.V. Keldysh, Modern Problems in Condensed Matter Sciences (North-Holland, Amsterdam, 1983) Vol.6.
- 11) C. Benoit a la guillaume and M. Voos: Phys. Rev. B5 (1972) 3079.
- 12) M. Combescot and P. Nozières: J. Phys. C5 (1972) 2369.
- 13) W.F. Brinkman and T.M. Rice: Phys. Rev. B7 (1973) 1508.

- 14) P. Vashishta, P. Bhattacharyya and K.S. Singwi: *Phys. Rev.* B10 (1974) 5108.
- 15) P. Vashishta and R.K. Kalia: *Phys. Rev.* B25 (1982) 6492.
- 16) Y.E. Pokrovskii and K.I. Svistunova: *Zh. Eksp. Teor. Fiz., Pis'ma Red.* 13 (1971) 297. translation: *JETP Lett.* 13 (1971) 212.
- 17) A.S. Alekseev, T.M. Astimirov, V.S. Bagaev, T.I. Galkina, N.A. Denin, N.N. Sibeldin and V.A. Tsvetkov: *Proc. XII Int. Conf. Phys. Semicond., Stuttgart, 1974* (B.G. Teubner, Stuttgart, 1974) p.91.
- 18) M. Greenstein and J.P. Wolfe: *Phys. Rev. Lett.* 41 (1978) 715.
- 19) R.M. Westervelt, J.C. Culbertson and B.S. Black: *Phys. Rev. Lett.* 42 (1979) 267.
- 20) R.M. Westervelt, J.L. Staehli and E.E. Haller: *Phys. Stat. Solidi* b20 (1978) 557.
- 21) Y. Shiraki and H. Nakashima: *Solid State Commun.* 27 (1978) 1033.
- 22) R.M. Westervelt, T.K. Lo, J.L. Staehli and C.D. Jeffries: *Phys. Rev. Lett.* 32 (1974) 1051.
- 23) V.M. Murzin, V.A. Zayats and V.L. Kononenko: *Fiz. Tverd. Tela* 17 (1975) 2684. translation: *Sov. Phys. Solid State* 17 (1975) 1783.
- 24) K. Fujii and E. Otsuka: *J. Phys. Soc. Jpn.* 38 (1975) 742.
- 25) H.G. Zarate and T. Timusk: *Phys. Rev.* B19 (1979) 5223.
- 26) A.S. Alekseev, T.I. Galkina, V.N. Maslennikov, R.G. Khakimov and E.P. Shebnev: *ZhETF Pis. Red.* 21 (1975) 578.

- 27) A.D.A. Hansen: Ph.D. Thesis, U.C. Berkeley, 1977, unpublished.
- 28) J.C. Hensel and R.C. Dynes: Phys. Rev. Lett. 39 (1977) 969.
- 29) J.C. Hensel, T.G. Phillips and T.M. Rice: Phys. Rev. Lett. 30 (1973) 227.
- 30) T. Ohyama, T. Sanada and E. Otsuka: Phys. Rev. Lett. 33 (1974) 647.
- 31) K. Betzler, B.G. Zhurkin and A.L. Karuzskii: Solid State Commun. 17 (1975) 577.
- 32) H.L. Störmer and R.W. Martin: Phys. Rev. B20 (1979) 4213.
- 33) H. Nakata and E. Otsuka: Phys. Rev. B23 (1981) 5428.
- 34) T. Ohyama, A.D.A. Hansen and J.L. Turney: Solid State Commun. 19 (1976) 1083.
- 35) R.S. Markiewicz, J.P. Wolfe and C.D. Jeffries: Phys. Rev. Lett. 32 (1974) 1357.
- 36) I. Balslev: Phys. Rev. 143 (1966) 636.
- 37) J.P. Wolfe, W.L. Hansen, E.E. Haller, R.S. Markiewicz, C. Kittel and C.D. Jeffries: Phys. Rev. Lett. (1975) 1292.
- 38) J.P. Wolfe, R.S. Markiewicz, S.M. Kelso, J.E. Furneaux and C.D. Jeffries: Phys. Rev. B18 (1978) 1479.
- 39) P. Nozières: Proc. X VI Int. Conf. Phys. Semicond., Montpellier, 1982 (North-Holland, Amsterdam. 1983) p.16.
- 40) R.S. Markiewicz, J.P. Wolfe and C.D. Jeffries: Phys. Rev. B15 (1977) 1988.
- 41) T. Ohyama and E. Otsuka: J. Phys. Soc. Jpn. 48 (1980) 1550.
- 42) T. Ohyama, I. Honbori and E. Otsuka: J. Phys. Soc. Jpn. 48 (1980) 1559.

- 43) K. Fujii, T. Ohyama and E. Otsuka: J. Phys. Soc. Jpn. 54  
(1985) 740.
- 44) A.S. Alekseev, V.S. Bagaev, T.I. Galkina, O.V. Gogolin and  
N.A. Penin: Fiz. Tverd. Tela 12 (1970) 3516. translation:  
Sov. Phys. Solid State 12 (1971) 2855.
- 45) B.J. Feldman: Solid State Commun. 15 (1974) 131.
- 46) B. Bergersen, J.A. Rostoworowski, E. Eswaran and R.R.  
Parsons: Phys. Rev. B14 (1976) 1633.
- 47) R.R. Parsons and M.L.W. Thewalt: Solid State Commun. 21  
(1977) 1087.
- 48) B.V. Novikov, R.L. Korchazhika and N.S. Sokolov: Fiz. Tverd.  
Tela 15 (1973) 459. translation: Sov. Phys. State 15 (1973)  
326.
- 49) R.E. Halliwell and R.R. Parsons: Can. J. Phys. 52 (1974)  
1336.
- 50) R.W. Martin and R. Sauer: Phys. Stat. Solidi b62 (1974)  
443.
- 51) M. Chen, D.L. Smith and T.C. McGill: Phys. Rev. B15 (1977)  
4983.
- 52) C. Benoit a la Guillaume and M. Voos: Solid State Commun.  
(1972) 1585.
- 53) M. Chen, S.A. Lyon, D.L. Smith and T.C. McGill: Phys. Rev.  
B17 (1978) 4744.
- 54) J. Wagner, W. Schmid and R. Sauer: Solid State Commun. 32  
(1979) 1215.
- 55) T. Ugumori, K. Morigaki and C. Nagashima: J. Phys. Soc. Jpn.  
46 (1979) 536.

- 56) M.A. Washington, J.M. Warlock and M. Voos: Solid State Commun. 33 (1980) 549.
- 57) V.M. Asnin, V.V. Bel'kov, A.A. Rogachev. V.I. Stepanov and I.M. Fishman: Solid State Commun. 48 (1983) 611.
- 58) J.C. Culbertson and J.E. Furneaux: Solid State Commun. 54 (1985) 417.
- 59) K. Ogawa, T. Ohyama and E. Otsuka: Solid State Commun. 57 (1986) 231.
- 60) H. Nakata, Y. Ichikawa and E. Otsuka: Jpn. J. Appl. Phys. 25 (1986) L294.
- 61) K. Ogawa, T. Ohyama and E. Otsuka: Solid State Commun. 60 (1986) 79.
- 62) K. Ogawa, T. Ohyama and E. Otsuka: to be published in Jpn. J. Appl. Phys. 26 (1987) No.1.
- 63) B. Bergensen, P. Jena and A.J. Berlinsky: J. Phys. C8 (1975) 1377.
- 64) G. Mabler and J.L. Birman: Phys. Rev. B12 (1975) 3221.
- 65) D.L. Smith: Solid State Commun. 18 (1976) 637.
- 66) G. Mabler and J.L. Birman: Phys. Rev. B13 (1976) 3661.
- 67) L. Sander, H.H. Shore and J.H. Rose: Solid State Commun. 27 (1978) 331.
- 68) E. Otsuka: J. Phys. Soc. Jpn. 50 (1981) 189.
- 69) Y.E. Pokrovskii and K.I. Svistunova: Proc. XII Int. Conf. Phys. Semicond., Stuttgart, 1974 (B.G. Teubner, Stuttgart, 1974) p.71.
- 70) J. Cross, L.T. Ho, A.K. Ramdas, R. Sauer and E.E. Haller: Phys. Rev. B28 (1983) 6953.

- 71) R.J. Jones: Ph.D.Thesis, Purdue University, 1968, unpublished.
- 72) N.R. Butler and P. Fisher: Phys. Rev. B13 (1976) 5465.
- 73) H. Brooks: "Advances in Electronics and Electron Physics", 1955, Vol.7.
- 74) H. Nakata and E. Otsuka: Phys. Rev. B29 (1984) 2347.
- 75) R. Sauer and J. Weber: J. Phys. C17 (1984) 1421.
- 76) M.L.W. Thewalt, E.C. Lightowers and E.E. Haller: Solid State Commun. 54 (1985) 1043.
- 77) E.E. Haller, R.E. McMurray, Jr., L.M. Falicov, N.M. Haegel and W.L. Hansen: Phys. Rev. Lett. 51 (1983) 1089.
- 78) H. Nakata, Y. Ichikawa and E. Otsuka: Jpn. J. Appl. Phys. 23 (1984) L889.
- 79) T. Ohyama, K. Ogawa and E. Otsuka: J. Phys. Soc. Jpn. 53 (1984) 2358.
- 80) J.P. Wolfe and C.D. Jeffries: Chap. 5 in ref.10.
- 81) C. Herring and E. Voigt: Phys. Rev. 101 (1956) 944.
- 82) G.E. Pikus and G.L. Bir: Fiz. Tverd. Tela 1 (1959) 1642. translation: Sov. Phys. Solid State 1 (1959) 1502.
- 83) A.P. Korolyuk and T.A. Prushak: Zn. Exp. Teor. Fiz. 41 (1962) 1689. translation: Sov. Phys. JETP 14 (1962) 1201.
- 84) Y. Shapira and B. Lax: Phys. Rev. Lett. 12 (1964) 166.
- 85) D.H. Reneker: Phys. Rev. 115 (1959) 303.
- 86) A.P. Korolyuk: Fiz. Tverd. Tela 5 (1963) 3323. translation: Sov. Phys. Solid State 5 (1964) 2433.
- 87) A.M. Toxen and S. Tensal: Phys. Rev. 137 (1965) A211.
- 88) Y. Sawada, E. Burstein and L. Testarki: Proc. VIII Int.

- Conf. Phys. Semicond., Kyoto, 1966, J. Phys. Soc. Jpn. 21  
(1966) Suppl. p.760.
- 89) S. Mase, Y. Fujimori and H. Mori: J. Phys. Soc. Jpn. 21  
(1966) 1744.
- 90) P.N. Argyres: J. Phys. Chem. Solids 4 (1958) 19.
- 91) J.C. Hensel and K. Suzuki: Phys. Rev. B9 (1974) 4219.
- 92) K. Murase, E. Enjouji and E. Otsuka: J. Phys. Soc. Jpn. 29  
(1970) 1248.
- 93) D.K. Wilson: Phys. Rev. 134 (1964) A265.
- 94) R.B. Dingle: Proc. Roy. Soc. London A211 (1952) 517.
- 95) D. Pines: "Elementary Excitations in Solids" (W.A. Benjamin,  
New York, 1964) p.58.
- 96) R.A. Smith: "Semiconductors" (Cambridge Univ. Press,  
Cambridge, 1978) p.85.
- 97) M.A. Tamor, M. Greenstein and J.P. Wolfe: Phys. Rev. B27  
(1983) 7353.
- 98) V.S. Bagaev, L.V. Keldysh, N.N. Sibeldin and V.A. Tsvetkov:  
Zh. Eksp. Teor. Fiz. 70 (1976) 702. translation: Sov. Phys.  
JETP 43 (1976) 362.
- 99) H. Nakata and E. Otsuka: J. Phys. Soc. Jpn. 54 (1985) 3605.
- 100) H. Nakata and E. Otsuka: J. Phys. Soc. Jpn. 55 (1986) 391.
- 101) R.A. Smith: cited in ref. 96, p.187.
- 102) J.C. Culbertson, R.M. Westervelt and E.E. Haller: Phys. Rev.  
B34 (1986) 6980.
- 103) M.A. Tamor and J.P. Wolfe: Phys. Rev. Lett. 44 (1980) 1703.
- 104) E. Otsuka, H. Nakata and Y. Ichikawa: J. Phys. Soc. Jpn. 55  
(1986) 2064.

- 105) E.D. Palik and J.K. Furdyna: Rep. Prog. Phys. 33 (1970) 1193.
- 106) J.R. Dixon, Jr. and J.K. Furdyna: Phys. Rev. B13 (1976) 4626.
- 107) R.S. Markiewicz: Phys. Rev. B18 (1978) 4260.
- 108) K. Ogawa: Conf. Digest X Int. Conf. Infrared and Millimeter Waves, Orlando, 1985 (IEEE, 1985) p.156.
- 109) H. Nakata and E. Otsuka: Appl. Phys. B27 (1982) 207.
- 110) D. Pines: cited in ref.95, p.277.
- 111) D. Pines: cited in ref.95, p.274.
- 112) L.V. Keldysh and S.G. Tikhodeev: ZhETF Pis. Red. 21 (1975) 582. translation: JETP Lett. 21 (1975) 273.
- 113) H.-h. Chou and G.K. Wong: Phys. Rev. Lett. 41 (1978) 1677.
- 114) J.C. Culbertson and J.E. Furneaux: Phys. Rev. Lett. 49 (1982) 1528.
- 115) H. Nakata and E. Otsuka: J. Phys. Soc. Jpn. 54 (1985) 3605.
- 116) H. Nakata and E. Otsuka: J. Phys. Soc. Jpn. 55 (1986) 391.
- 117) E.F. Gross, B.V. Novikov and N.S. Sokolov: Fiz. Tverd. Tela 14 (1972) 443. translation: Sov. Phys. Solid State 14 (1972) 368.
- 118) E.C. Lightowers and Z.E. Ciechanowska: J. Phys. C14 (1981) L719.
- 119) D. Labrie, M.L.W. Thewalt and B.P. Clayman: Phys. Rev. B32 (1985) 5514.
- 120) H. Nakata, Y. Ichikawa, E. Otsuka and M. Kobayashi: J. Phys. Soc. Jpn. 55 (1986) 2859.
- 121) W. Shockley and W.T. Read, Jr.: Phys. Rev. 87 (1952) 835.

- 122) E. Otsuka: Jpn. J. Appl. Phys. 25 (1986) 303.
- 123) K. Vladár and A. Zawadowski: Phys. Rev. B28 (1983) 1596.
- 124) S. Katayama, S. Maekawa and H. Fukuyama: submitted to J. Phys. Soc. Jpn.
- 125) J.M. Ziman: "Principles of the Theory of Solids" (Cambridge Univ. Press, Cambridge, 1972) sect. 5.
- 126) J.C. Slater: "Introduction to Chemical Physics" (McGraw-Hill, New York, 1939) p.348.
- 127) B. K. Ridley: J. Phys. C11 (1978) 2323.
- 128) A. C. Wang, L. S. Lu and C. T. Sah: Phys. Rev. B30 (1984) 5896.

## Figure Captions

- Fig. 1            Photographs of strain-confined electron-hole liquid (SCEHL) in pure Ge and  $6.0 \times 10^{13} \text{ cm}^{-3}$  In-doped Ge. Disc-shaped Ge crystal with a 4 mm diameter and a height  $\sim 3.5$  mm is set in a sample holder and immersed in liquid helium. Inhomogeneous strain is introduced into the sample with a screw. The sample was excited by a cw-Ar<sup>+</sup>-laser. These pictures have been taken by an infrared-sensitive vidicon system which detects e-h recombination luminescence at  $\sim 1.7 \text{ }\mu\text{m}$  from the sample. A strain well is formed just inside the sample from the point contacted by the screw, and SCEHL is produced in the well. The second bright spot is due to recombination emission under the laser spot in each sample.
- Fig. 2            The origin of the quantum oscillation in the magneto-acoustic attenuation by SCEHL is illustrated (see text).
- Fig. 3            Schematical representation of radiative recombination in SCEHL. Just one conduction band is drawn taking account of the single valley population. It is filled up to the Fermi level  $F_e$ . The band should, actually, be shifted to the Brillouin zone edge in Ge. The valence band is occupied to the Fermi level  $F_h$ . The Fermi levels  $F_e$  and  $F_h$  are denoted  $E_{F_e}$  and  $E_{F_h}$  in the text.
- Fig. 4            Top: Overview of the sample and its holder used in the experiments. The sample diameter is 0.4 cm. For

excitation, a laser beam is focussed on the spot marked +. The position of the aperture for spatial resolution measurements is denoted as X. Bottom: Spatial distribution of luminescence intensity along the diameter. The  $\alpha$ -drops generated at the laser spot around  $X_I$  move into the strain well with a drift velocity  $v_d$ . Strain-confined EHL appears in the well around  $X_S$ .

Fig. 5            strain-confined EHL and coexisting excitonic atmosphere in the strain potential. Processes labelled (1)-(5) are e-h recombination in SCEHL, free-exciton(FE) evaporation from the surface of SCEHL, free-exciton back flow into SCEHL, recombination of a free exciton and free-exciton capture by a neutral impurity, respectively. Free exciton captured by a neutral impurity forms a bound exciton (BE).<sup>99,100)</sup>

Fig. 6            (a) Sample mounting arrangement for magneto-acoustic measurements. Magnetic field is parallel to the acoustic propagation path. (b) Overview of the above system. Transducer covers an area where SCEHL exists.

Fig. 7            Block diagram of the experimental setup for magneto-acoustic measurements.

Fig. 8            Block diagram for photoluminescence measurements. Symbols, M, L, F and A are a mirror, a lens, a glass filter and an aperture, respectively.

Fig. 9            Waveguide system for circular-polarized 35 GHz millimeter waves magneto-absorption measurements.

Linear-polarized waves from a klystron is transformed into circular-polarized waves by a polarizer. The waveguide is mainly made of a conducting Cu-Ni pipe with a small thermal conductivity. Excitation light from a xenon flash lamp is guided through a dual core glass rod with one edge bent. The system was designed for utilization with a superconducting solenoid up to 6 T.

Fig. 10 Block diagram for multichannel time-resolved measurements of magneto-absorption of circular-polarized 35 GHz waves due to SCEHL.

Fig. 11 Recorder traces of the magneto-acoustic attenuation due to SCEHL at various temperatures. Acoustic propagation and magnetic field are along the  $\langle 001 \rangle$  direction. These data were taken at 50  $\mu$ s after the photoexcitation pulse. Indices  $n=1, 2$  and 3 denote the Landau quantum numbers of electrons crossing the Fermi level. The ground levels for the upper four traces are given by horizontal lines, a, b, c and d.

Fig. 12 Fitting examples using eq.(2-23). Solid lines are the experimental data at 3.0 K and at 2.2 K. Open circles give the theoretical lines given by eq.(2-23) with  $E_{Fe} = 2.7$  meV and  $\Gamma_e = 0.55$  meV at 3.0 K, and  $E_{Fe} = 2.9$  meV and  $\Gamma_e = 0.48$  meV at 2.2 K.

Fig. 13 The e-h density in SCEHL plotted against the square of the temperature  $T^2$ . The density is obtained from eq.(4-1). The solid line corresponds to the least

square fitting of eq.(4-3).

- Fig. 14            The scattering rate of electrons in SCEHL versus  $\tau^2$ . The solid line is given by eq.(4-5).
- Fig. 15            Magneto-oscillations of SCEHL at various delay times at 1.7 K with an ultrasonic frequency of 140 MHz. Horizontal bars labelled a, b, c and d give the ground levels as in Fig. 11.
- Fig. 16            Variation of the density and the scattering rate with delay time at 1.7 K.
- Fig. 17            Density dependence of the scattering rate deduced from the data in Fig. 16.
- Fig. 18            The upper trace is the magneto-acoustic attenuation for  $\vec{B} // \langle 110 \rangle$  at 1.9 K, while the lower for  $\vec{B} // \langle 001 \rangle$ , corresponding to Fig. 11 and 15.
- Fig. 19            The e-h pair density as a function of the magnetic field. The density has been determined at each peak in the data at 140  $\mu$ s and at 160  $\mu$ s after the excitation photopulse.
- Fig. 20            Magneto-oscillation by SCEHL in Ge/Zn-1. Magnetic field and acoustic propagation are parallel to the  $\langle 110 \rangle$  direction. The data were taken at 1.9 K at 60  $\mu$ s after the excitation with an ultrasonic frequency of 180 MHz.
- Fig. 21            Photoluminescence spectra in radiative recombination including an LA-phonon emission from SCEHL and free excitons in pure Ge. Abscissa gives an emitted photon energy in the recombination. Incident power is

170 mW. Spectral resolution is indicated in the figure. These data have been taken under a steady-state excitation at temperatures indicated.

Fig. 22 Luminescence spectra from SCEHL and excitons in pure Ge and in Ge/Zn-1 at 4.2 K with a cw-laser power of 400 mW corresponding to an incident power of 200 mW. Abscissa gives photon energy. Symbols  $\gamma$  and  $\alpha$  denote bound excitons and bound double excitons captured by neutral Zn impurities.<sup>74)</sup> These spectra are taken without spatial resolution.

Fig. 23 Steady-state spectra of the LA- and TA-assisted luminescence from e-h drops in pure Ge, Ge/Zn-1 and Ge/Zn-2 at 1.7 K. The incident power  $P_{inc}$  of the laser is calibrated to be 240 mW.

Fig. 24 Time-resolved spectra from e-h drops are obtained at 1.7 K in pure Ge for various delay times between 0 and 300  $\mu$ s. The abscissa is scaled by wavelength on the bottom, while by photon energy on the top. The laser power of 300 mW corresponds to  $P_{inc} = 180$  mW. Pulse duration of the laser 100  $\mu$ s.

Fig. 25 The time-resolved spectra in Ge/Zn-1 at delay times between 0 and 60  $\mu$ s at 1.7 K. The laser pulse has a 100  $\mu$ s duration and a 500 mW power, corresponding to  $P_{inc} = 300$  mW.

Fig. 26 Time-variation of the photoluminescence intensity of the LA-line from SCEHL after the laser pulse at 1.7 K. The intensity is plotted in a logarithmic

scale. Circles and triangles are the experimental data. Solid lines indicate exponential decay of the intensity with lifetimes, 150  $\mu\text{s}$  in pure Ge, 30  $\mu\text{s}$  in Ge/Zn-1 and 10  $\mu\text{s}$  in Ge/Zn-2.

Fig. 27

Photoluminescence spectra for LA-phonon assisted lines in pure Ge with and without strain at 4.2 K (solid lines). In an unstrained sample, ordinary droplets and free excitons are observed (the upper trace). Open circles give a fitting result with the band-bottom energies for the droplets and the excitons,  $E_G' = 705.6$  meV and  $E_G^X = 713.4$  meV, and the Fermi energies,  $E_{Fe} = 2.2$  meV and  $E_{Fh} = 3.6$  meV. The sample is illuminated by unfocussed laser beam having a spot radius of  $\sim 1$  mm and an incident power of 150 mW. The spatially resolved spectra at the well in a strained sample have been taken at 30  $\mu\text{s}$  after the focussed excitation pulse (the lower trace). The dashed line labelled  $\gamma$  is the component in the theoretical spectra from SCEHL and free excitons in the excitonic shell. The other line  $\alpha$  is that from ordinary droplets and coexisting free excitons around the well. The total intensity (open circles) is given as an addition of the  $\gamma$ - and  $\alpha$ -components. Fitting parameters for the  $\gamma$ -component are as follows:  $E_G'$  of SCEHL and  $E_G^X$  of the excitons in the shell are 705.5 and 710.6 meV, and the Fermi energies  $E_{Fe}$  and  $E_{Fh}$  are 2.4 and 1.6 meV. The parameters for the  $\alpha$ -component are the same as in the unstrained

sample. The position of the focussed beam with  $P_{inc} = 230$  mW is  $\sim 0.3$  cm away from the center of the well towards the other end of the sample diameter.

Fig. 28 Luminescence from SCEHL and ordinary droplets in pure Ge and in Ge/Be 722-21.5 with the spatial resolution technique at 1.8 K under cw-excitation. The laser beam is focussed at about 0.3 cm away from the center of the well. The incident power of the laser is 50 mW or less in pure Ge, or 180 mW in Ge/Be 722-21.5. Solid lines are experimental traces. Open circles are theoretical fits comprising the luminescence lines due to SCEHL and the ordinary droplets (dashed lines).

Fig. 29 Steady-state spatial distribution of the luminescence from SCEHL and droplets in pure Ge at 1.8 K. The absorbed power  $P_{abs}$  of 33 mW is calibrated after ref.38, and given by  $P_{abs} = 0.47 P_{inc}$ . The spatial resolution is indicated within the frame.

Fig. 30 The spatial distribution of SCEHL and the ordinary droplets in pure Ge at 1.8 K with  $P_{abs} = 67$  mW. The dashed line is drawn just as a guide. The radius used in the fitting is up to 400  $\mu\text{m}$ .

Fig. 31 The spatial distribution in Ge/Zn-1 at 1.8 K with  $P_{abs} = 71$  mW (solid circles).

Fig. 32 The intensity distribution of SCEHL around  $X_S = 0.36$  cm, ordinary droplets (EHD) and free excitons (FE) in pure Ge at 4.2 K with  $P_{abs} = 63$  mW. The dashed lines serve as a guide.

- Fig. 33            The spatial distribution including SCEHL, droplets, free and bound excitons (BE) in Ge/Zn-1 at 4.2 K with  $P_{\text{abs}} = 72$  mW. The dashed lines serve as a guide.
- Fig. 34            Time-decay of the LA-phonon assisted luminescence intensity of SCEHL in pure Ge. Open circles are the experimental data normalized at 0  $\mu\text{s}$  and plotted in log-scale. Solid lines are fitting by eqs.(2-56a) and (2-56b). The dashed line denoted as  $I_x$  corresponds to the expected time decay of free excitons in the surrounding shell from the equations. The incident power is 280 mW and the beam is focussed onto a surface region near the well.
- Fig. 35            Temperature dependence of the lifetime of SCEHL in pure Ge determined from the fitting.
- Fig. 36            Recombination rate as the inverse of the lifetime of SCEHL in pure Ge. This is connected with the e-h density at each temperature. The solid line is a fitting line by eq.(2-59) with  $A = 0$ .
- Fig. 37            Luminescence spectra from bound excitons and bound excitonic complexes as well as free excitons at 4.2 K. Bottom: free-exciton lines in pure Ge. Middle: bound-exciton line and bound-multiexciton line are denoted as  $BE_{\text{LA}}$  and  $BME_{\text{LA}}$  in Ge/In-1. Top: bound-exciton and bound-double-excitons lines are labelled as  $BE_{\text{LA}}$  and  $BDE_{\text{LA}}$  in Ge/Be 722-21.5.
- Fig. 38            Incident-power dependence of the intensity of LA-

phonon assisted line of ordinary droplets in pure Ge at 4.2 K. Threshold power  $P_{th}$  is 85 mW.

Fig. 39 Time-decay profile of free-exciton luminescence after the laser pulse in pure Ge, in Ge/Be 722-21.5 and in Ge/In-1. Circles and triangles are the experimental data. The luminescence intensity is plotted in a logarithmic scale and normalized at 0  $\mu$ s. Solid lines serve fitting results using eq.(2-65). Used samples are unstrained.

Fig. 40 Luminescence intensity of SCEHL in Ge/In-1 measured at the LA-phonon assisted line. The intensity is plotted in a logarithmic scale and normalized at 0  $\mu$ s. Dopant concentration in Ge/In-1 is indicated. Open circles are data points and solid lines are fitting curves drawn by the rate equations.

Fig. 41 The lifetime of SCEHL in Ge/In-1 against temperature. These points are given by fittings with the rate equations.

Fig. 42 Normalized LA-phonon assisted line of SCEHL in Ge/In-2 with a dopant concentration of  $3.7 \times 10^{14} \text{ cm}^{-3}$  plotted in a logarithmic scale against delay time. Solid lines are fitting curves with the same Richardson coefficient  $A_R$  as used in Figs. 34 and 40.

Fig. 43 Impurity-induced recombination rate given by subtracting the intrinsic recombination rates,  $B_n$  and  $C_n^2$  from the inverse of the lifetime,  $1/\tau_0$ , within SCEHL in Ge/In-2. The dashed line corresponds to the

mean value among the recombination rates below 3.2 K.

Fig. 44 Normalized LA-phonon assisted luminescence line of SCEHL in Ge/In-3 plotted in a logarithmic scale (open circles). The data are well fitted by an exponential decay with a lifetime of 46  $\mu$ s (solid line).

Fig. 45 Normalized intensity of LA-phonon assisted luminescence line of SCEHL in Ge/Be 722-21.5 with a Be concentration of  $4.5 \times 10^{13} \text{ cm}^{-3}$  plotted in a logarithmic scale against delay time. Open circles are experimental data while solid lines are theoretical curves.

Fig. 46 Temperature dependence of the induced recombination rate by  $4.5 \times 10^{13} \text{ cm}^{-3}$  Be impurities within SCEHL.

Fig. 47 Normalized intensity of LA-phonon line in Ge/Be 727-15.0 with a Be concentration of  $1.0 \times 10^{15} \text{ cm}^{-3}$ . The intensity is plotted in a logarithmic scale.

Fig. 48 Normalized intensity of LA-phonon line in Ge/Zn-1 with a Zn concentration of  $1.2 \times 10^{14} \text{ cm}^{-3}$  between 4.2 and 1.8 K.

Fig. 49 Comparison of AWDR peaks between pure Ge, Ge/In-1 ( $N_A = 6.0 \times 10^{13} \text{ cm}^{-3}$ ), Ge/In-2 ( $N_A = 3.7 \times 10^{14} \text{ cm}^{-3}$ ), Ge/Be 722-21.5 ( $N_A = 4.5 \times 10^{13} \text{ cm}^{-3}$ ) and Ge/Zn-1 ( $N_A = 1.2 \times 10^{14} \text{ cm}^{-3}$ ) at 1.6 K. Using linear polarized millimeter waves. Ordinate and abscissa give 35 GHz magneto-absorption intensity and magnetic field, respectively. Magnetic field is almost parallel to  $\langle 110 \rangle$  direction in each sample except for that in

Ge/Zn-1, where the field is almost along the  $\langle 001 \rangle$  direction. Horizontal bars give ground levels for AWDR peaks in the order of presentation.

Fig. 50           Circular-polarized 35 GHz magneto-absorption traces in pure Ge at 1.8 K. Magnetic field is applied nearly parallel to  $\langle 001 \rangle$  direction. The right side correspond to the electron-active polarization (e), while the left to the hole-active (h). Open circles are theoretical fits by eq.(2-89).

Fig. 51           Linear-polarized magneto-absorption data in Ge/Zn-1 at 1.6 K, using 35 GHz waves at delay times between 30 and 140  $\mu$ s. Sharp peaks at magnetic fields below 0.5 T are cyclotron resonance peaks of free carriers. The e- and h-active AWDR peaks are labelled as e and h. Open circles are theoretical fitting by eq.(2-89) for the both peaks. The direction of magnetic field is almost along the  $\langle 001 \rangle$  direction.

Fig. 52           Carrier scattering rates versus delay time. Solid and open circles correspond to electron and hole scattering rates in pure Ge. Solid and open triangles correspond to those in Ge/Zn-1, which are replotted in the inset with an expanded time scale. Horizontal lines are drawn in the delay time region where e-h density in SCEHL appears to be constant. The magnetic fields are almost parallel to the (001)-type axis both in pure Ge and in Ge/Zn-1.

Fig. 53           Linear-polarized 35 GHz waves magneto-absorption

traces in Ge/In-1 at 1.6 K. Open circles are theoretical fits by eq.(2-89). Horizontal bars give the ground levels for the traces. Magnetic field is applied almost parallel to the  $\langle 110 \rangle$  direction.

Fig. 54 The AWDR in Ge/In-2 at delay times between 75 and 175  $\mu\text{s}$  at 1.6 K. The fundamental peak appears intensely at high field. The peak denoted CR just below 0.5 T corresponds to an electron cyclotron resonance. Higher-harmonic AWDR's are observed at fields lower than the fundamental-resonance field. Open circles are the theoretical fits. The magnetic field direction is almost parallel to the  $\langle 110 \rangle$  direction.

Fig. 55 Carrier scattering rates within SCEHL in Ge/In-1 (solid triangles) and in Ge/In-2 (open triangles) plotted against delay time at 1.6 K.

Fig. 56 The AWDR peaks observed in linear-polarized 35 GHz waves magneto-absorption intensity in Ge/Be 722-21.5 at 1.6 K. The e- and h-active modes are labelled e and h. Open circles correspond to theoretical fittings by eq.(2-89) for the both modes. Horizontal bars are the ground levels for each trace. Applied magnetic field is almost parallel to the  $\langle 110 \rangle$ -type axis.

Fig. 57 Circular-polarized 35 GHz magneto-absorption due to photoexcited systems in Ge/Be 722-21.5 at 50  $\mu\text{s}$  after the photopulse at 1.8 K. The direction of magnetic fields is slightly tilted from the  $\langle 110 \rangle$  direction. The right side corresponds to the e-active

polarization (e) and the left to the h-active (h).

Fig. 58 Delay-time dependence of the scattering rates in Ge/Be 722-21.5 at 1.6 K. Open circles are for holes while the solid for electrons. Horizontal lines are drawn in the delay-time region where the scattering rates seem to be constant.

Fig. 59 Linear-polarized 35 GHz waves magneto-absorption trace at 10  $\mu$ s after the excitation pulse at 1.6 K. The AWDR peak is only feebly observable at  $\sim$ 1.8 T. The trace magnified by 5 times is also shown.

Fig. 60 Radius decay of SCEHL in Ge/Zn-1 at 1.6 K. Radius is plotted in a logarithmic scale.

Fig. 61 Radius decay in three doped samples at 1.6 K. Ordinate is plotted in a logarithmic scale.

Fig. 62 Resonance-field dependence of AWDR amplitude. Ordinate and abscissa are plotted in a logarithmic scale. The data (a), (b), (d) and (e) are taken at 1.6 K, while (c) at 1.8 K.

Fig. 63 Linear-polarized 35 GHz waves magneto-absorption due to photoexcited carriers and SCEHL in Ge/In-1 at various temperatures between 4.2 and 1.6 K. Magnetic field is almost parallel to the  $\langle 110 \rangle$ -type axis. The CR-labelled lines are cyclotron resonance of electrons. Open circles are theoretical fits by eq.(2-89). Horizontal bars correspond to the ground levels for the traces in the order of presentation.

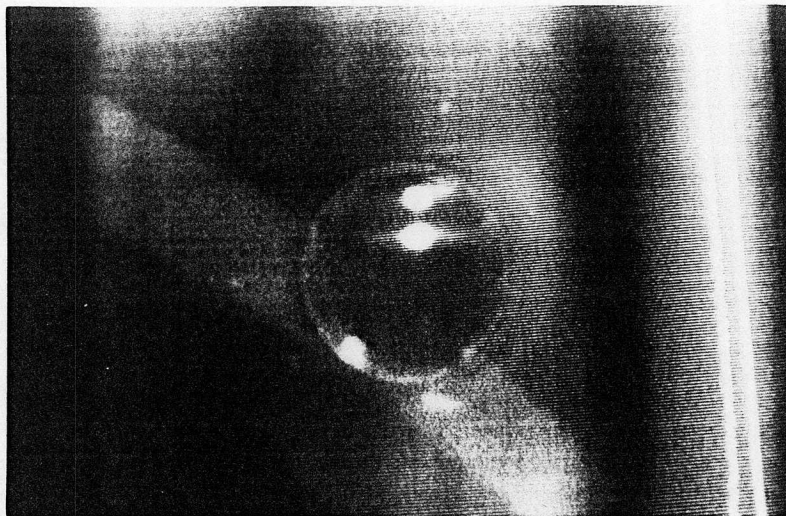
Fig. 64 Linear-polarized 35 GHz waves magneto-absorption

caused by photoexcited systems in Ge/Be 722-21.5 at various temperatures between 4.2 and 1.6 K. Magnetic field is applied almost along the  $\langle 110 \rangle$  direction. The peak denoted CR is due to cyclotron resonance of electrons. Open circles are theoretical fits. Horizontal bars give the ground levels. The e- and h-active AWDR peaks are denoted as e and h.

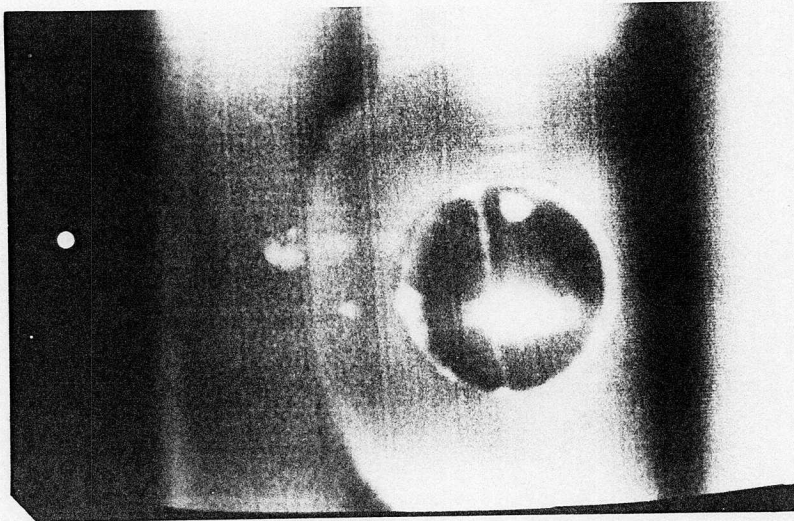
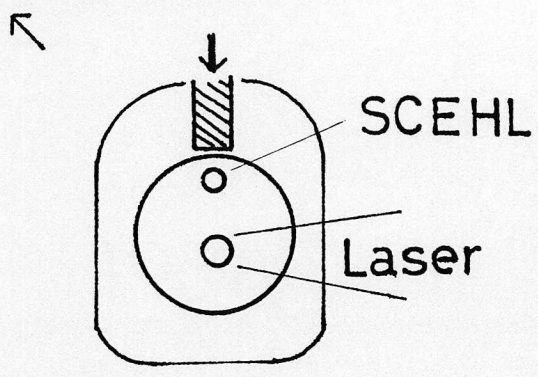
Fig. 65 Scattering rates for carriers in SCEHL plotted against  $T^2$ . Bold line corresponds to the carrier-carrier scattering observed in AWDR in pure Ge,<sup>42)</sup> and is expressed as  $1/\tau_{e-h} = a + bT^2$  ( $s^{-1}$ ) with  $a = 1.4 \times 10^{10} s^{-1}$  and  $b = 1.2 \times 10^9 K^{-2} s^{-1}$ . Scattering rates in Ge/In-1 are solid triangles. Scattering rates both for electrons and for holes in Ge/Be 722-21.5 are given by solid circles and by open circles, respectively.

Fig. 66 Induced scattering rates by Be impurities for electrons (e) and holes (h) within SCEHL in Ge/Be 722-21.5. Abscissa is temperature.

Fig. 67 Far-infrared magneto-absorption traces due to SCEHL in pure Ge obtained at 4.2 and 1.8 K. With a delay-time of 20  $\mu s$  after the light pulse. Far-infrared wavelength is 220  $\mu m$ . The horizontal bar is the ground level for the trace at 4.2 K. Magnetic field is almost parallel to the  $\langle 001 \rangle$  direction.



Pure Ge



Ge/In-1

Fig. 1

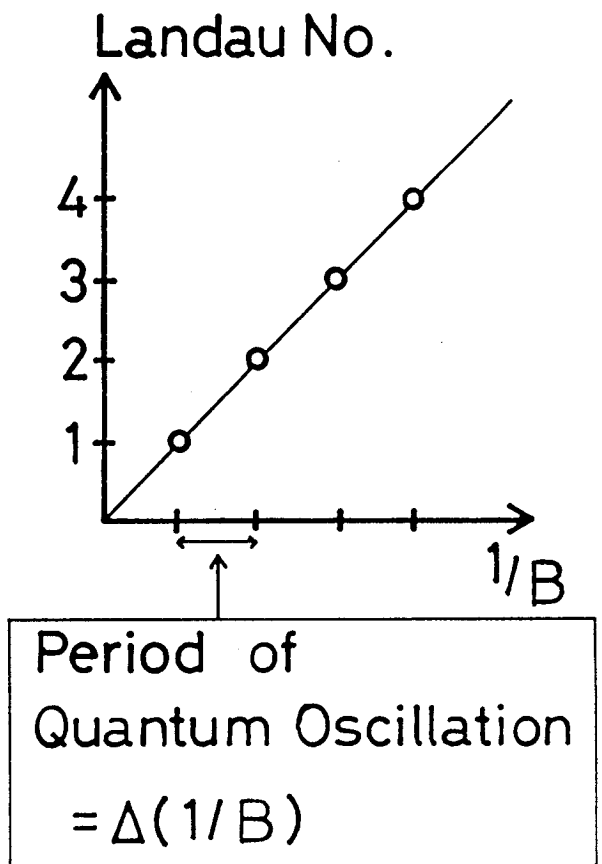
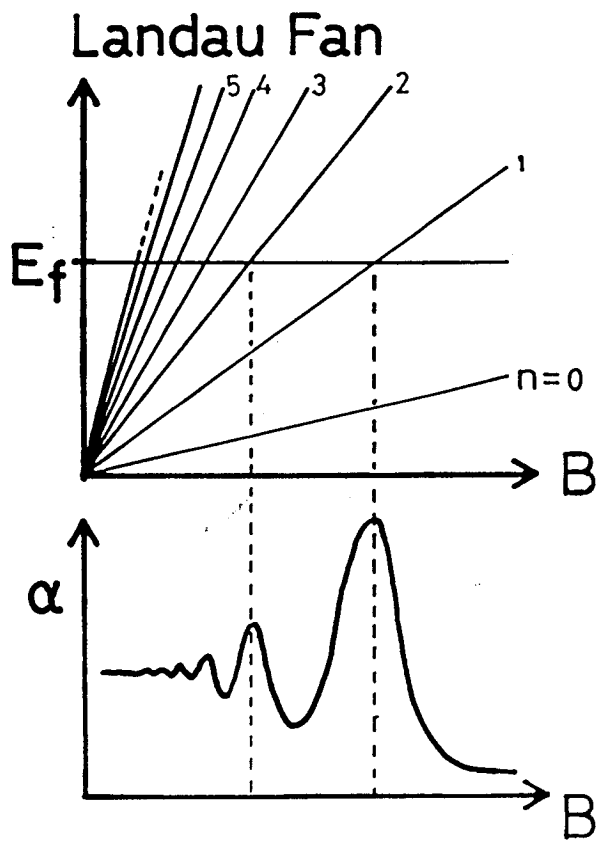
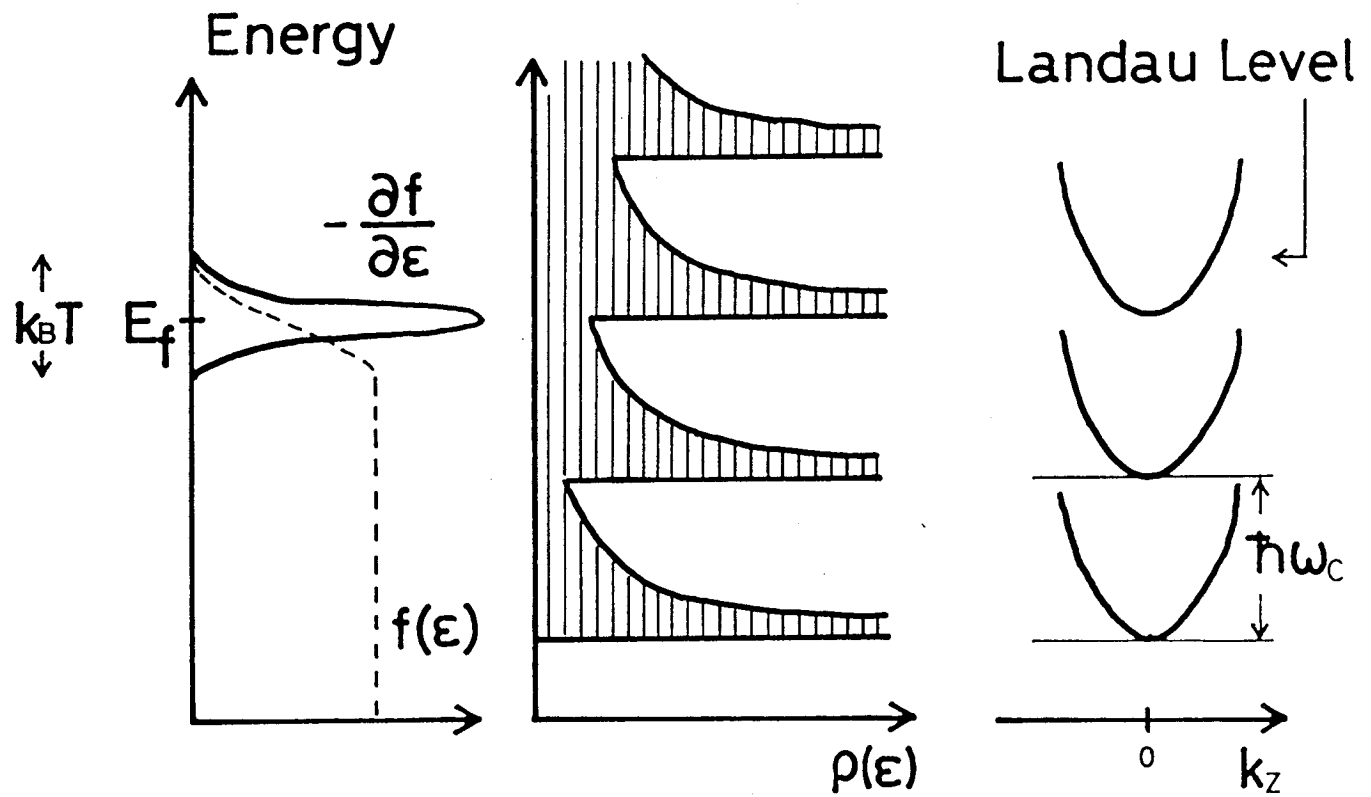


Fig. 2

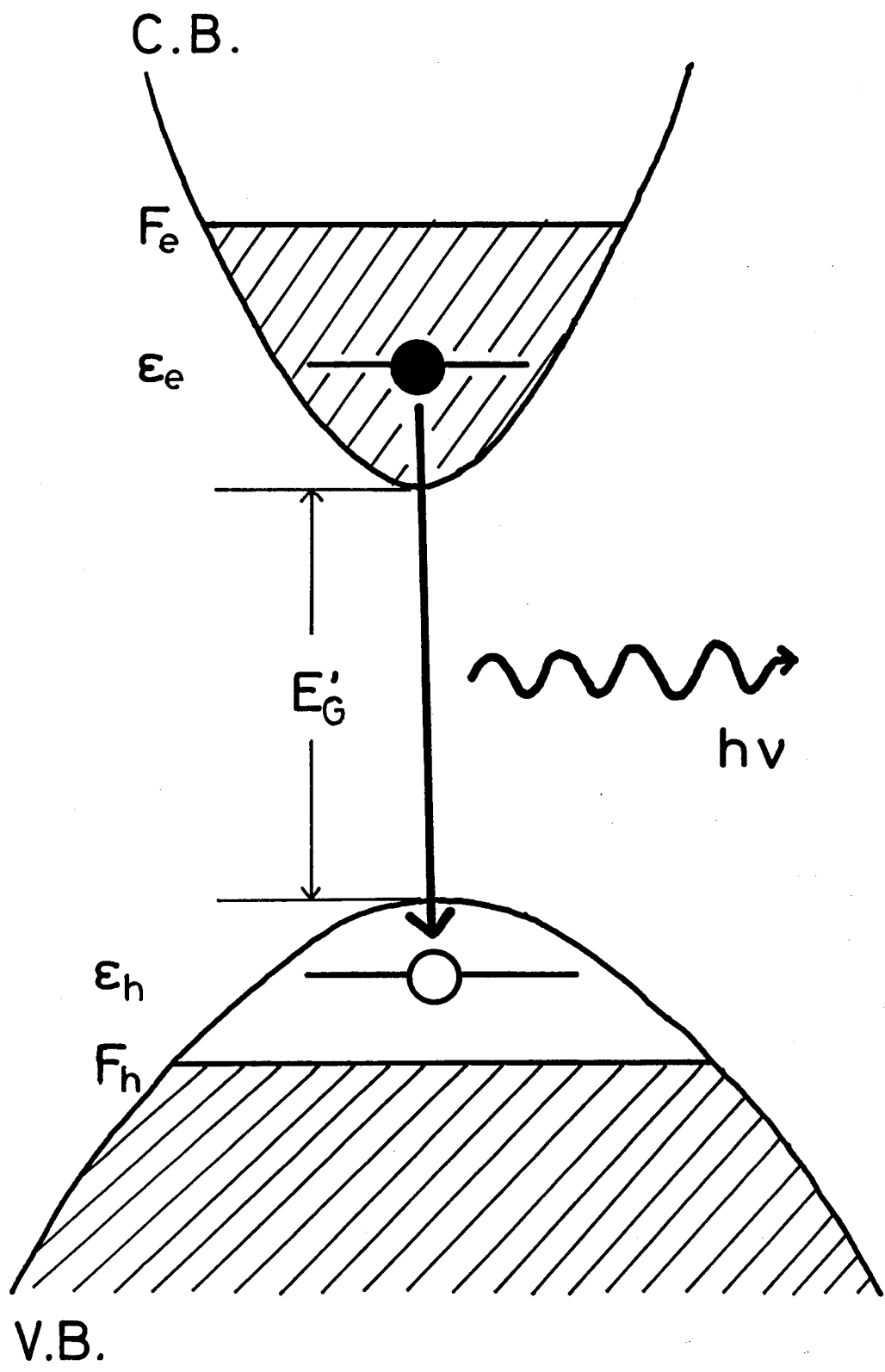


Fig. 3

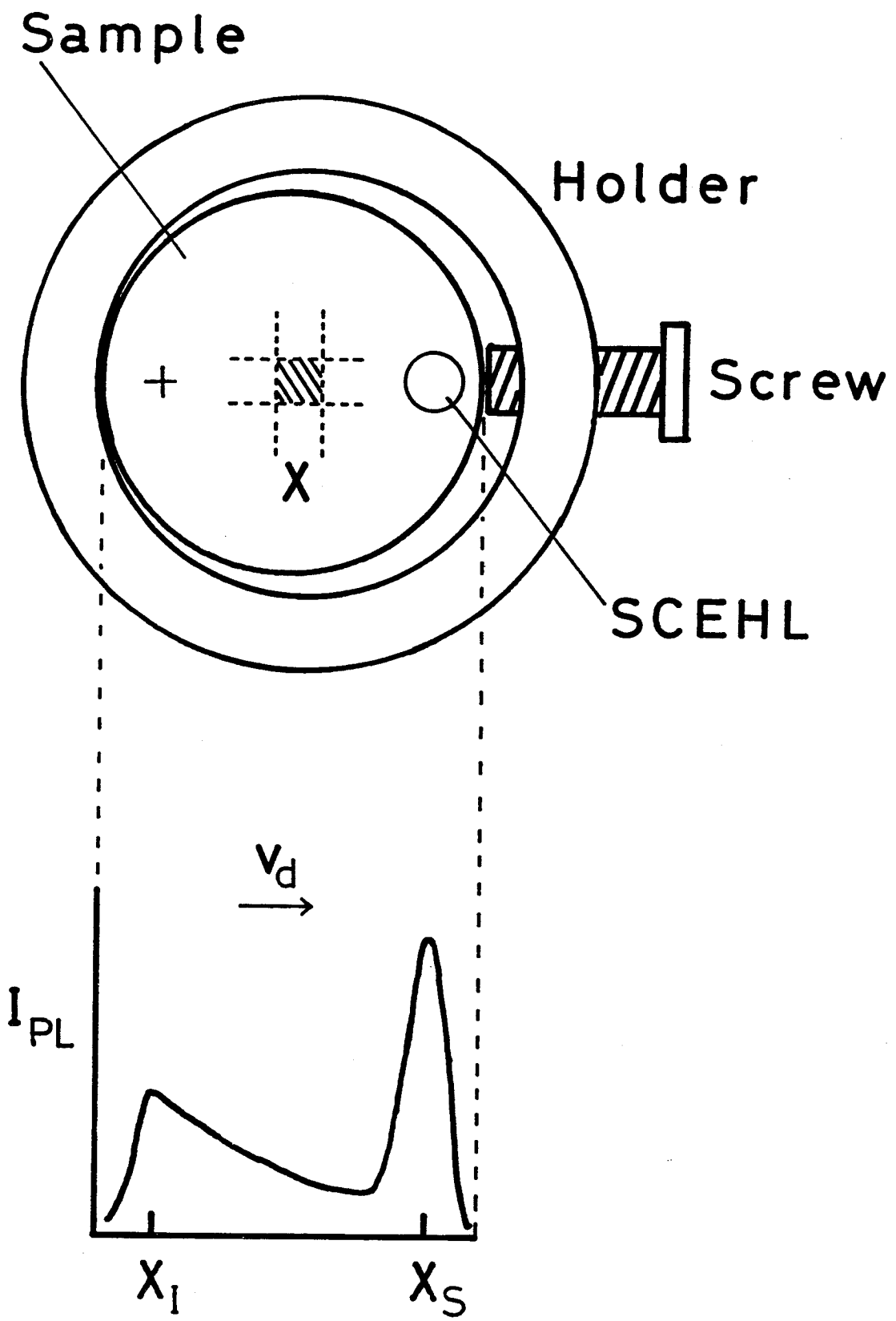


Fig. 4

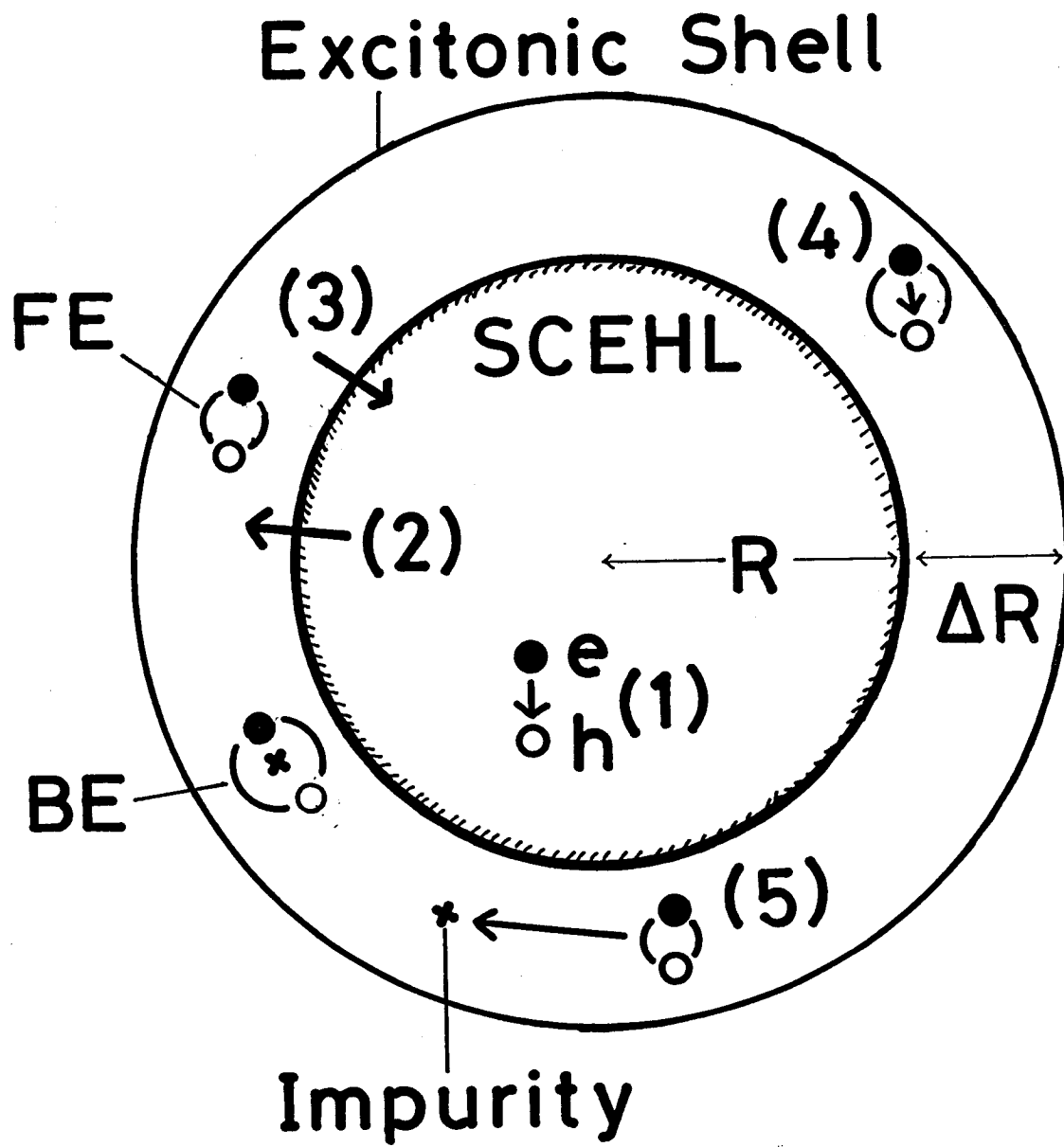


Fig. 5

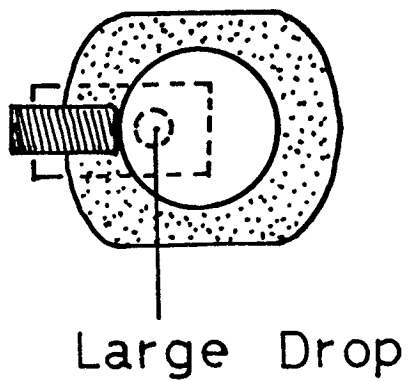
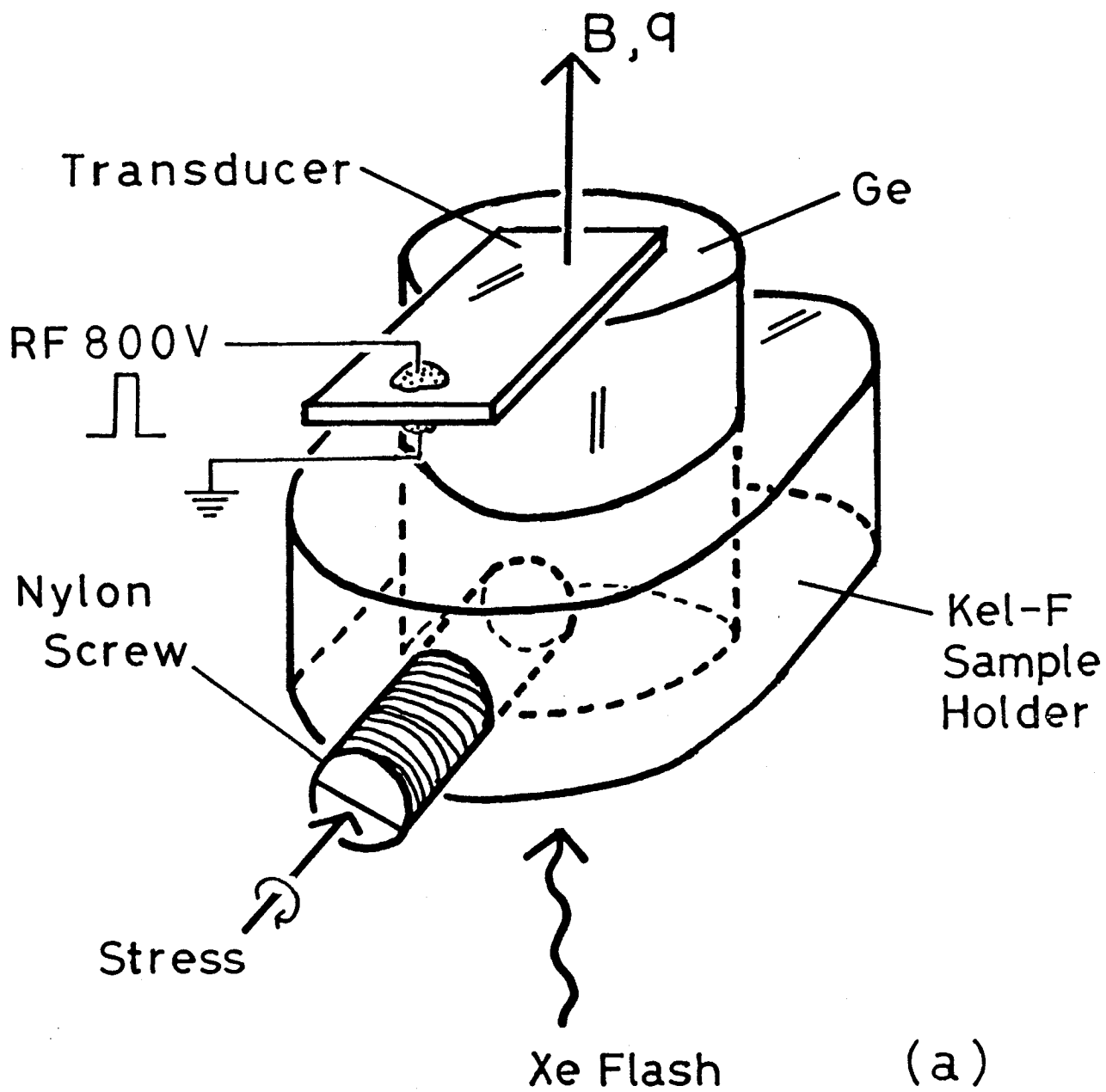


Fig. 6

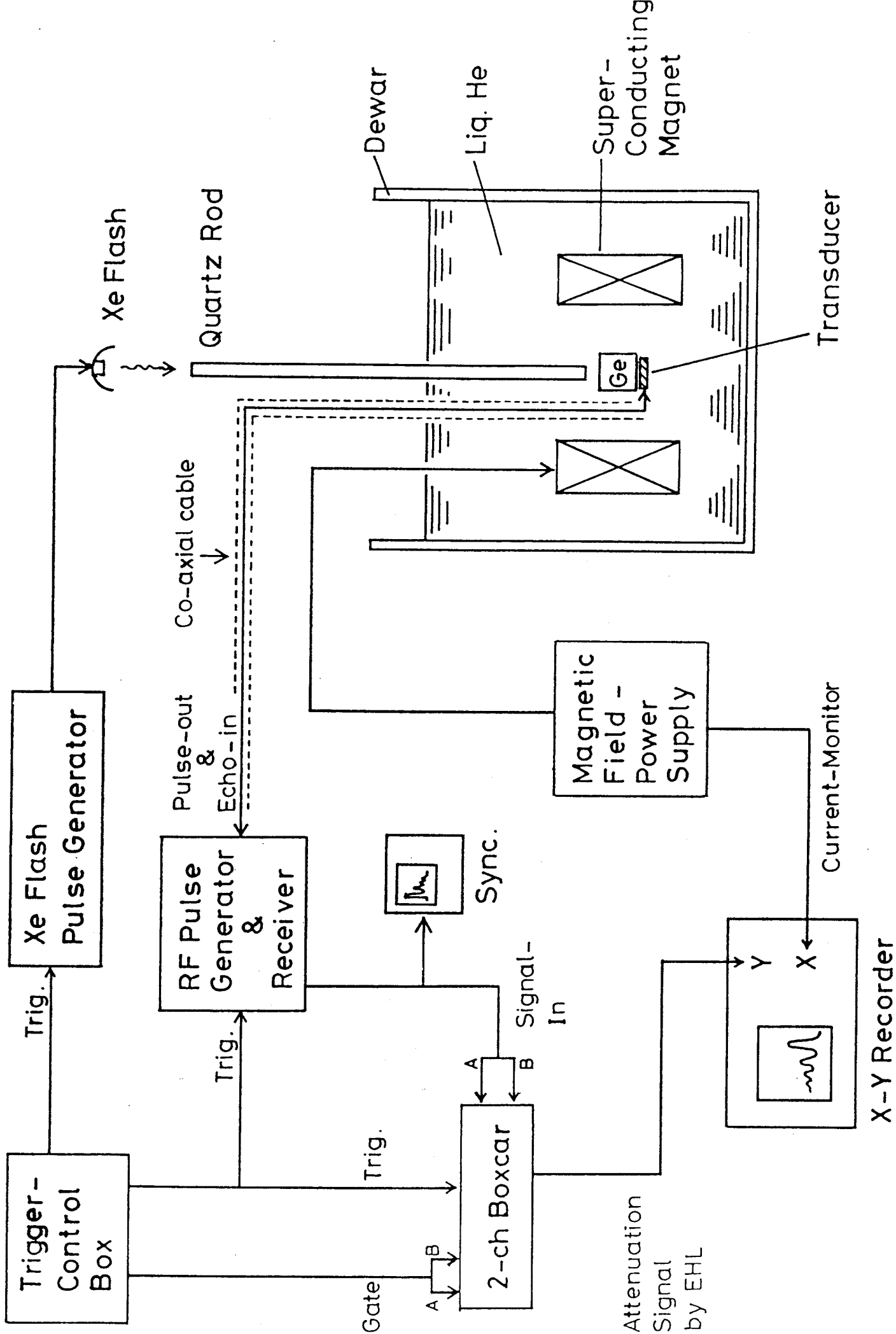


Fig. 7

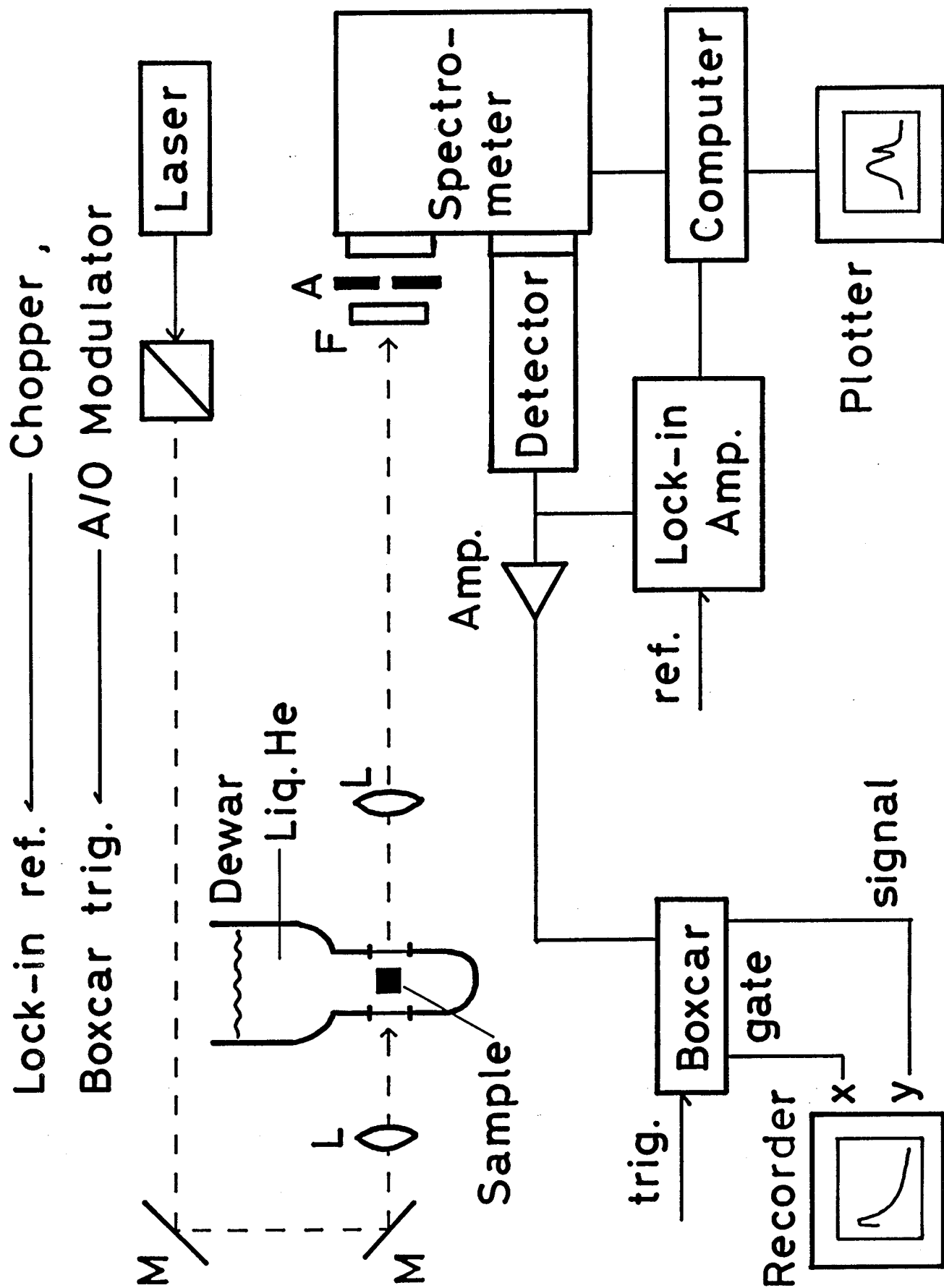


Fig. 8

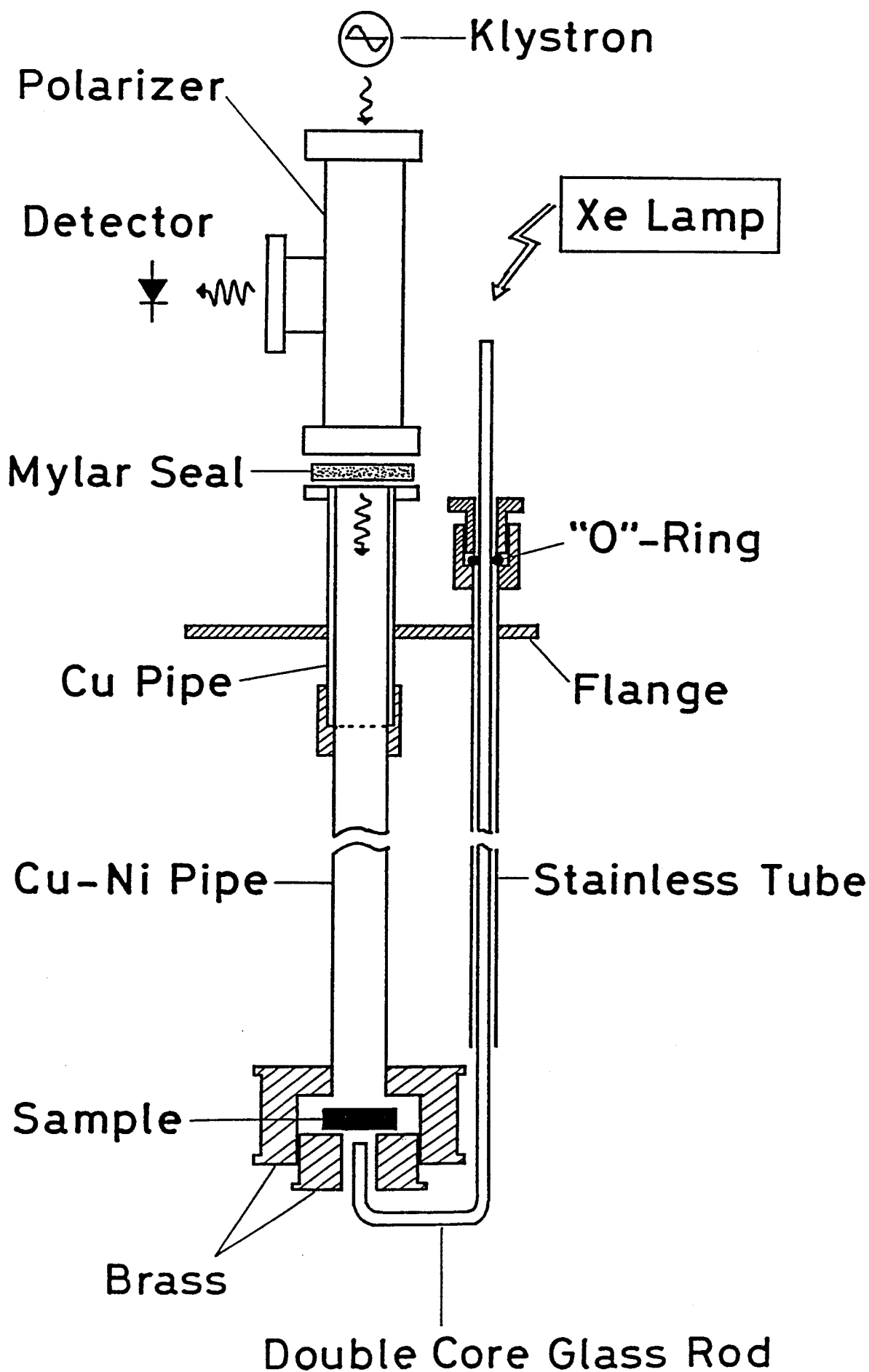


Fig. 9

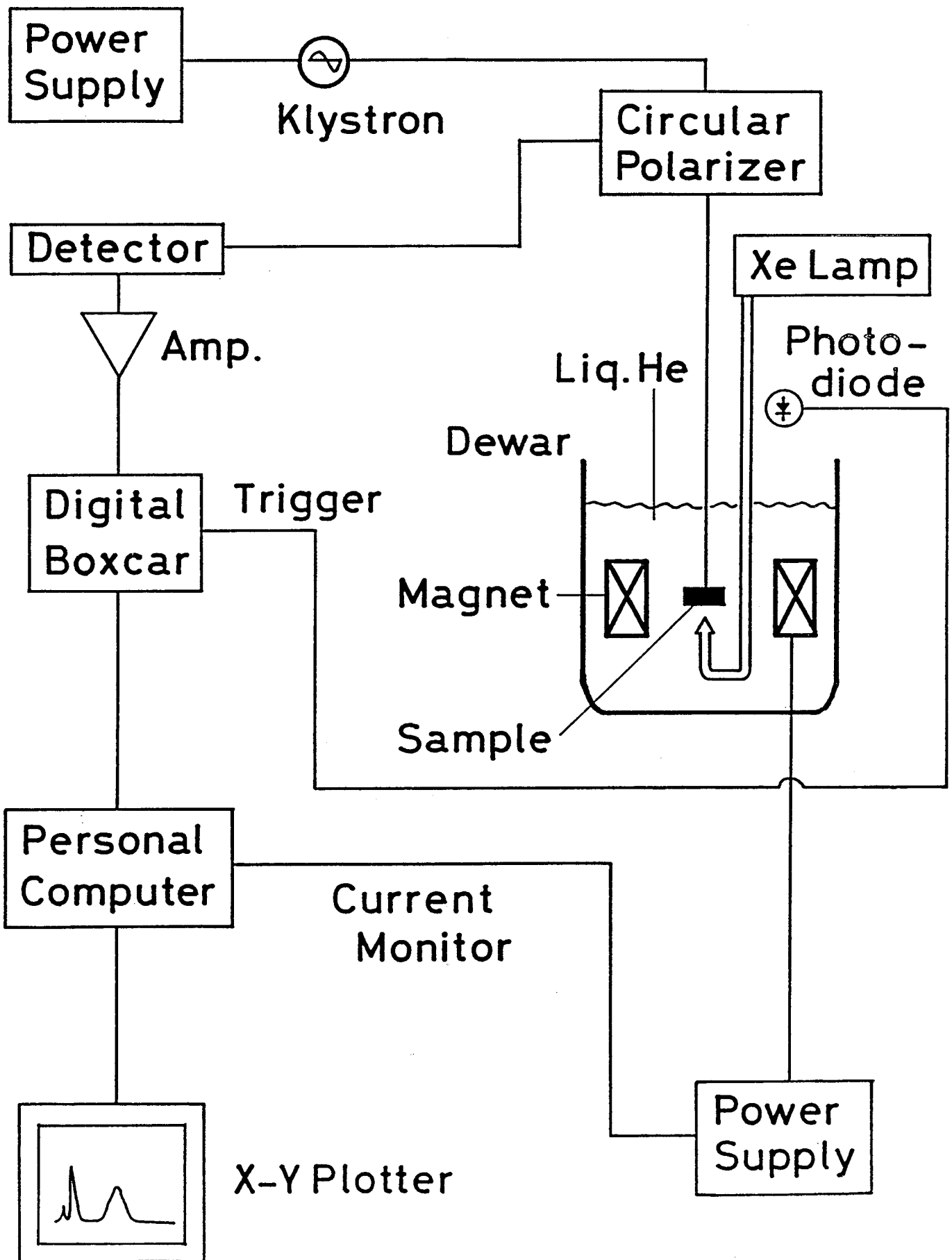


Fig. 10

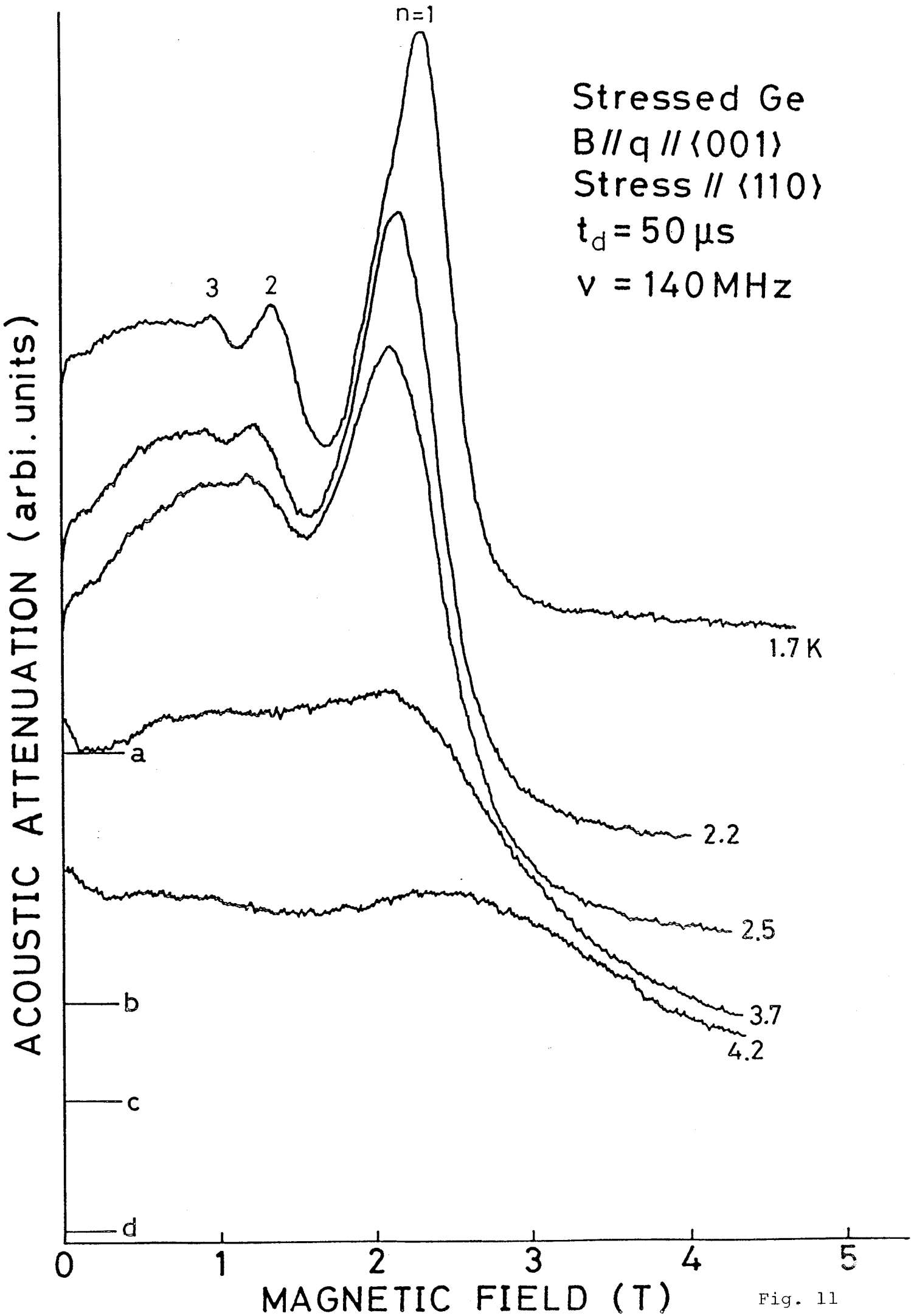


Fig. 11

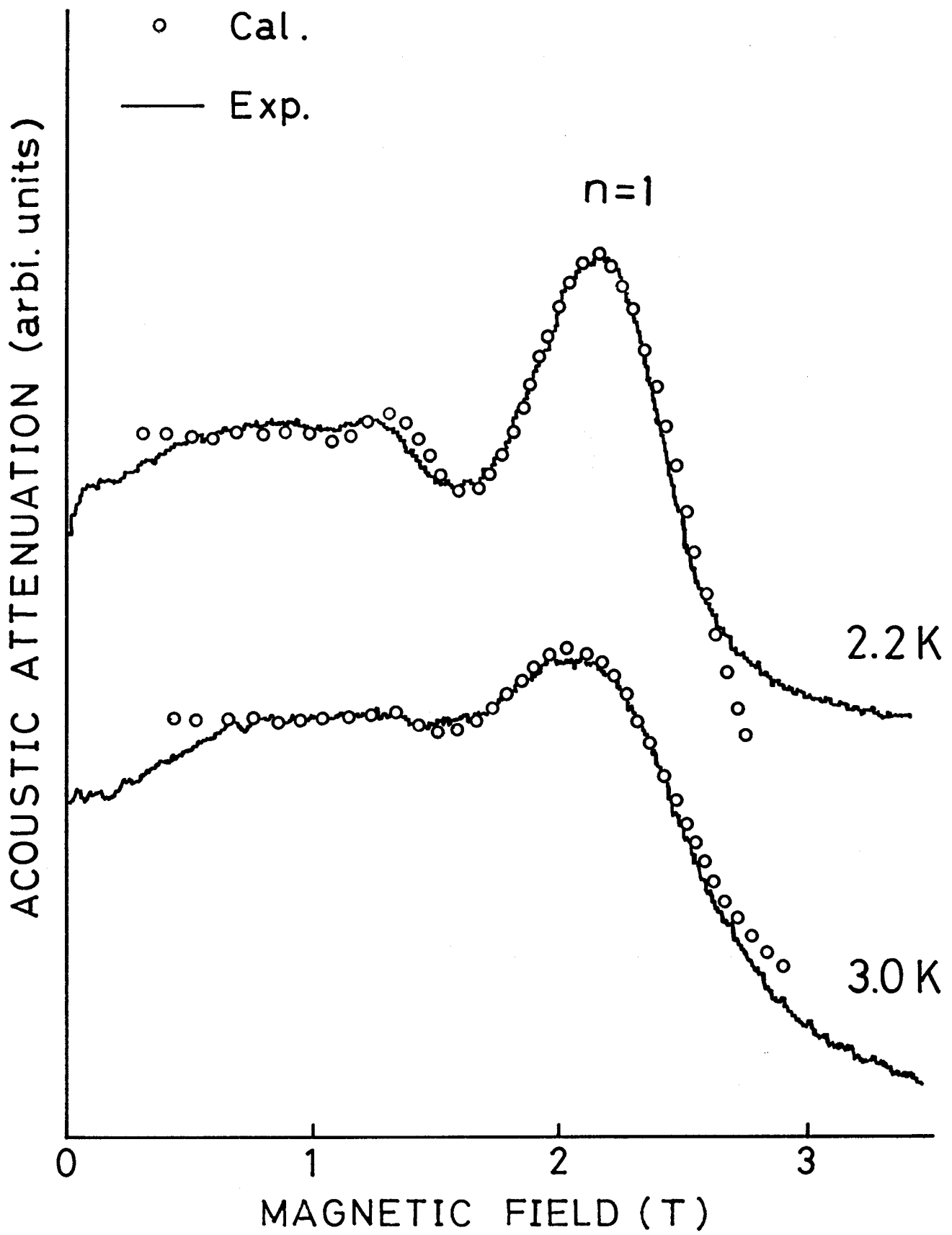


Fig. 12

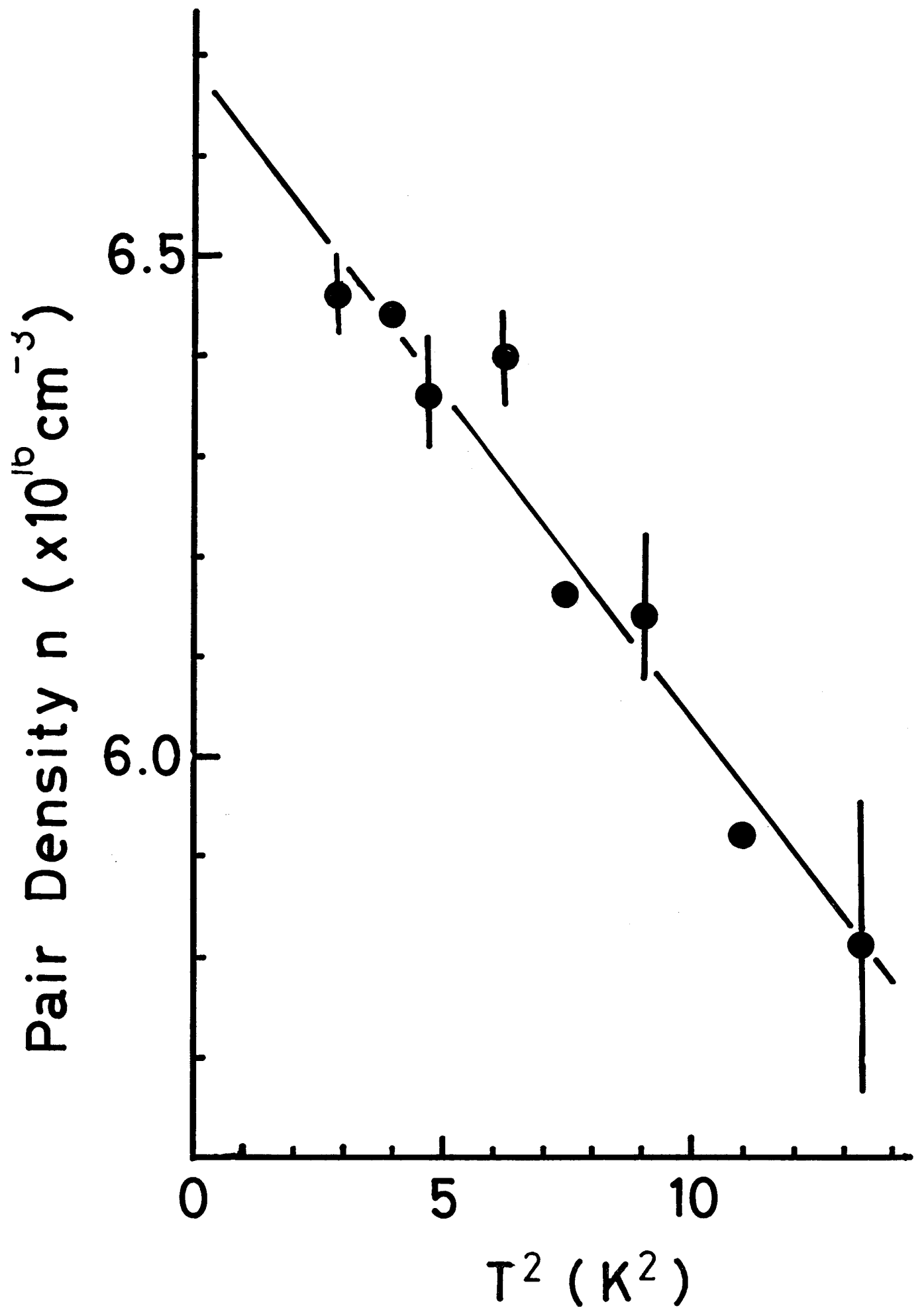


Fig. 13

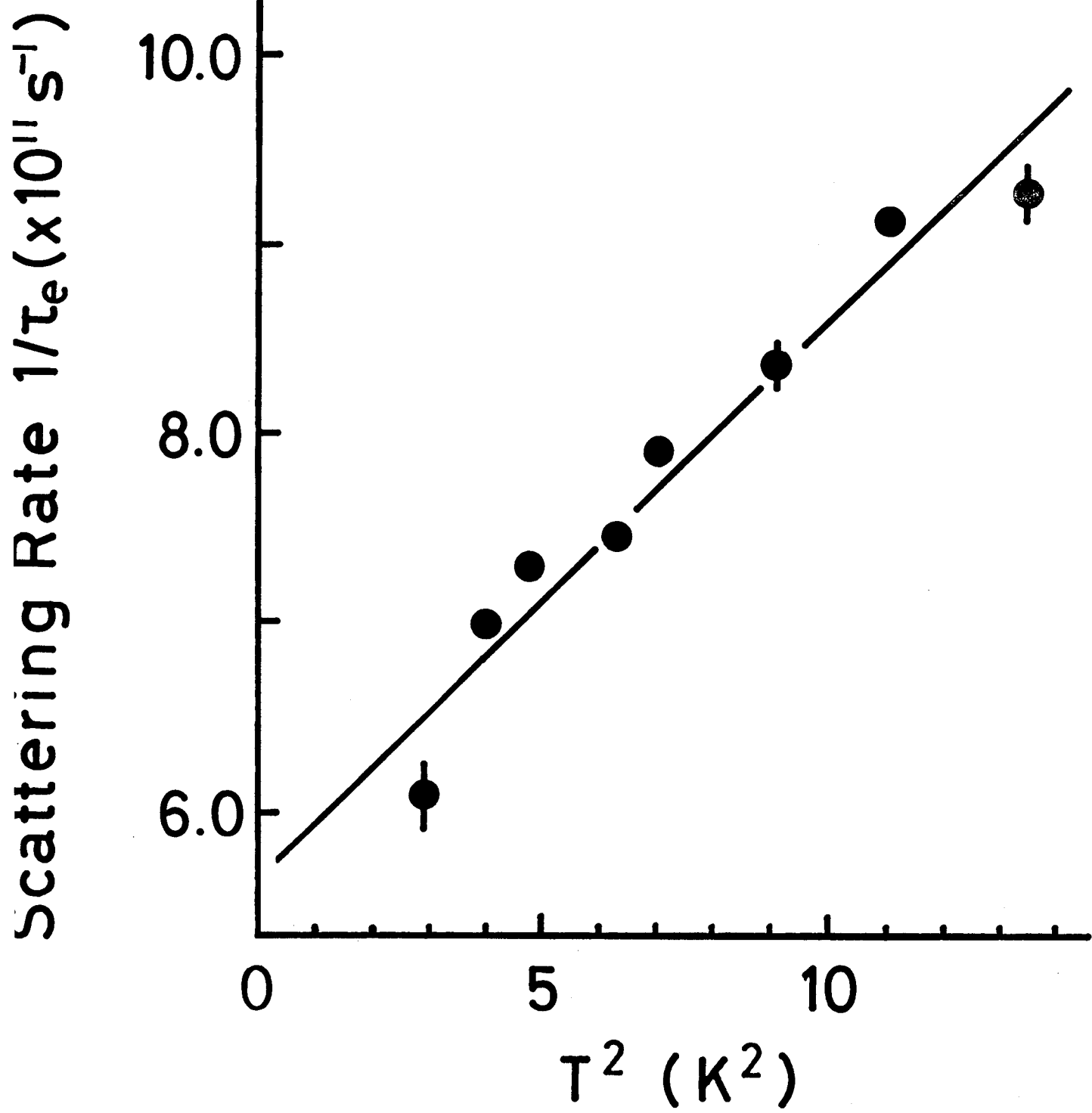


Fig. 14

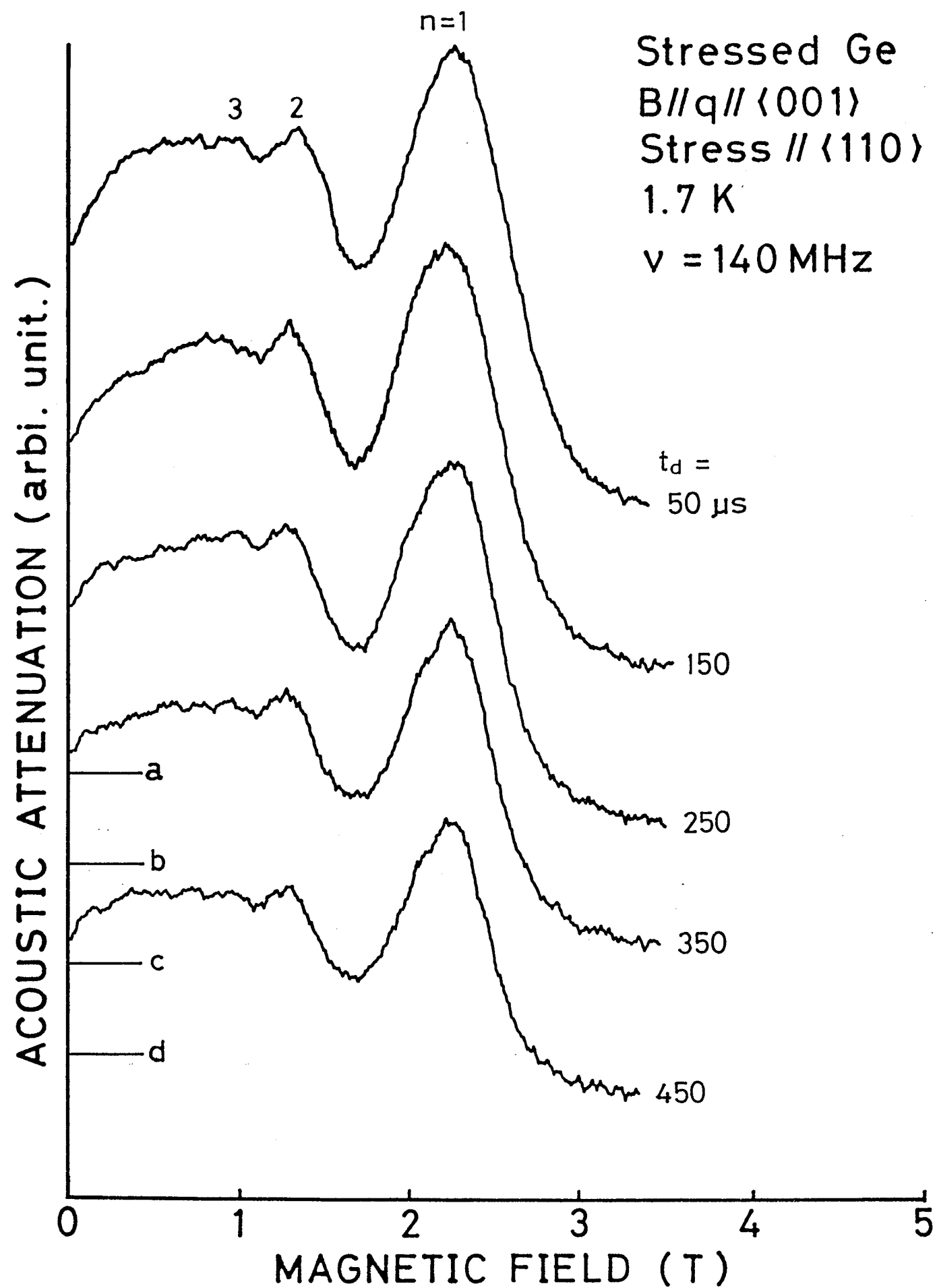


Fig. 15

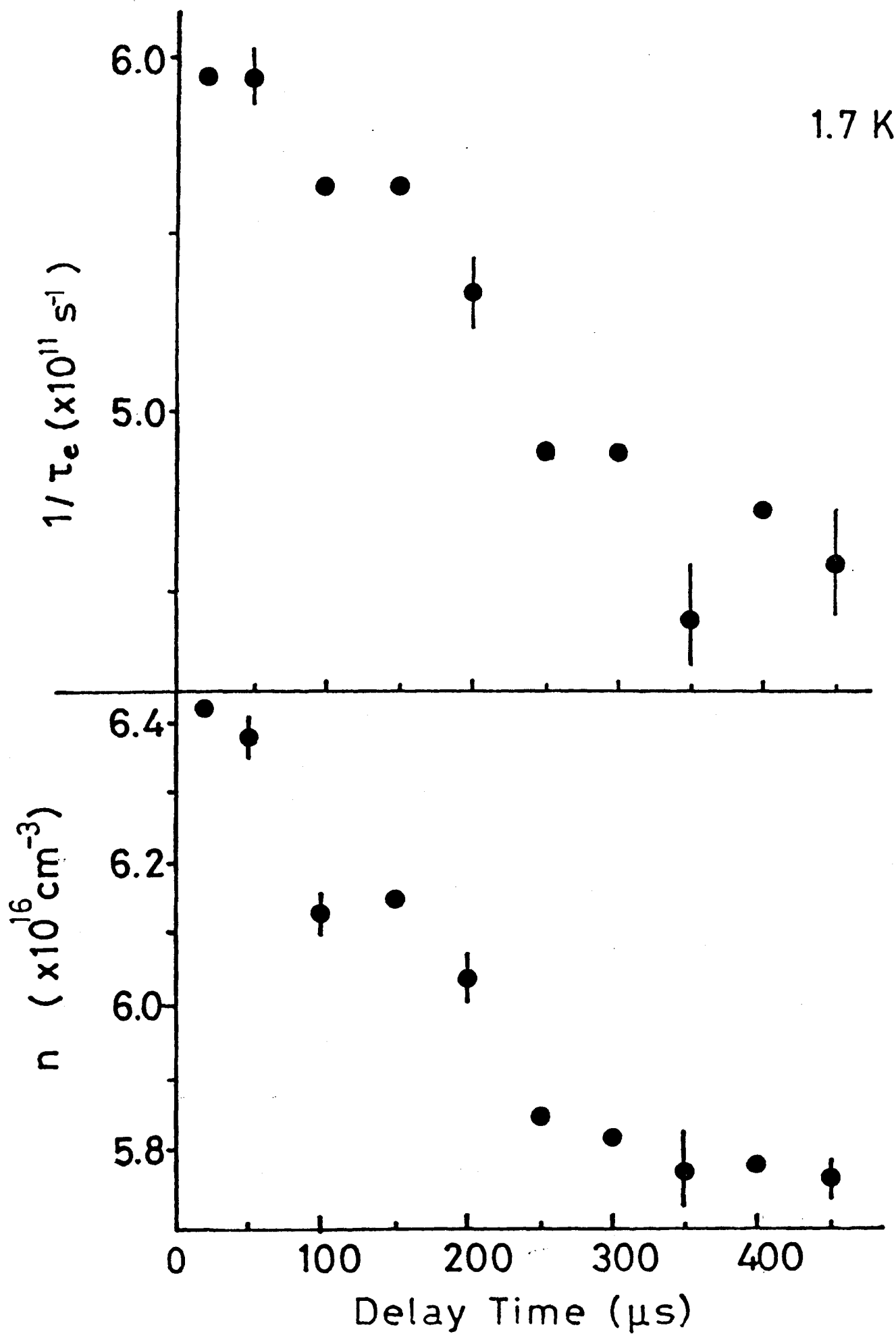


Fig. 16

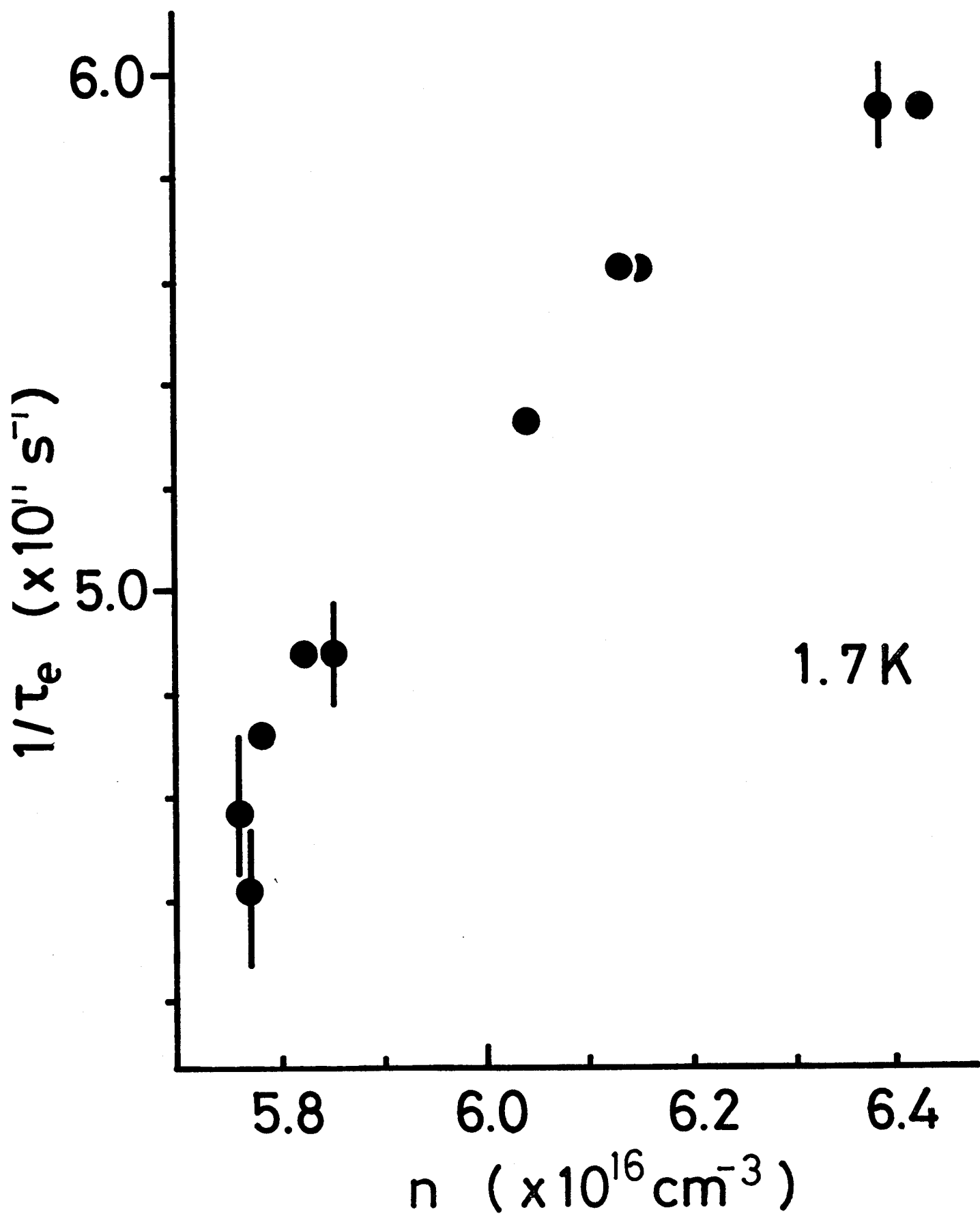


Fig. 17

Stressed Ge  
 $\nu = 180 \text{ MHz}$   
 $t_d = 140 \mu\text{s}$

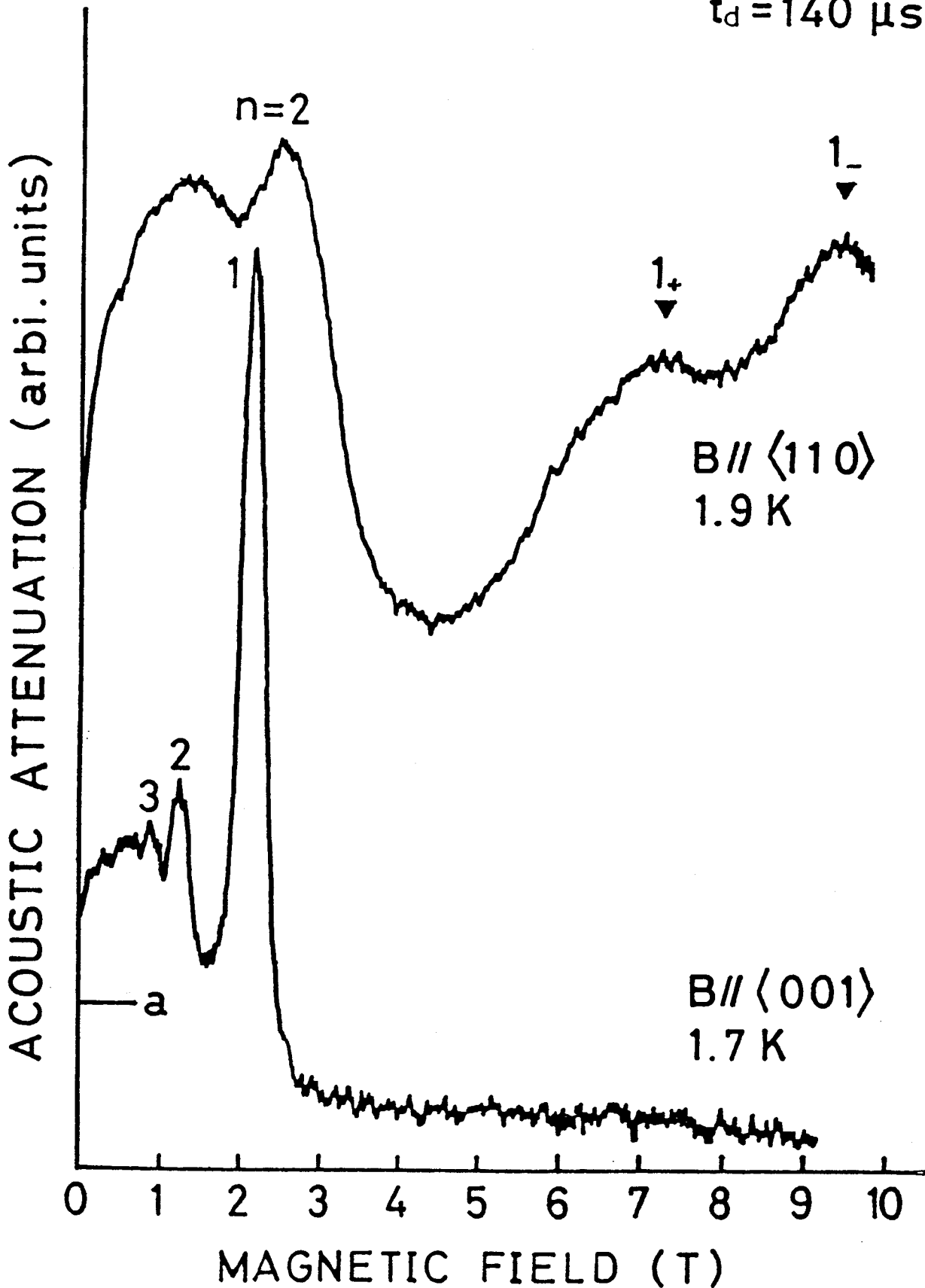


Fig. 18

180 MHz

1.9 K

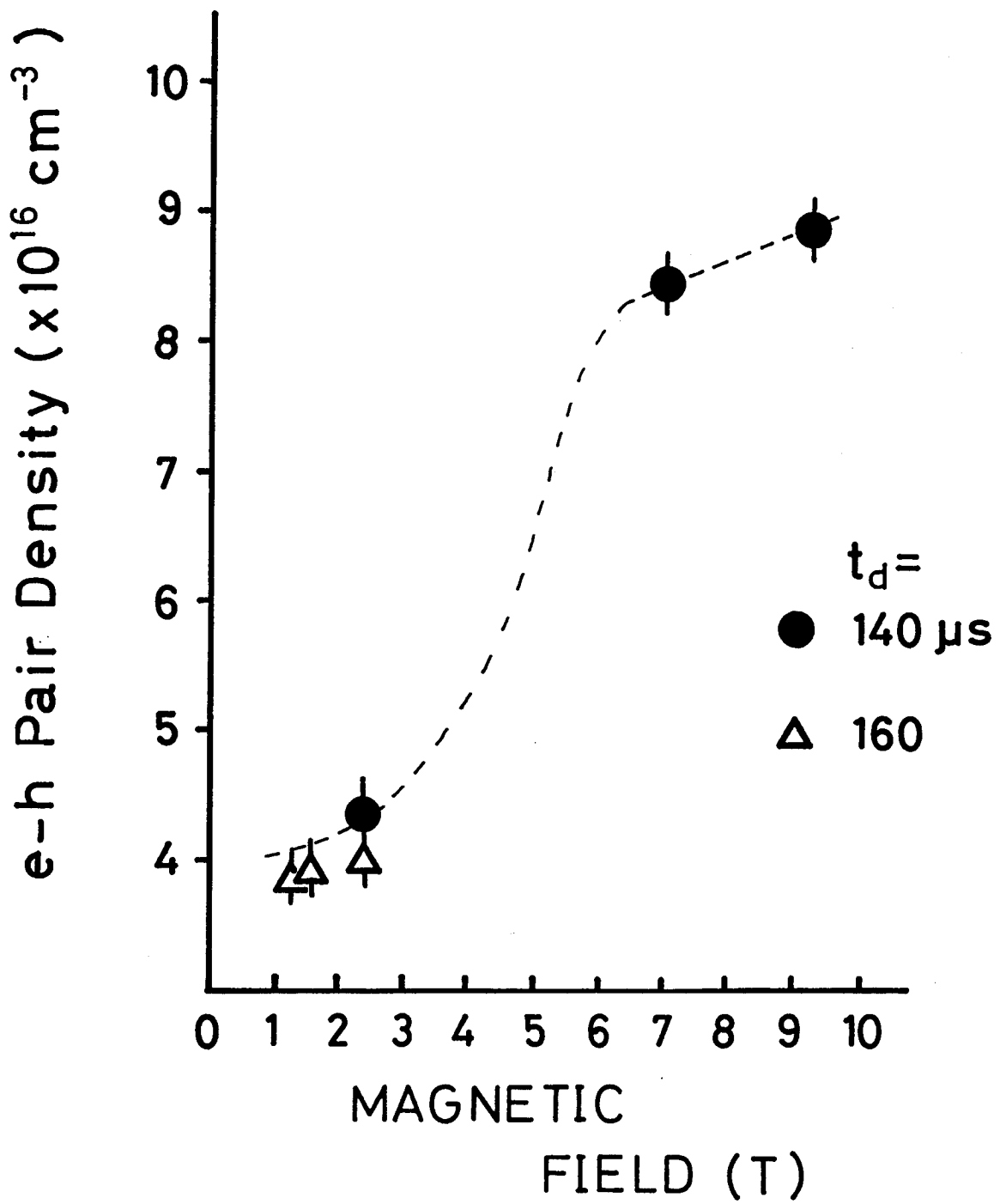


Fig. 19

Stressed Ge/In      180 MHz  
B//q// <110>       $t_d = 60 \mu s$       1.9 K

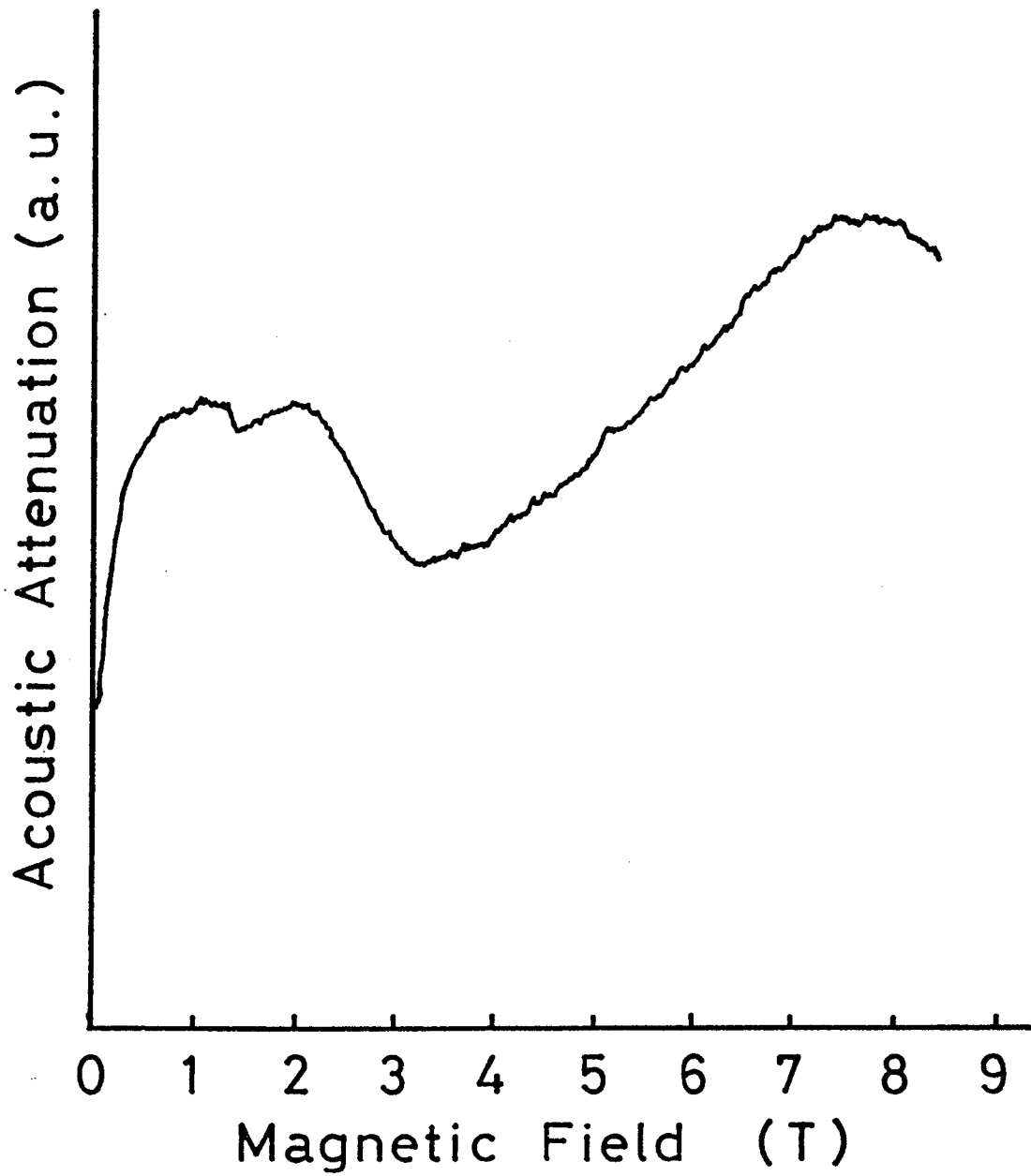


Fig. 20

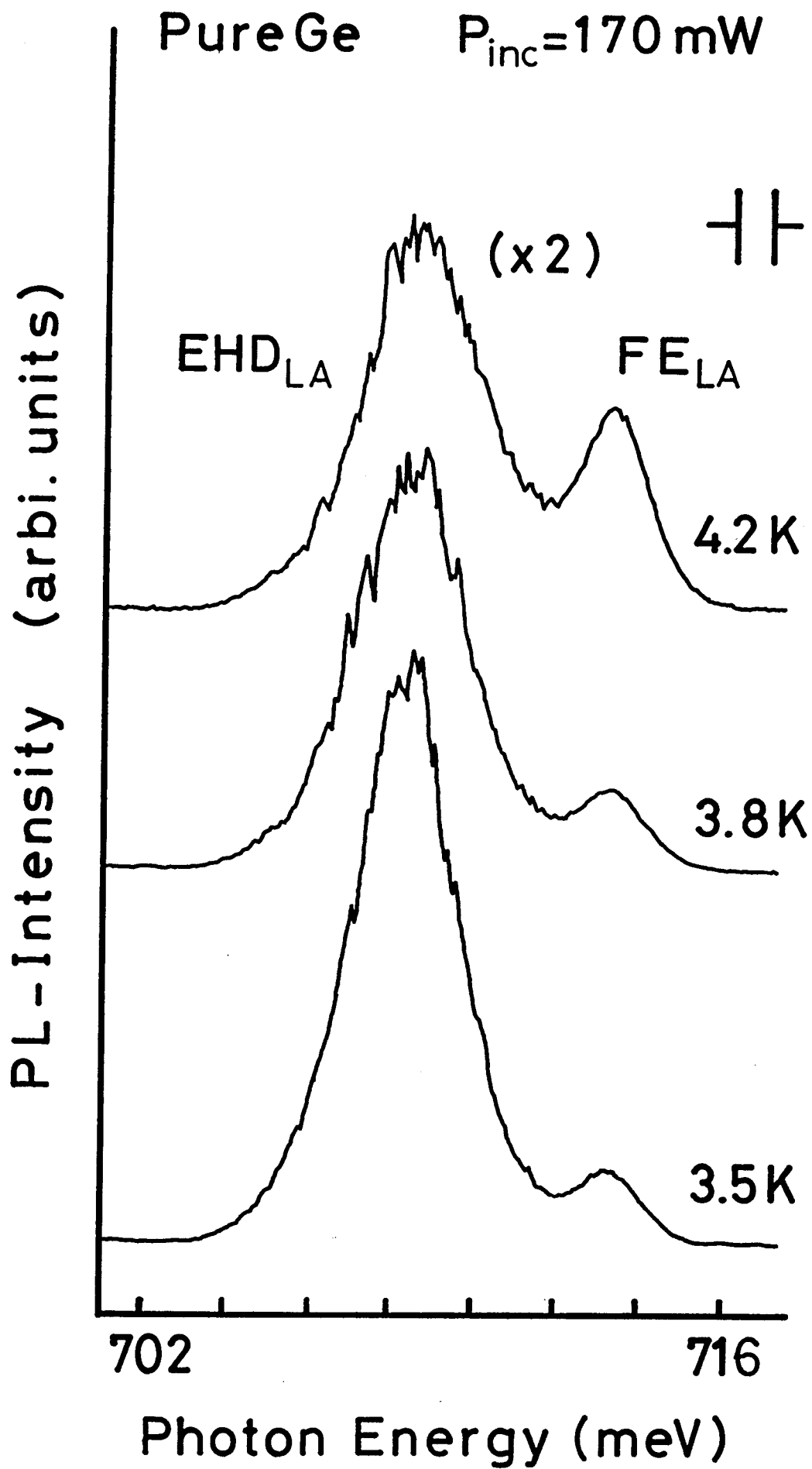


Fig. 21

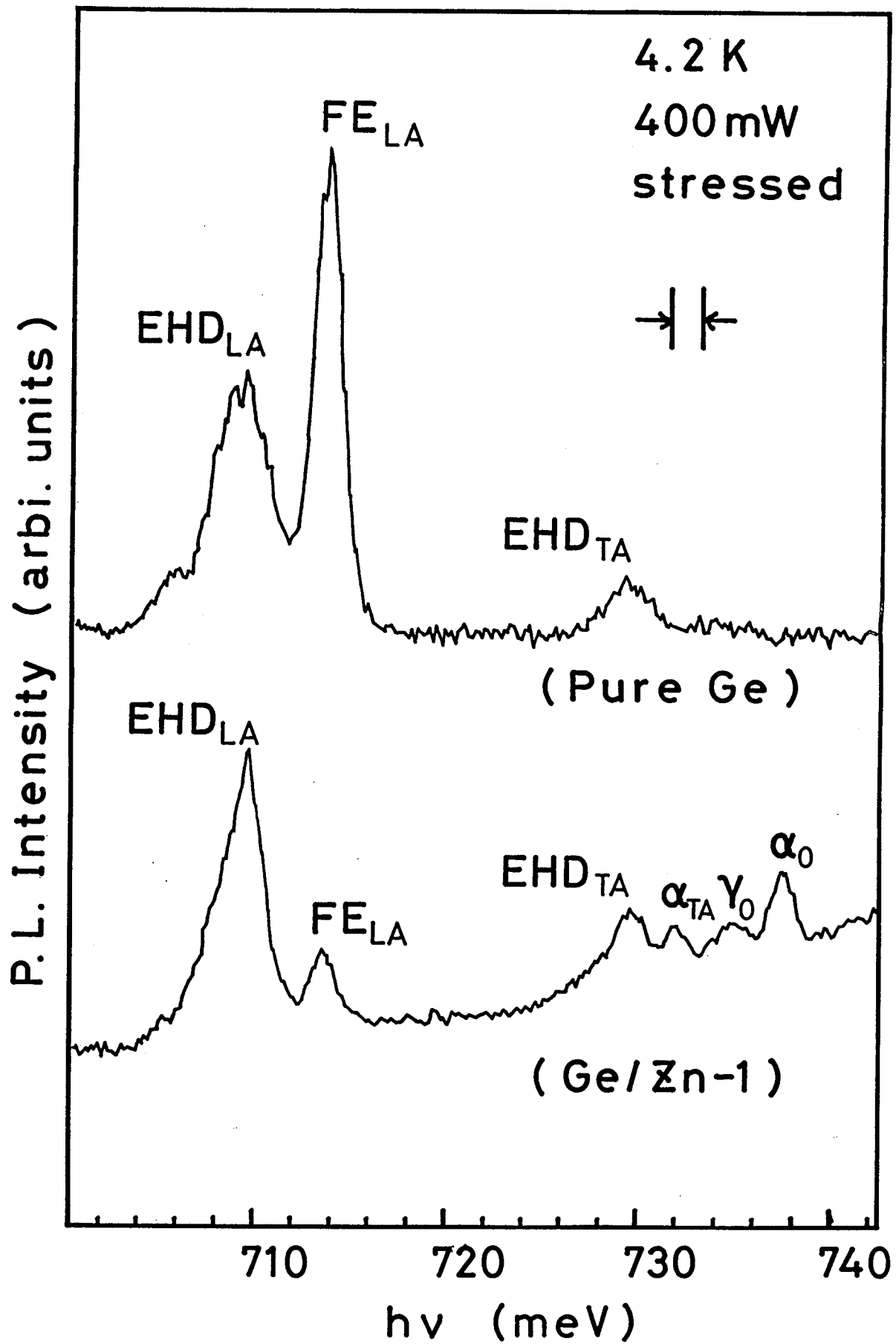


Fig. 22

1.7 K 400 mW

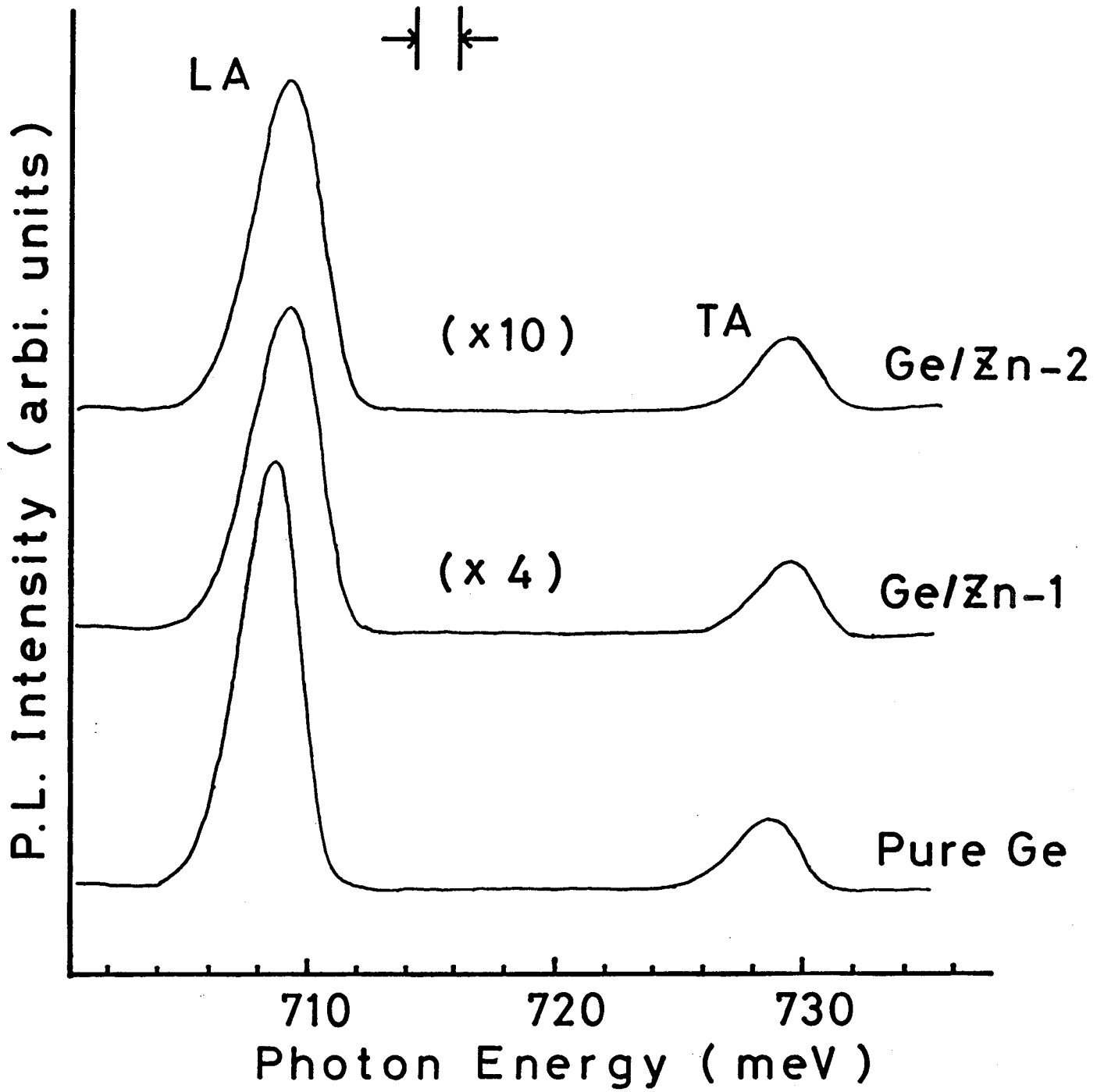


Fig. 23

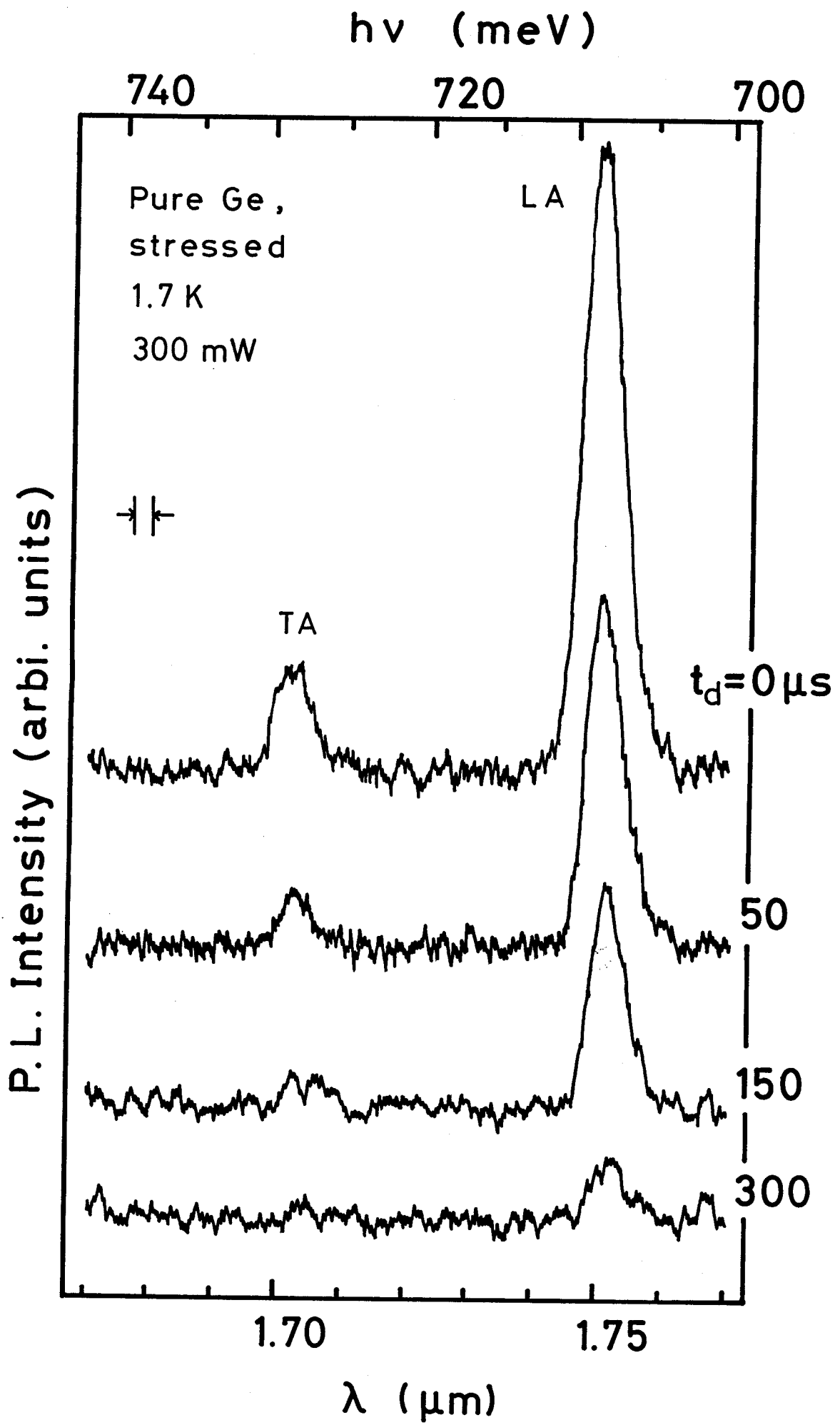


Fig. 24



1.7 K LA - Peak

- Pure Ge
- △ Ge/Zn-1
- Ge/Zn-2

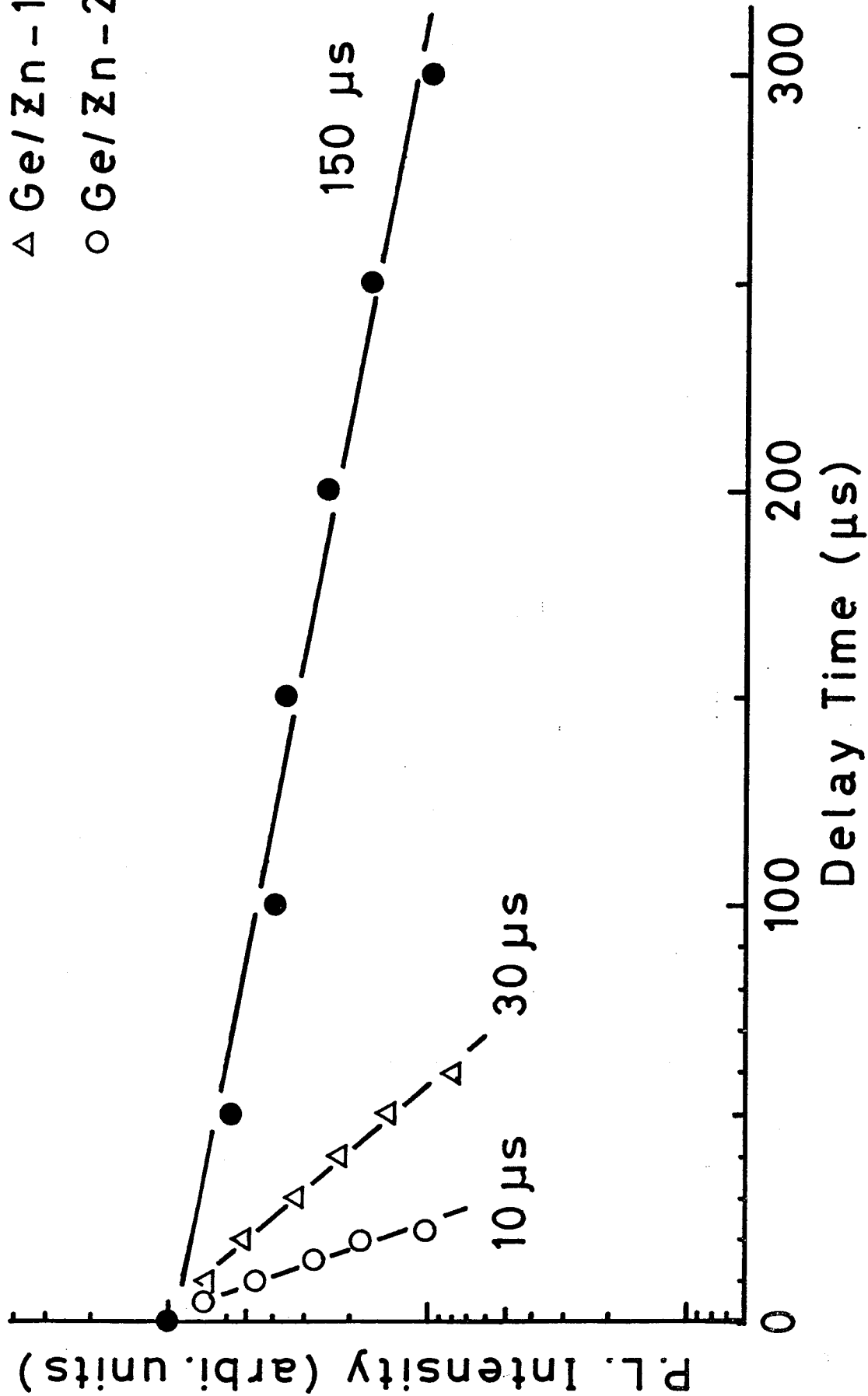


Fig. 26

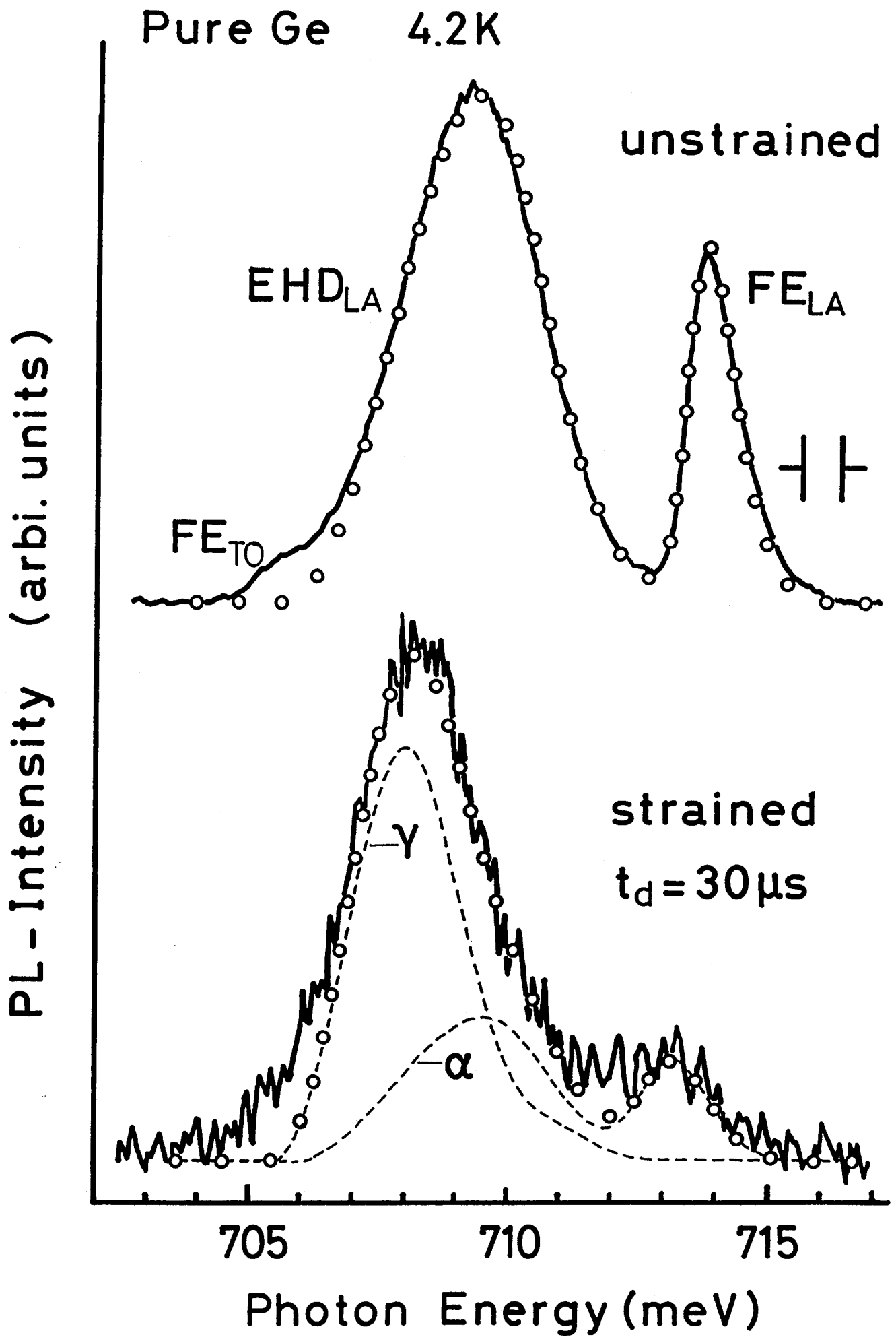


Fig. 27

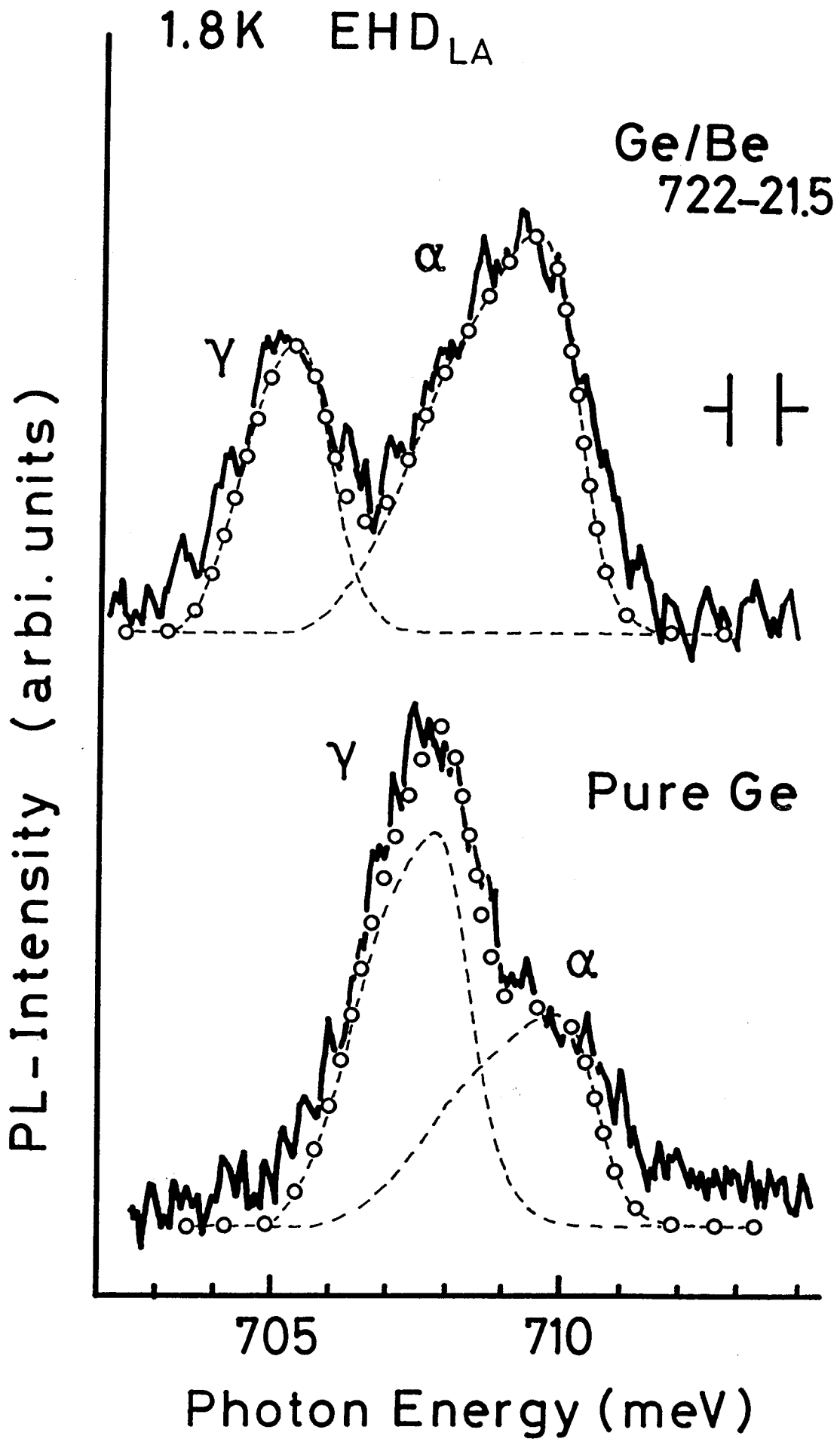


Fig. 28

Pure Ge 1.8 K

$P_{\text{abs}} = 33 \text{ mW}$

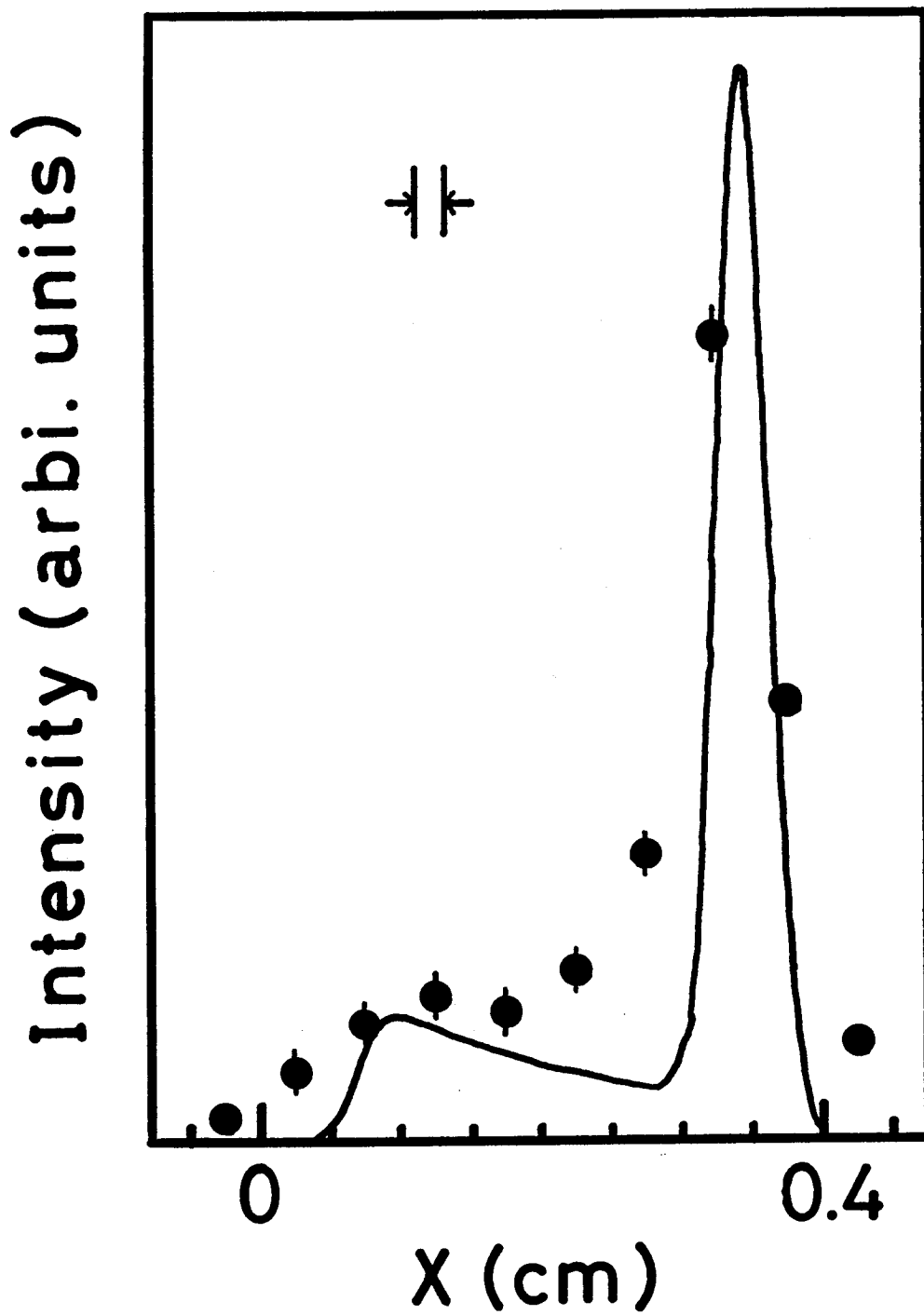


Fig. 29

Pure Ge

1.8 K

$P_{\text{abs}} = 67 \text{ mW}$

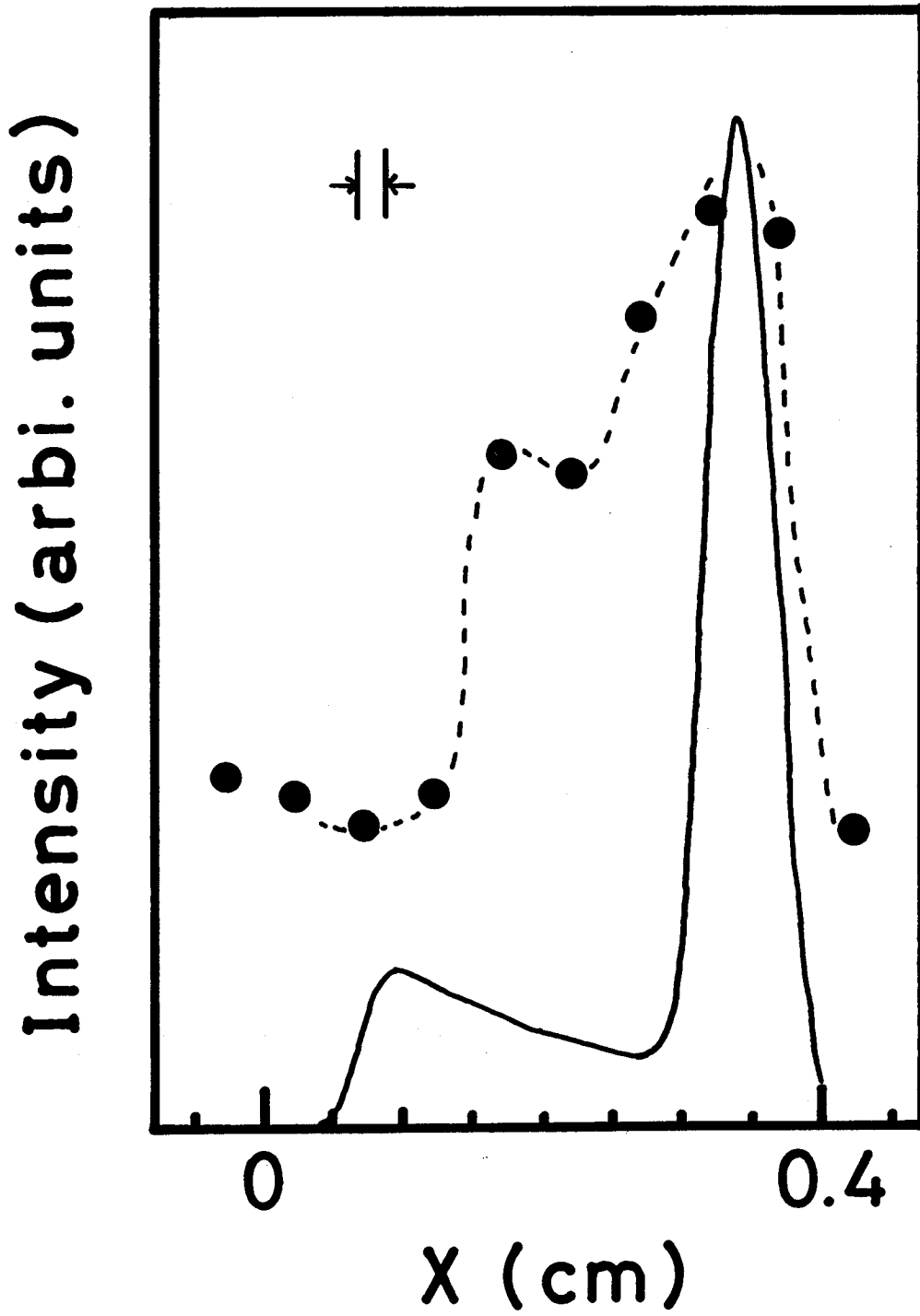


Fig. 30

Ge/Zn-1      1.8 K

$P_{\text{abs}} = 71 \text{ mW}$

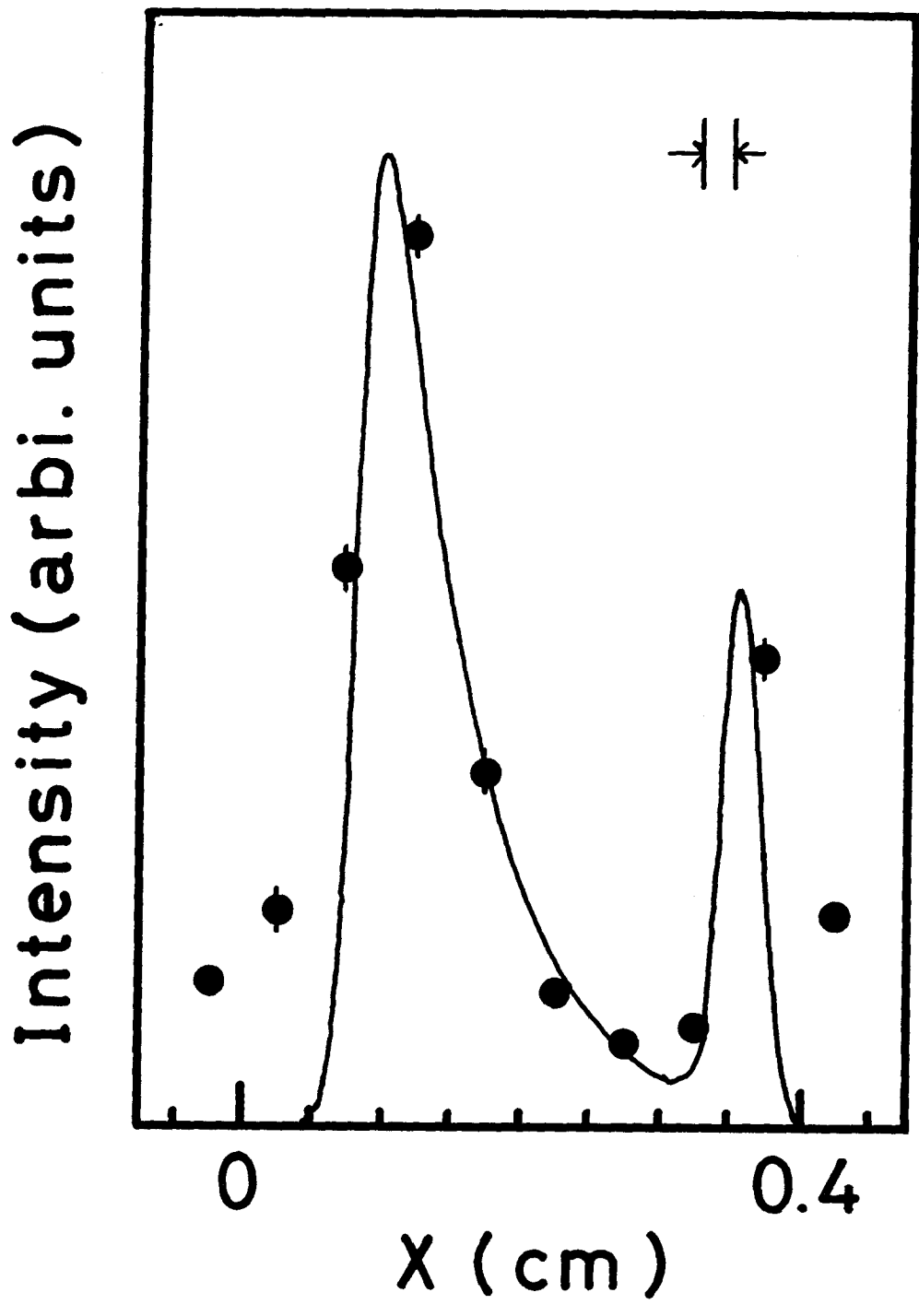


Fig. 31

Pure Ge 4.2 K

$P_{\text{abs}} = 63 \text{ mW}$

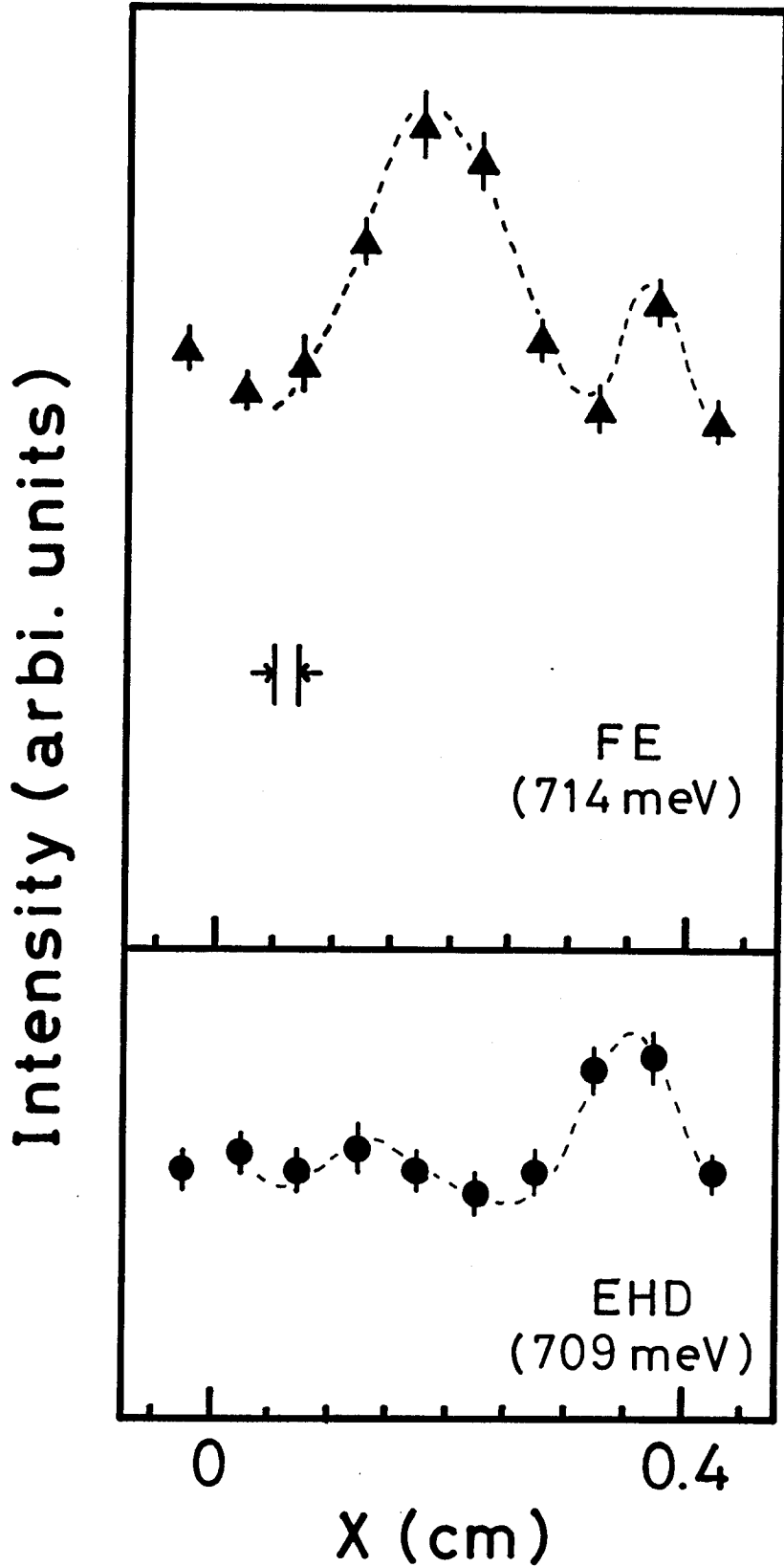


Fig. 32

Ge/Zn -1      4.2 K

$P_{\text{abs}} = 72 \text{ mW}$

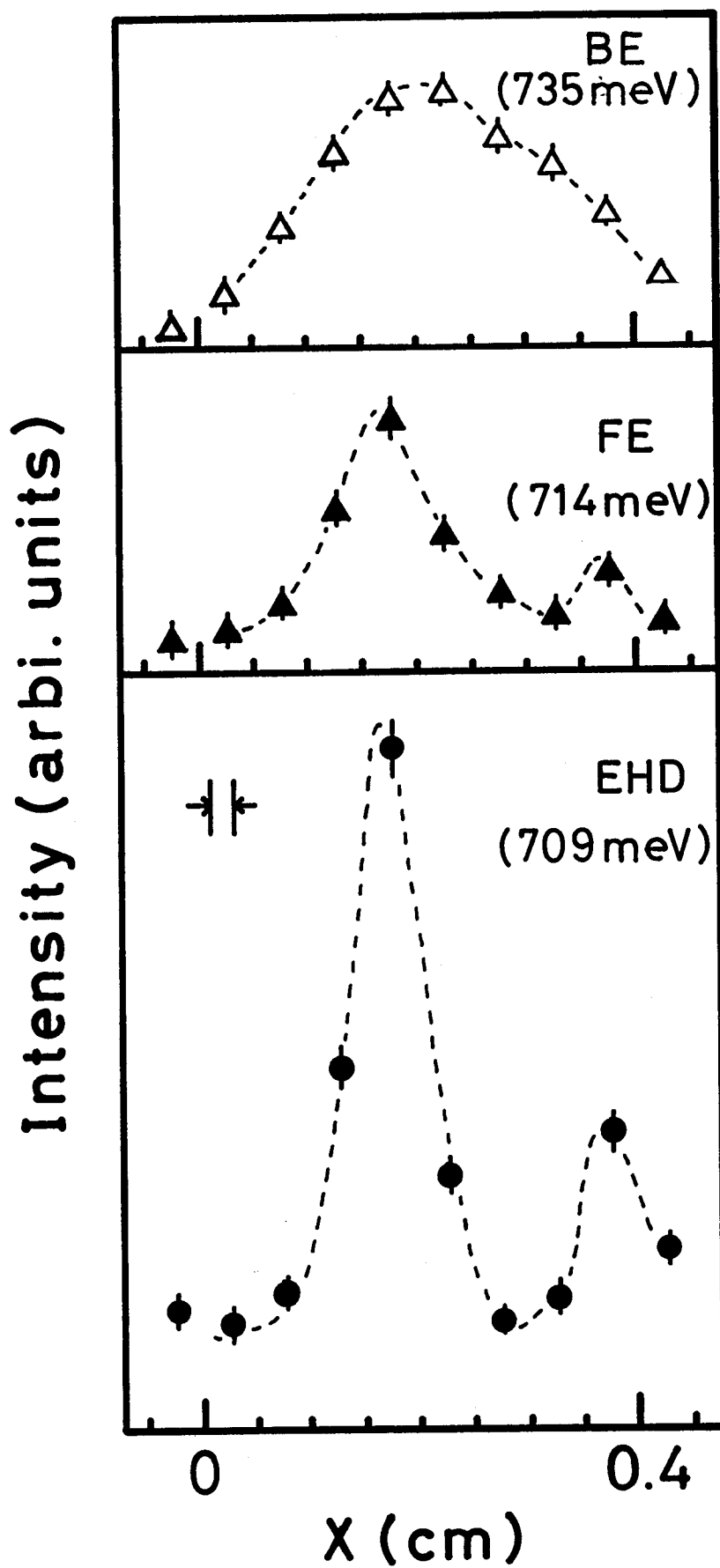


Fig. 33

Pure Ge

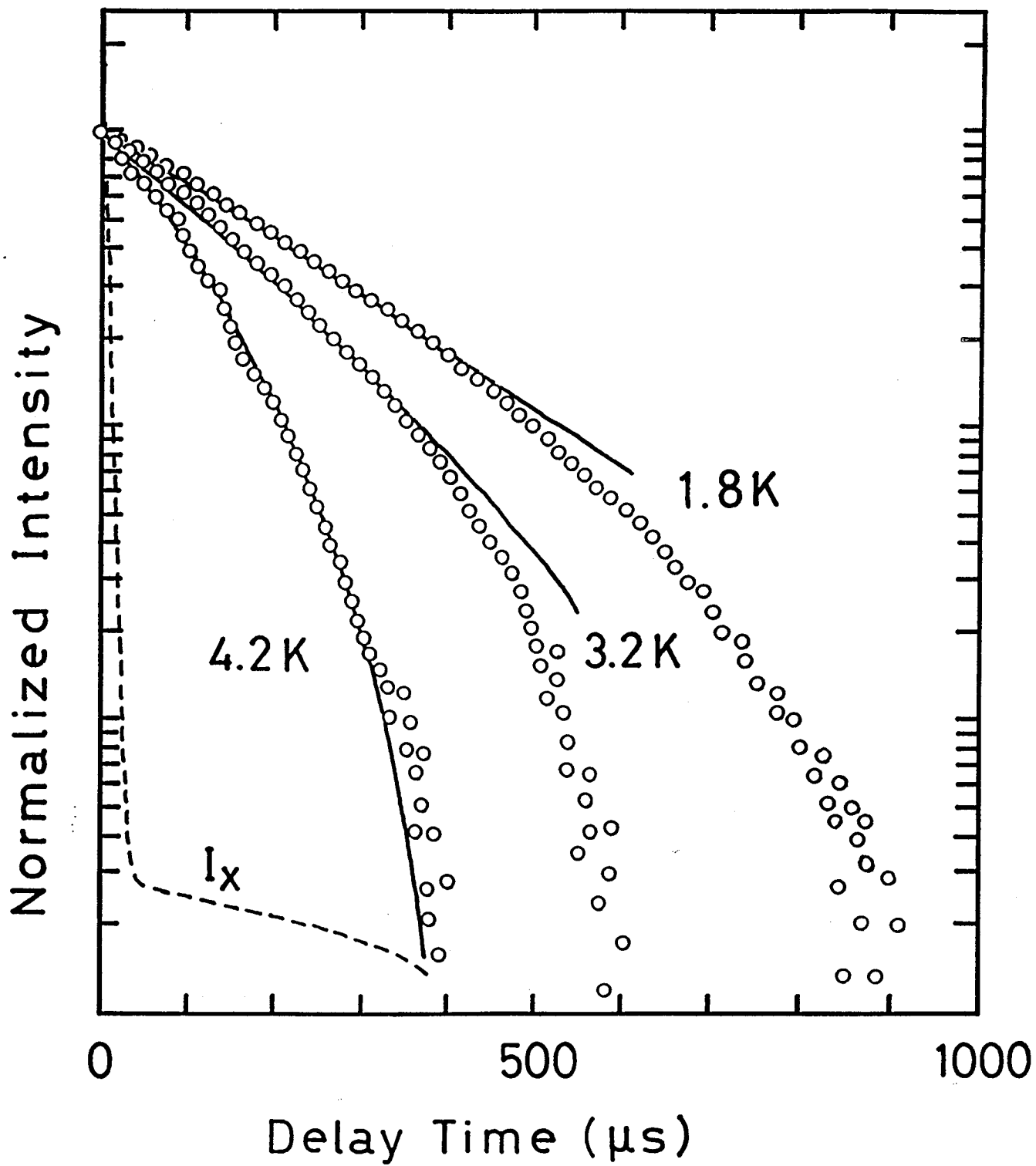


Fig. 34

Pure Ge

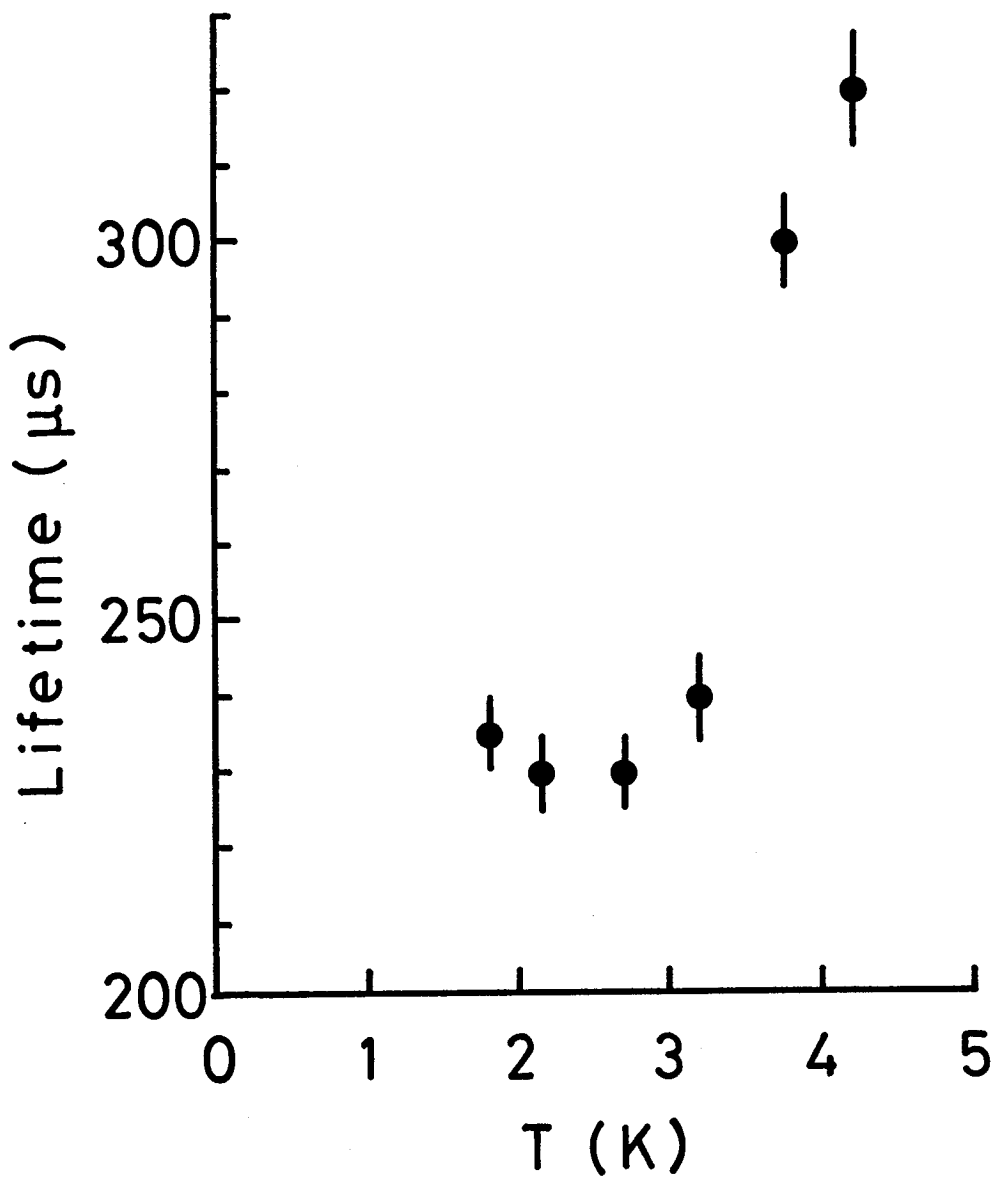


Fig. 35

Pure Ge

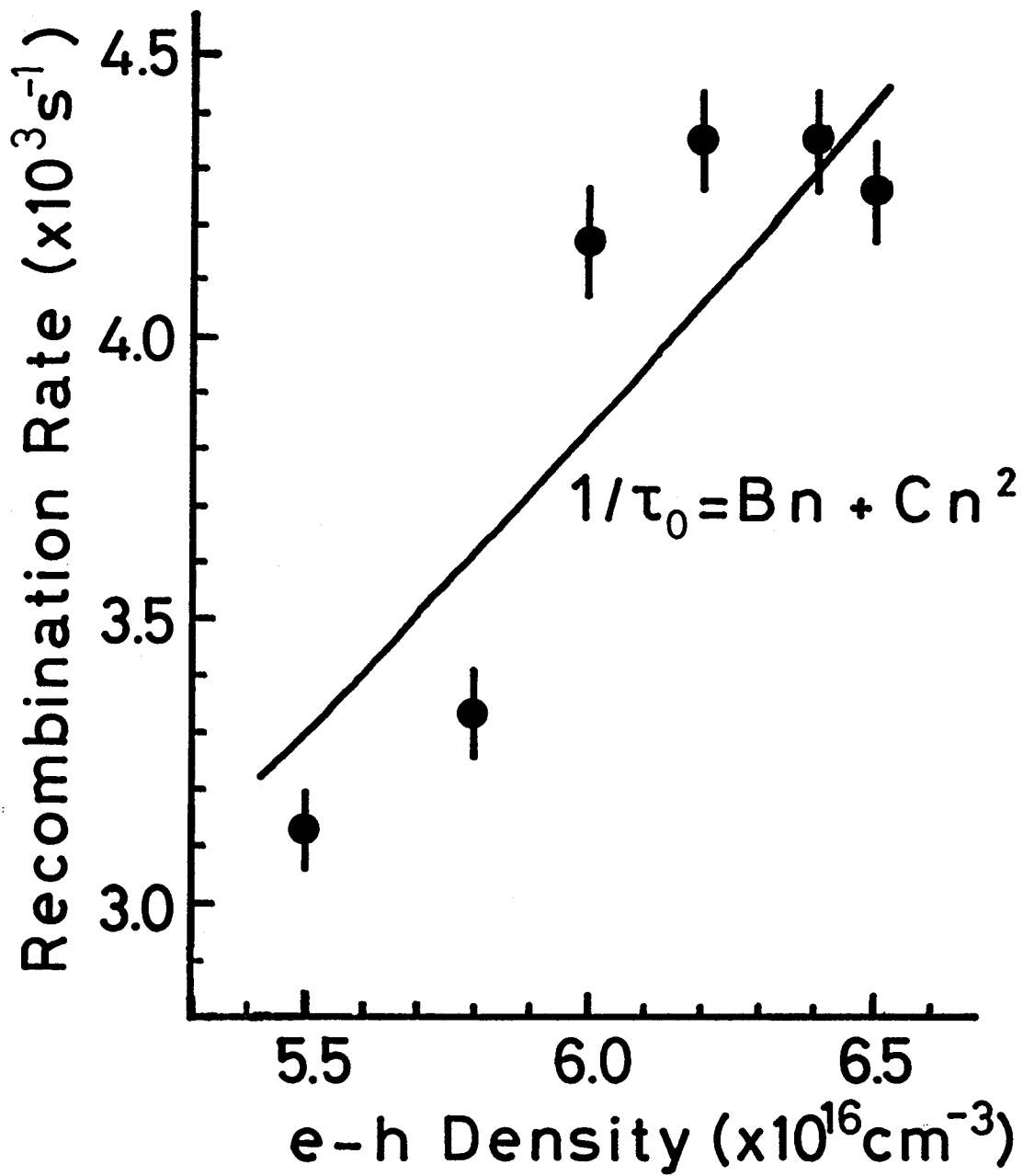


Fig. 36

4.2 K

$P_{inc} = 79 \text{ mW}$

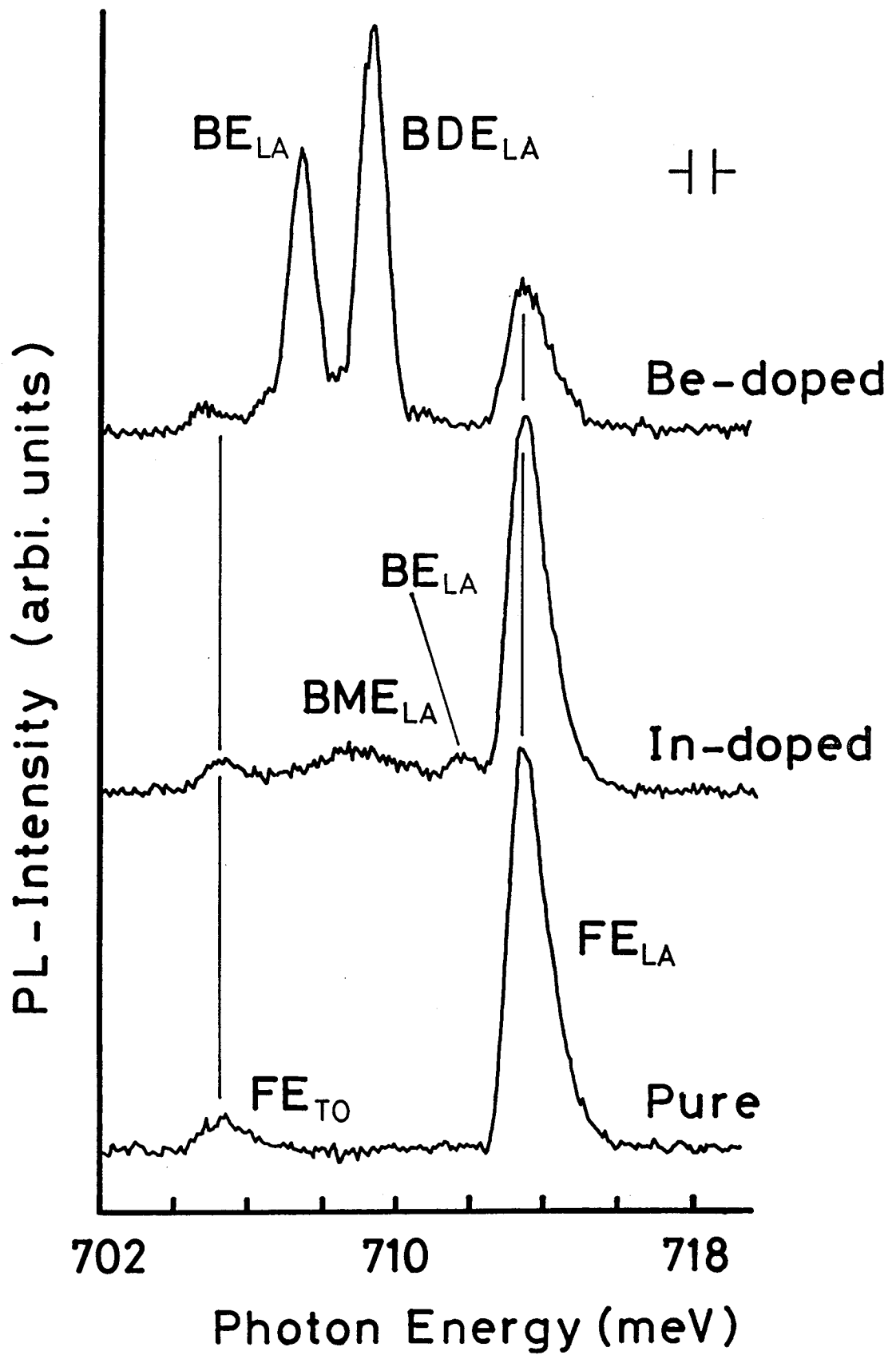


Fig. 37

Unstrained, 4.2 K

$I_{\text{EHDLA}}$  (arbi. units)

$P^{\text{th}}$  ↓

0 100 200

Incident Power (mW)

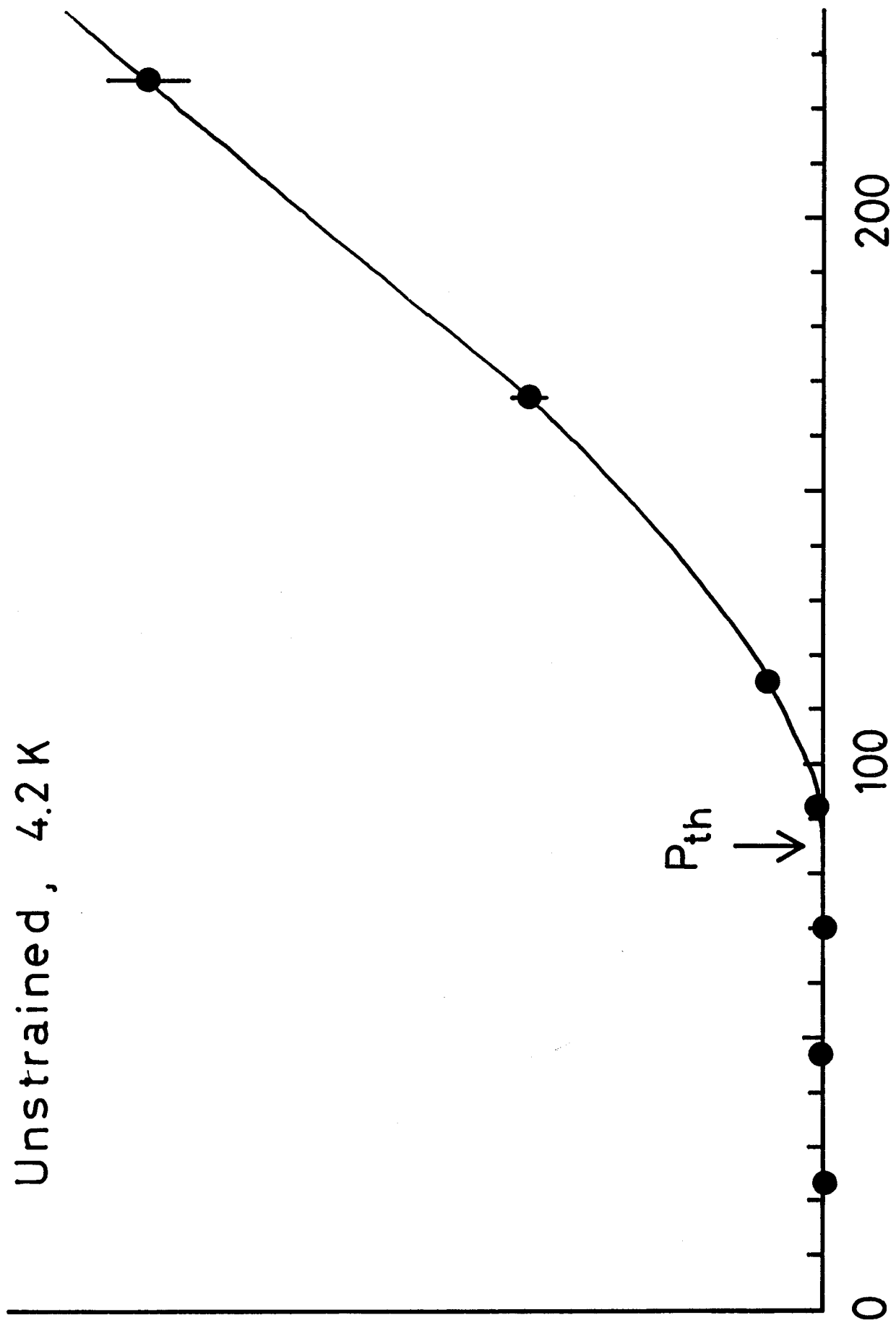


Fig. 38

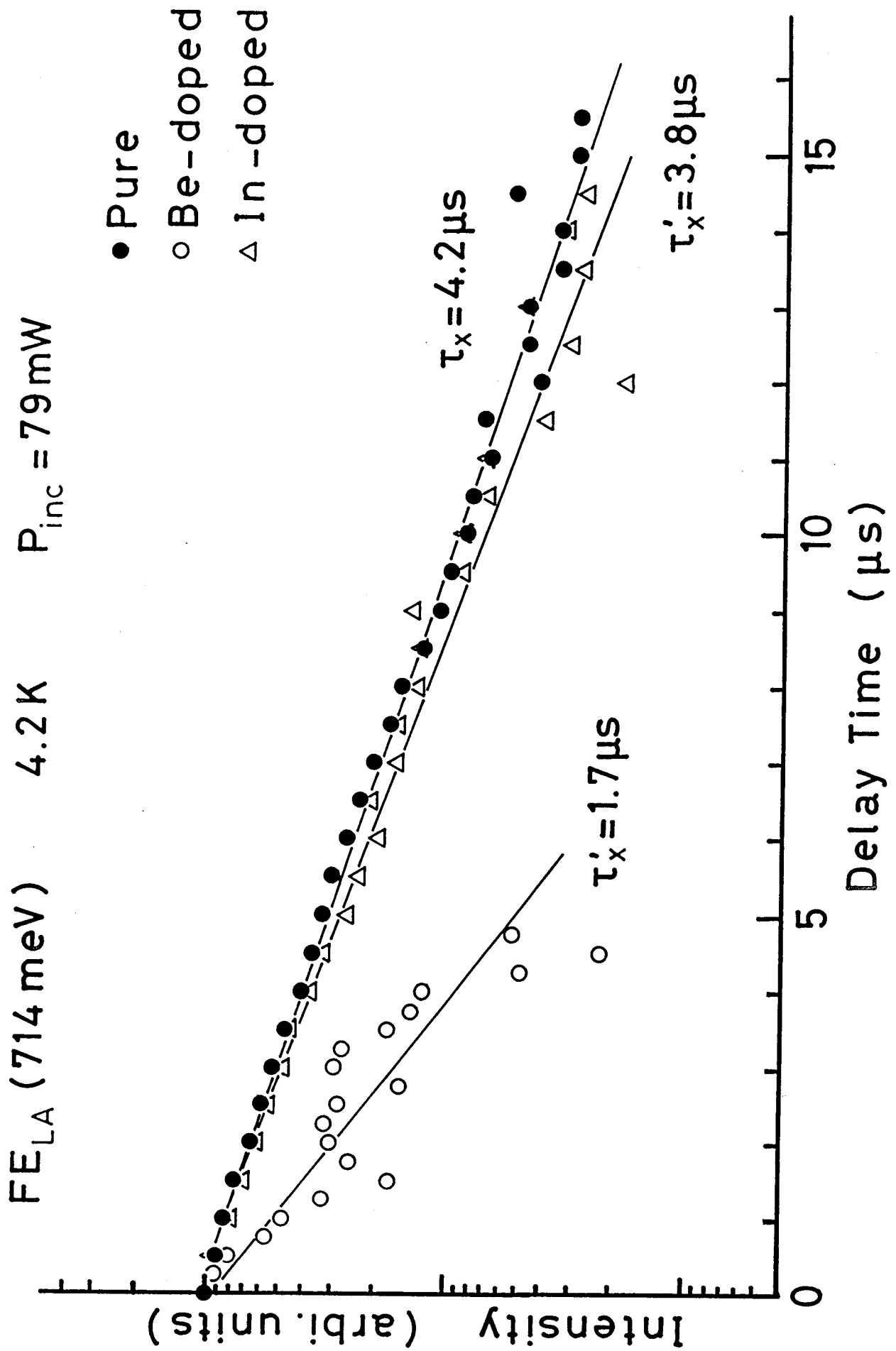


Fig. 39

In-doped,  $6.0 \times 10^{13} \text{ cm}^{-3}$

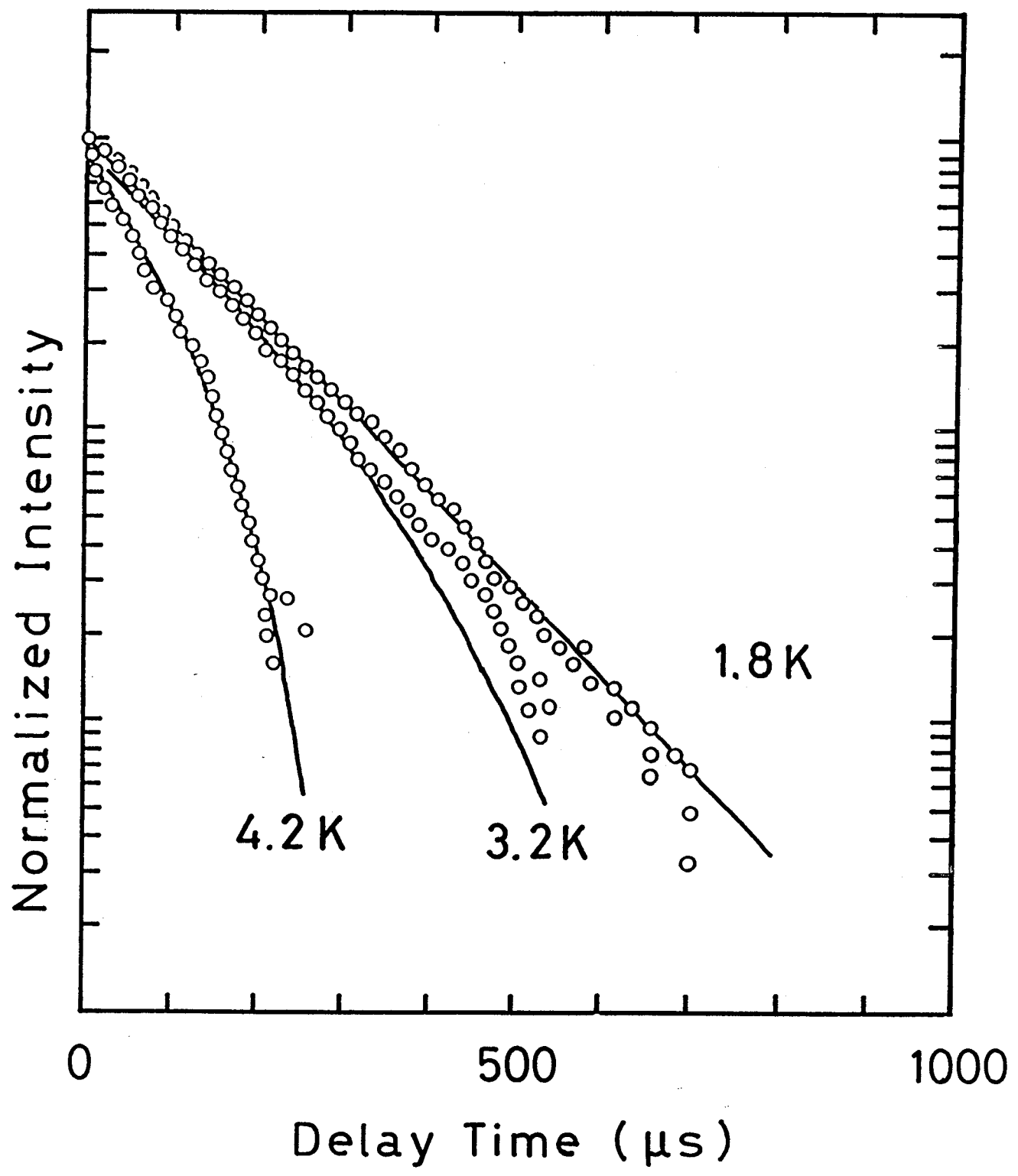


Fig. 40

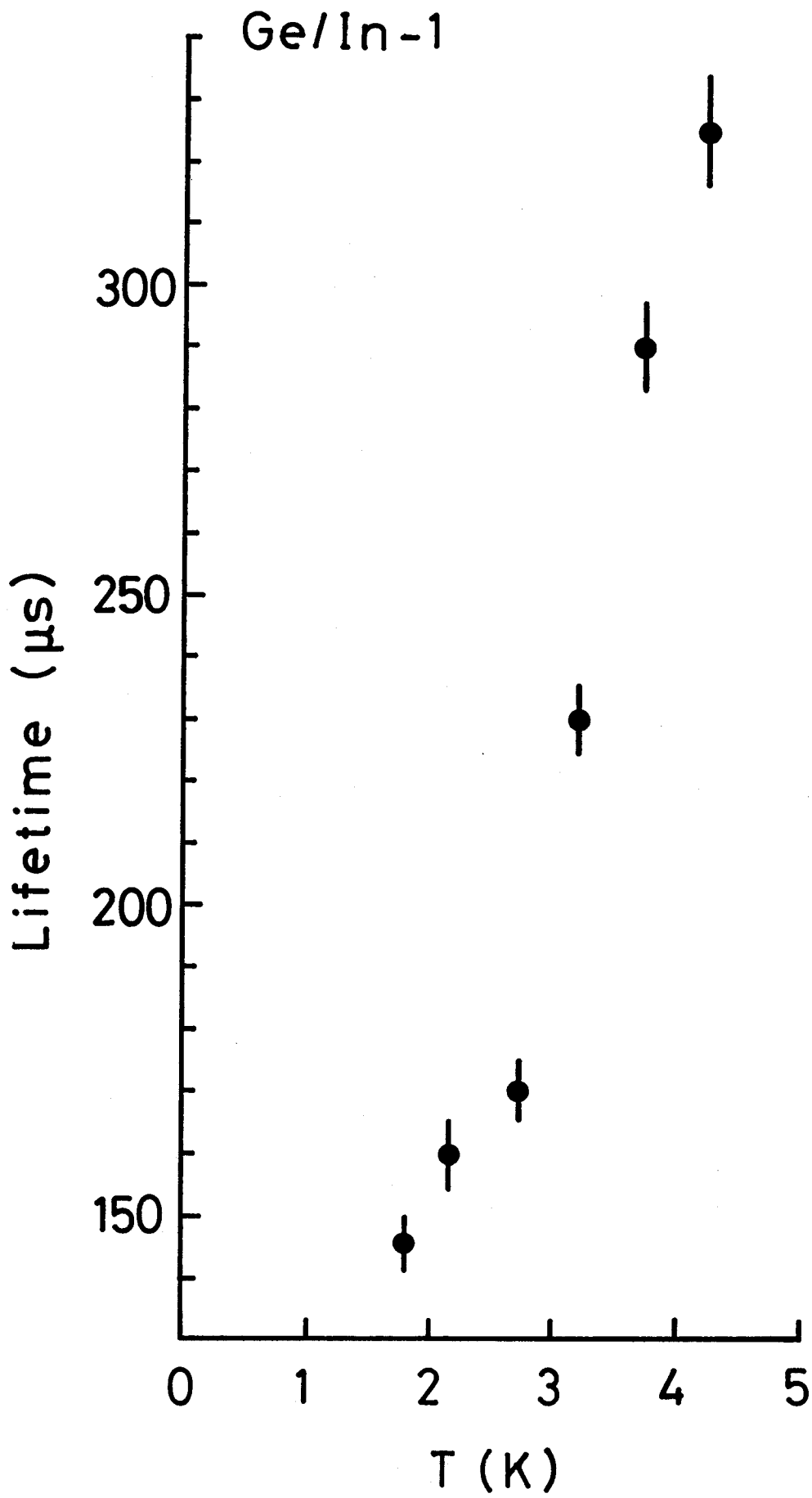


Fig. 41

In-doped,  $3.7 \times 10^{14} \text{ cm}^{-3}$

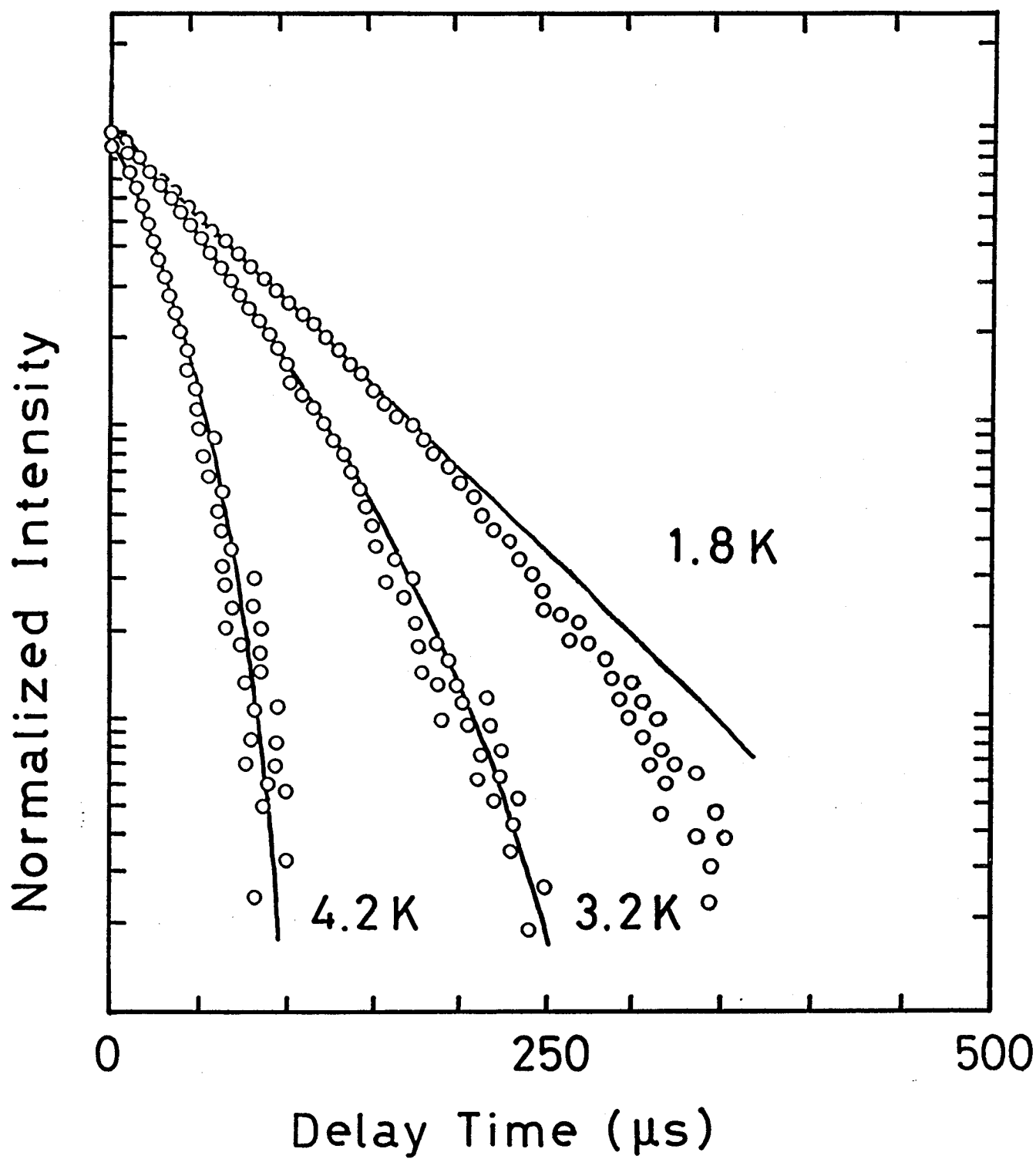


Fig. 42

Ge/In-2

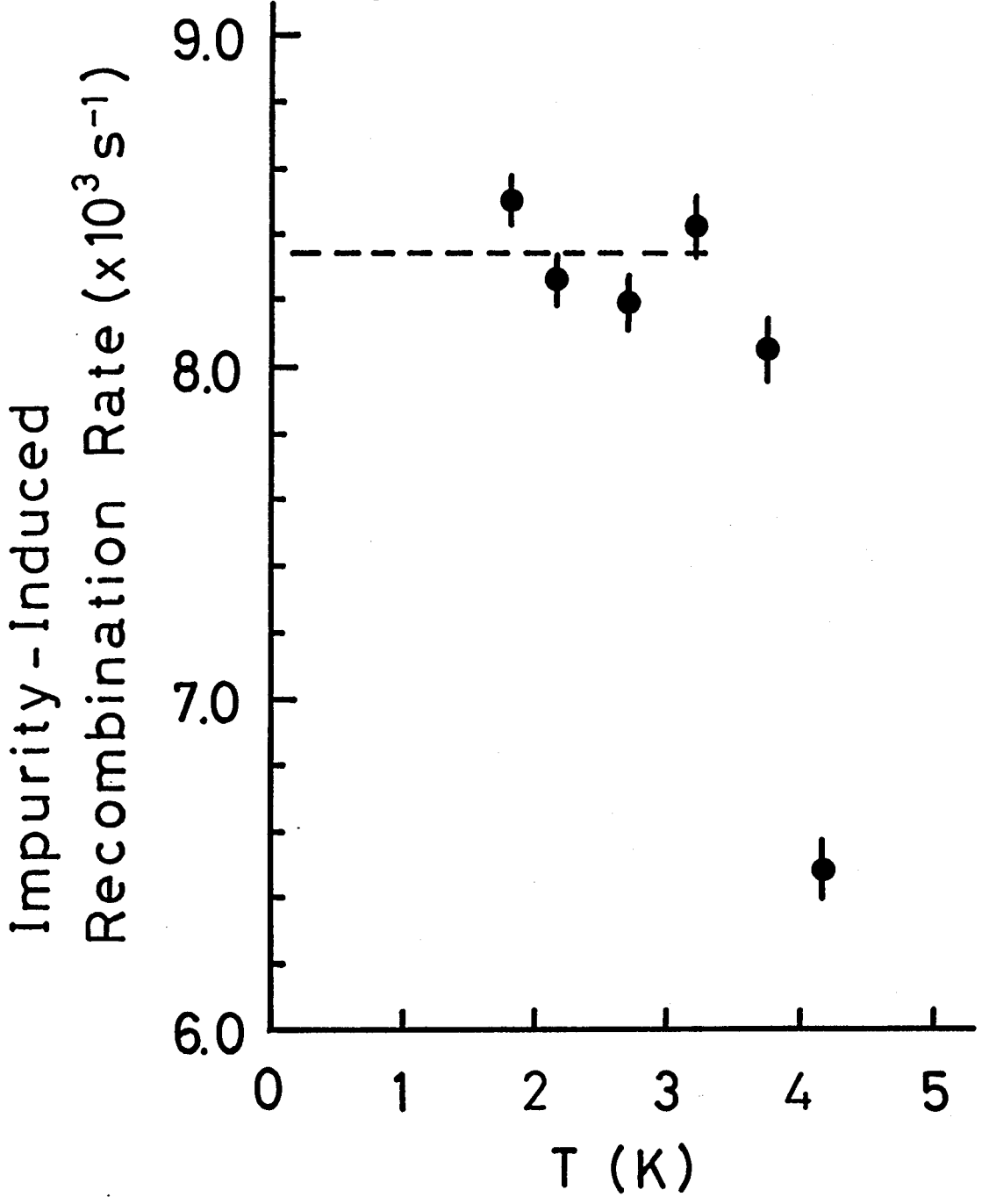


Fig. 43

In-doped,  $1.8 \times 10^{15} \text{ cm}^{-3}$

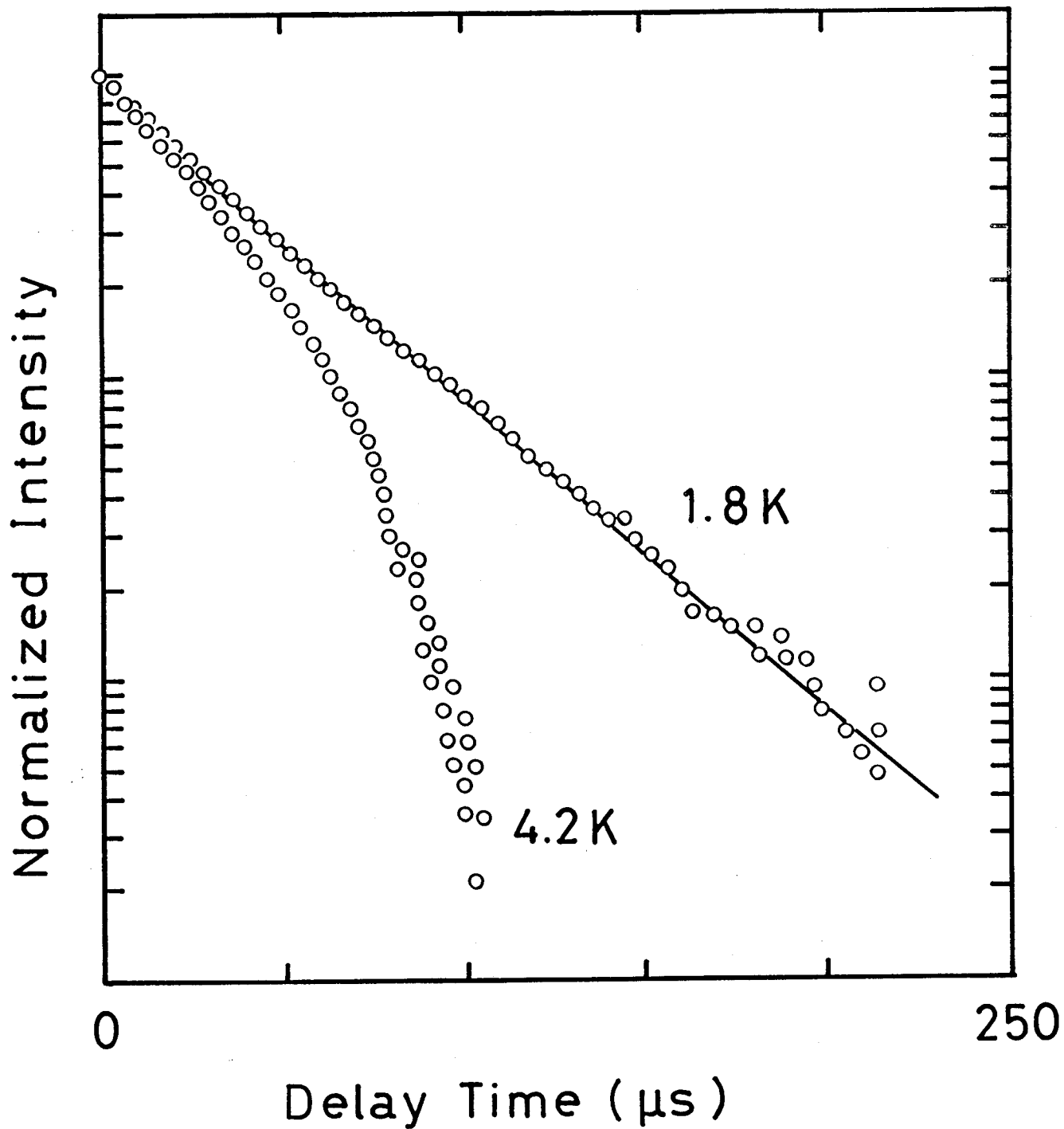


Fig. 44

Be-doped,  $4.5 \times 10^{13} \text{ cm}^{-3}$

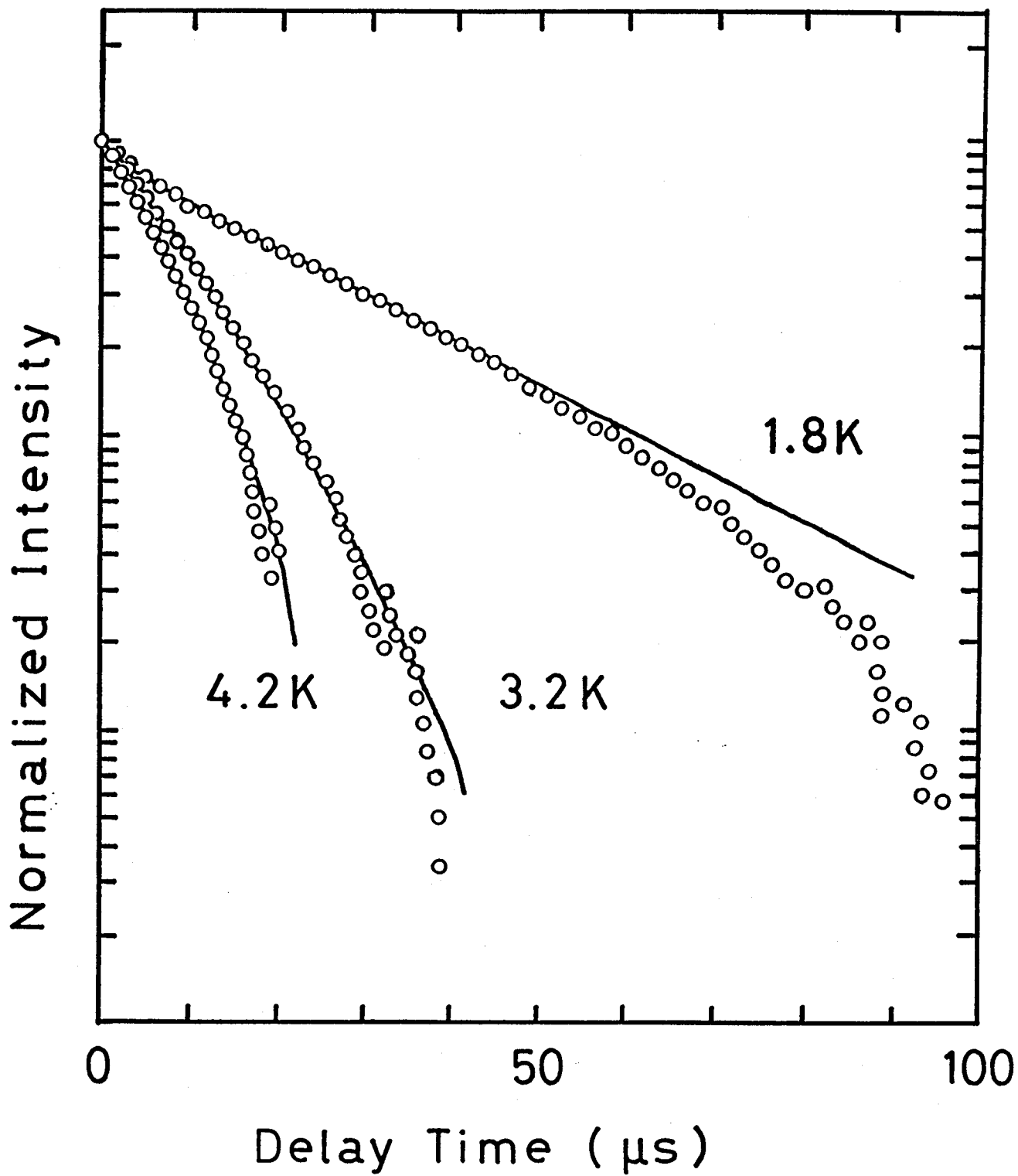


Fig. 45

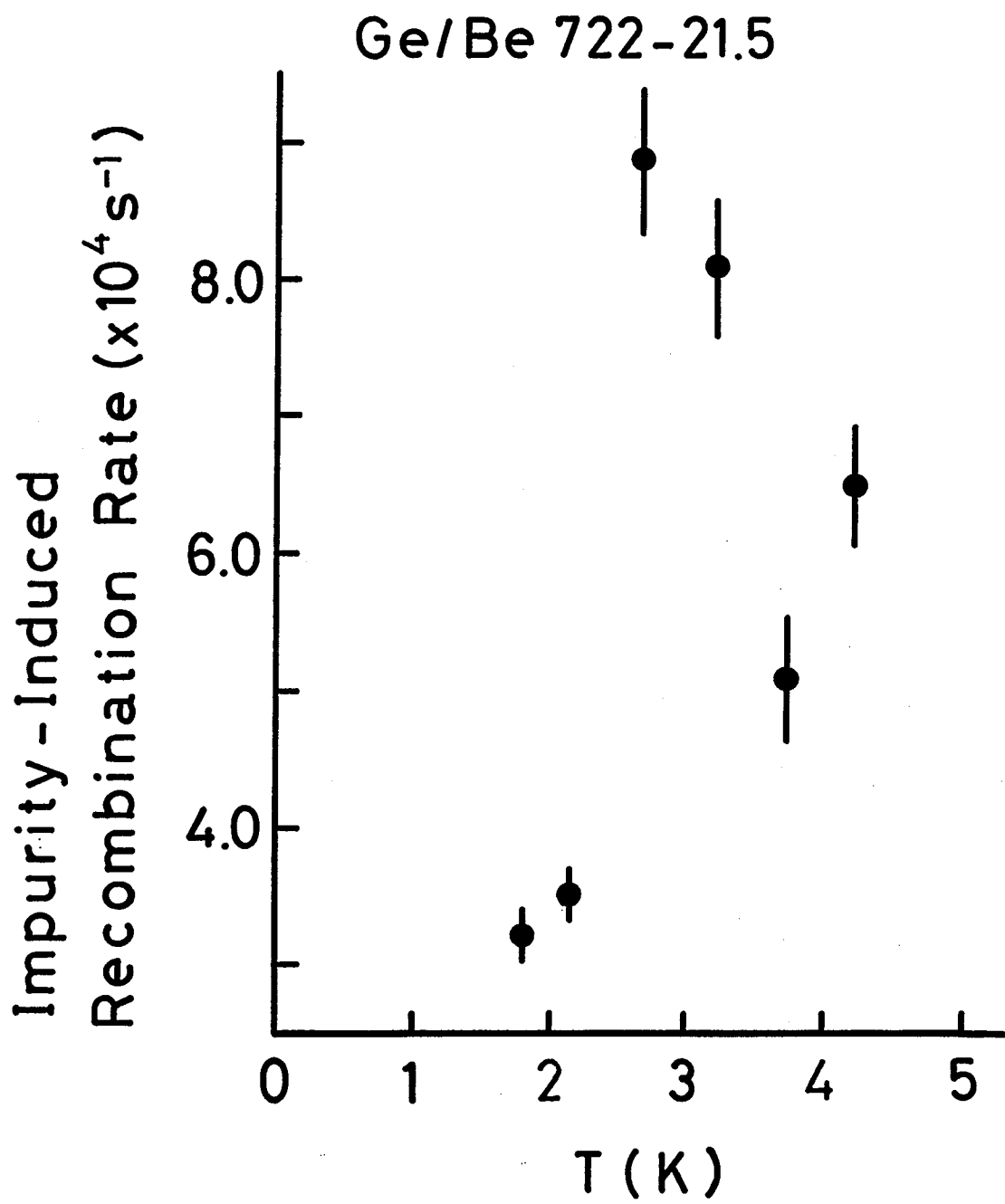


Fig. 46

Be-doped,  $1.0 \times 10^{15} \text{ cm}^{-3}$

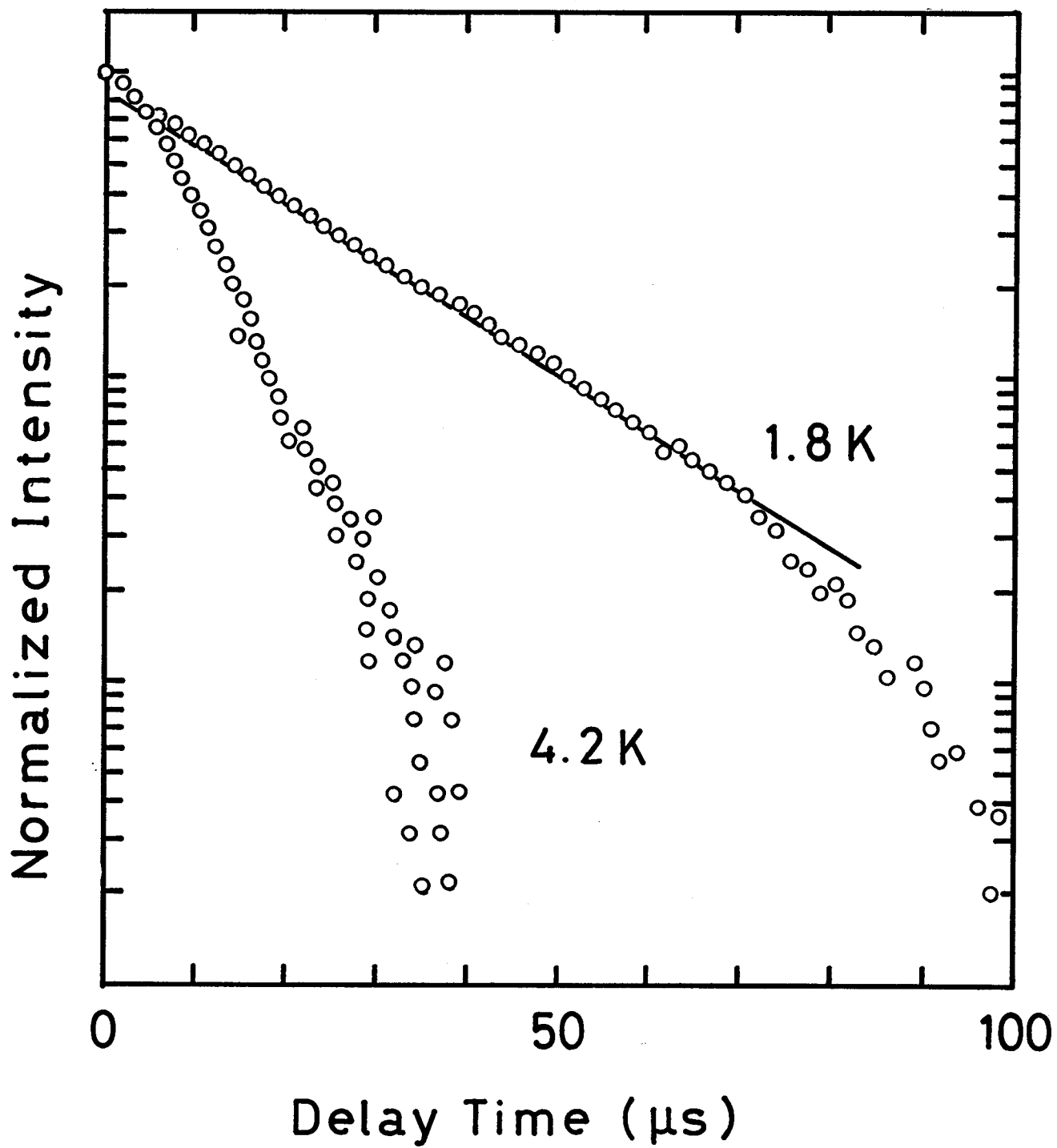


Fig. 47

Be-doped,  $2.0 \times 10^{15} \text{ cm}^{-3}$

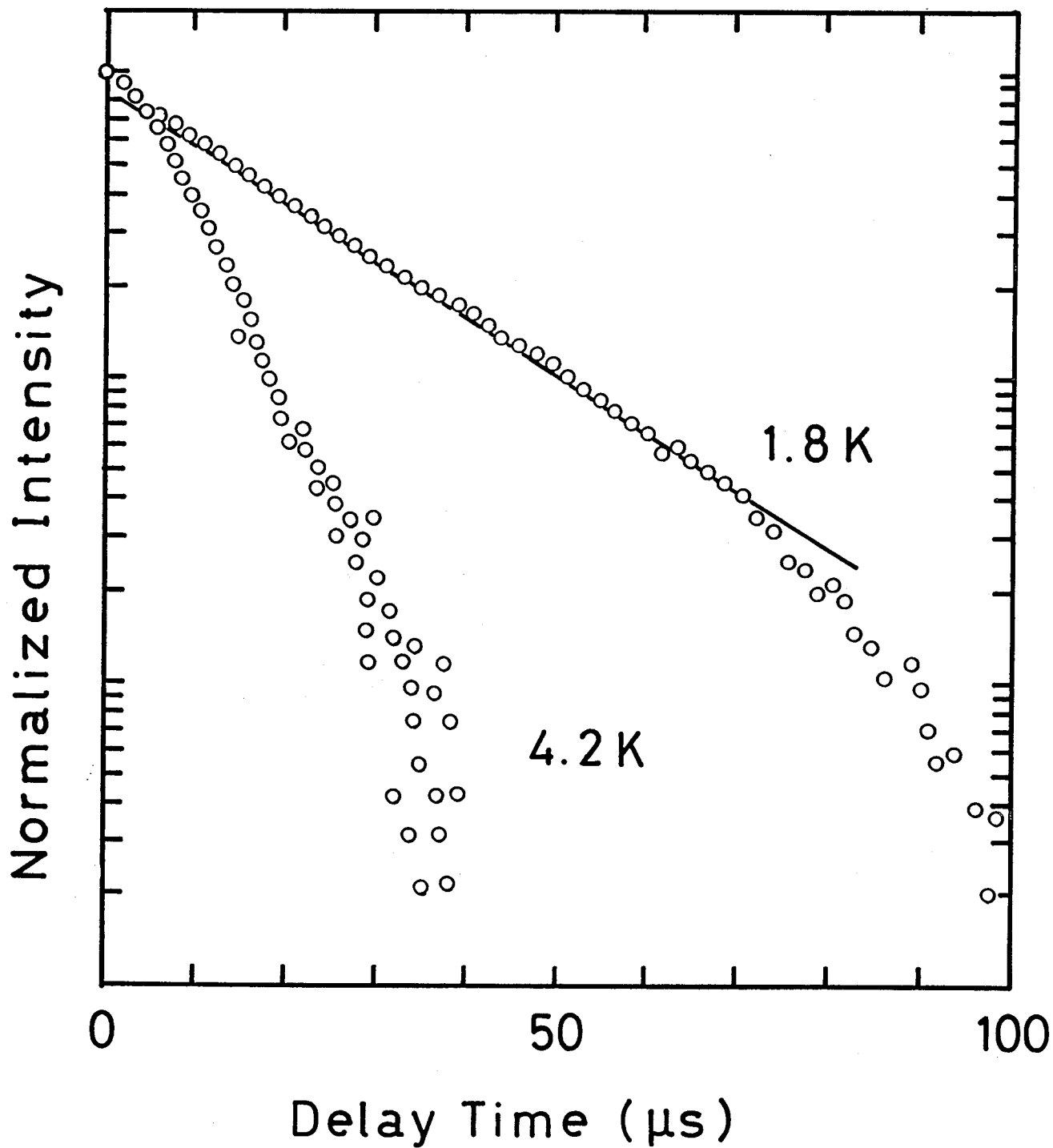


Fig. 47

Zn-doped,  $1.2 \times 10^{14} \text{ cm}^{-3}$

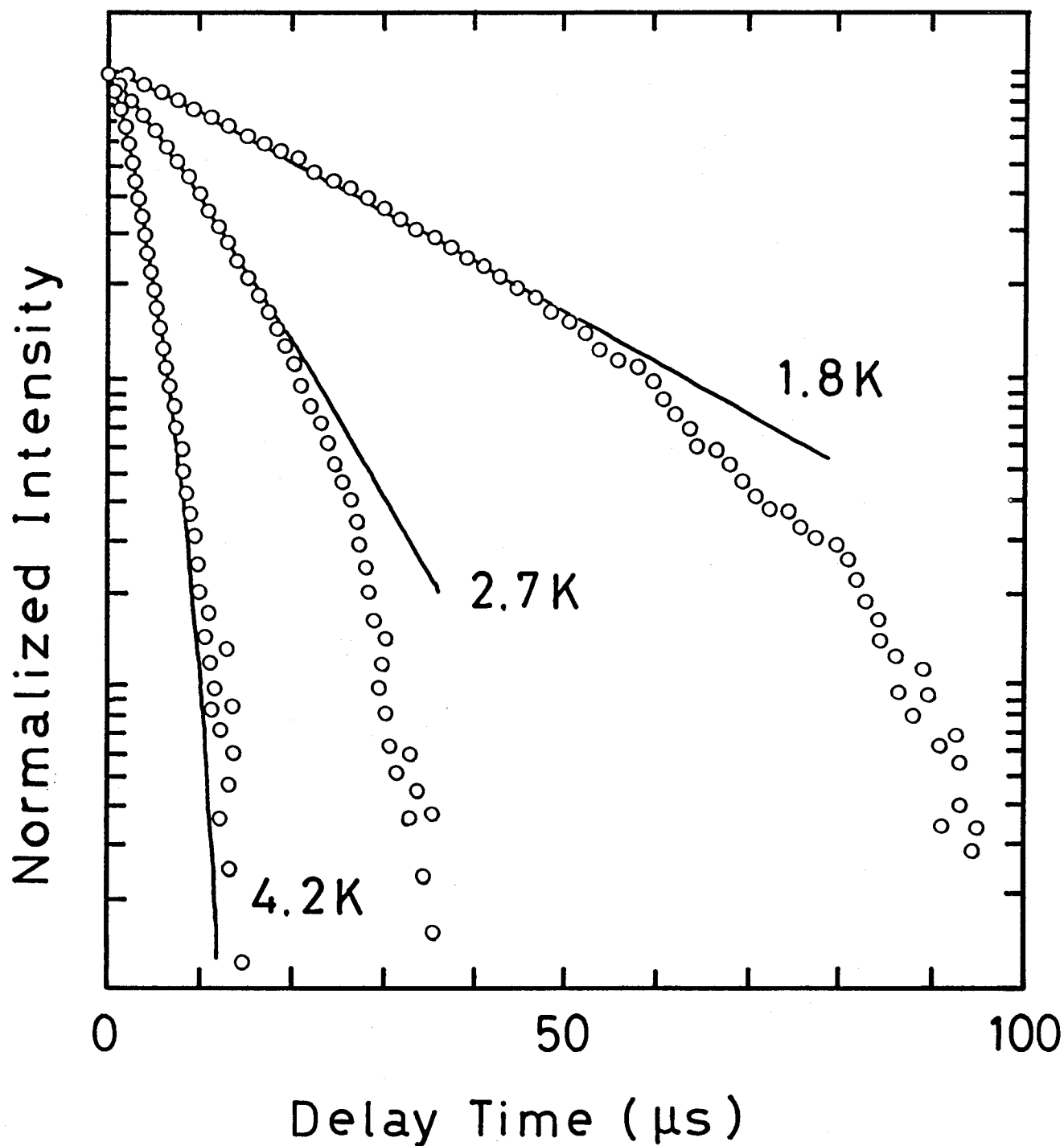


Fig. 48

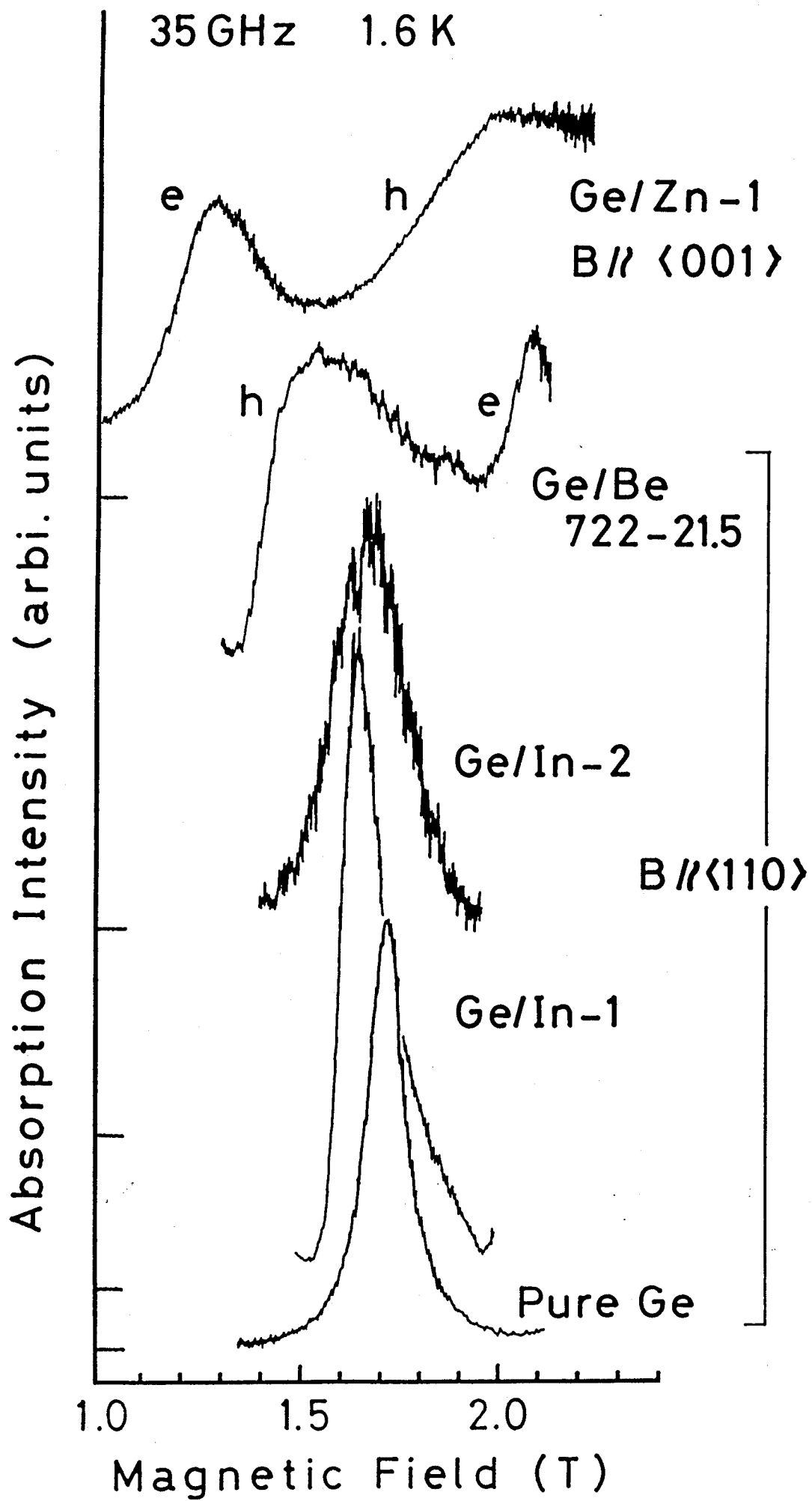


Fig. 49

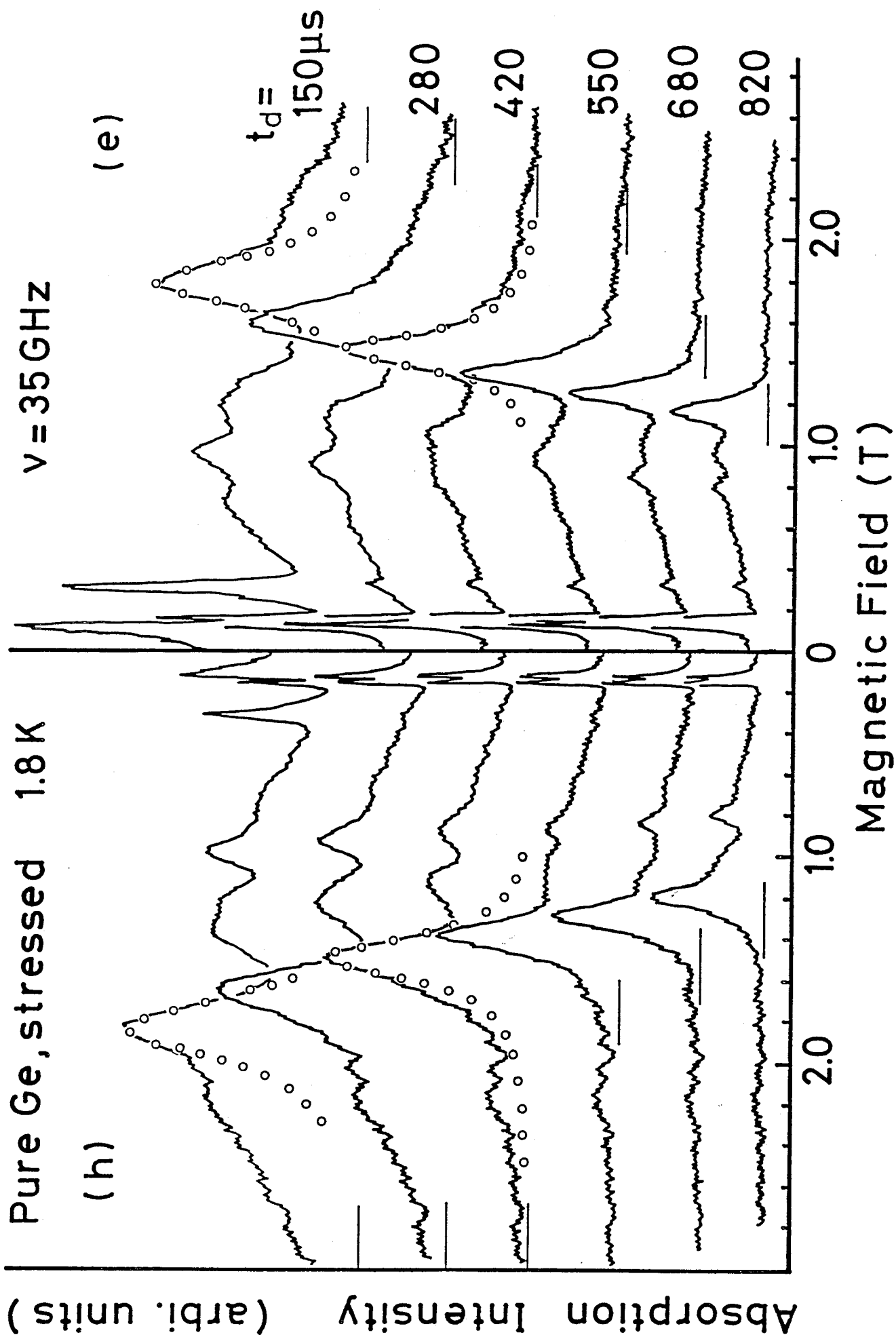


Fig. 50

Ge/Zn-1

1.6 K

35 GHz

Absorption Intensity (arbi. units)

$t_d = 30 \mu s$

h

50  $\mu s$

e

70  $\mu s$

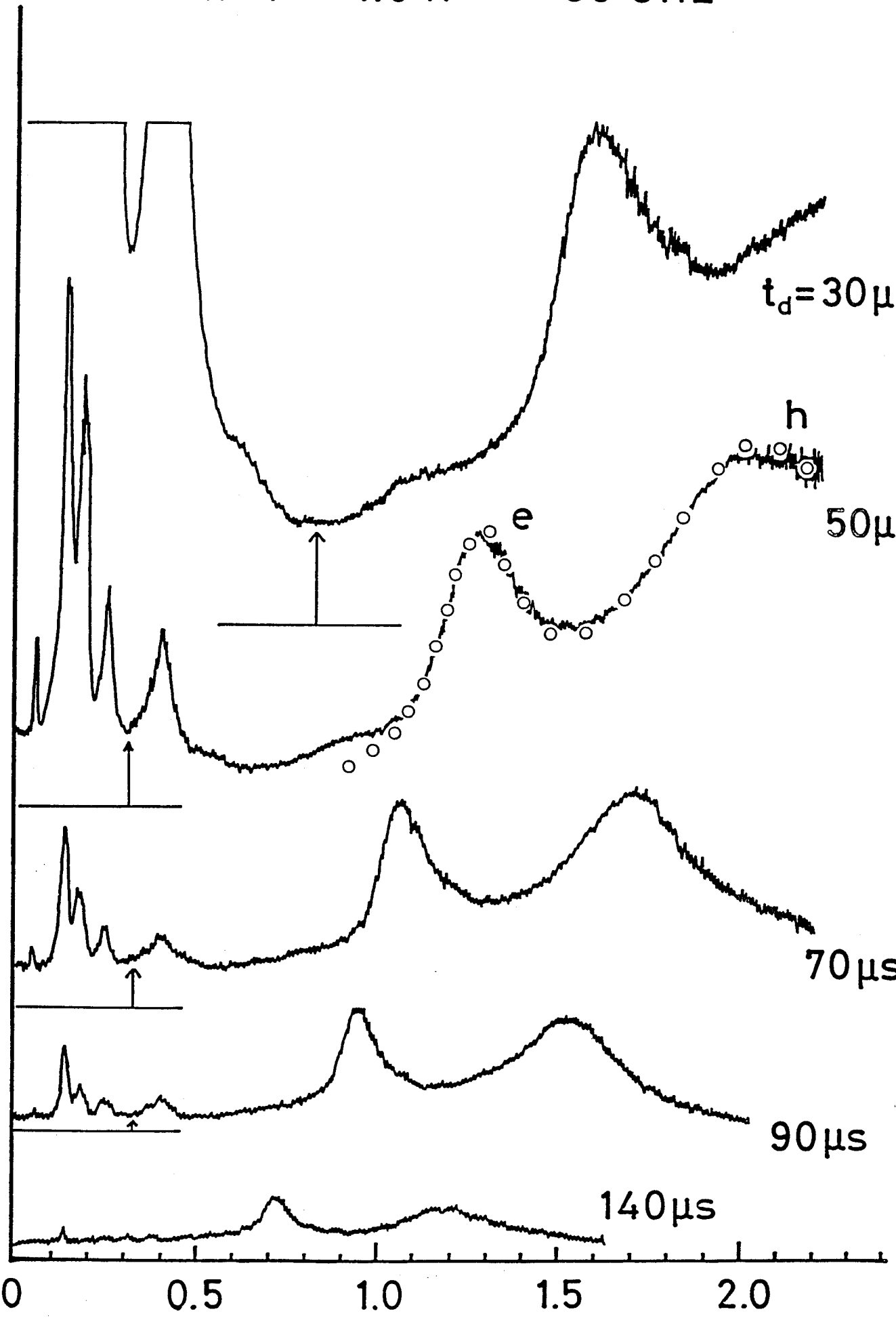
90  $\mu s$

140  $\mu s$

0 0.5 1.0 1.5 2.0

Magnetic Field (T)

Fig. 51



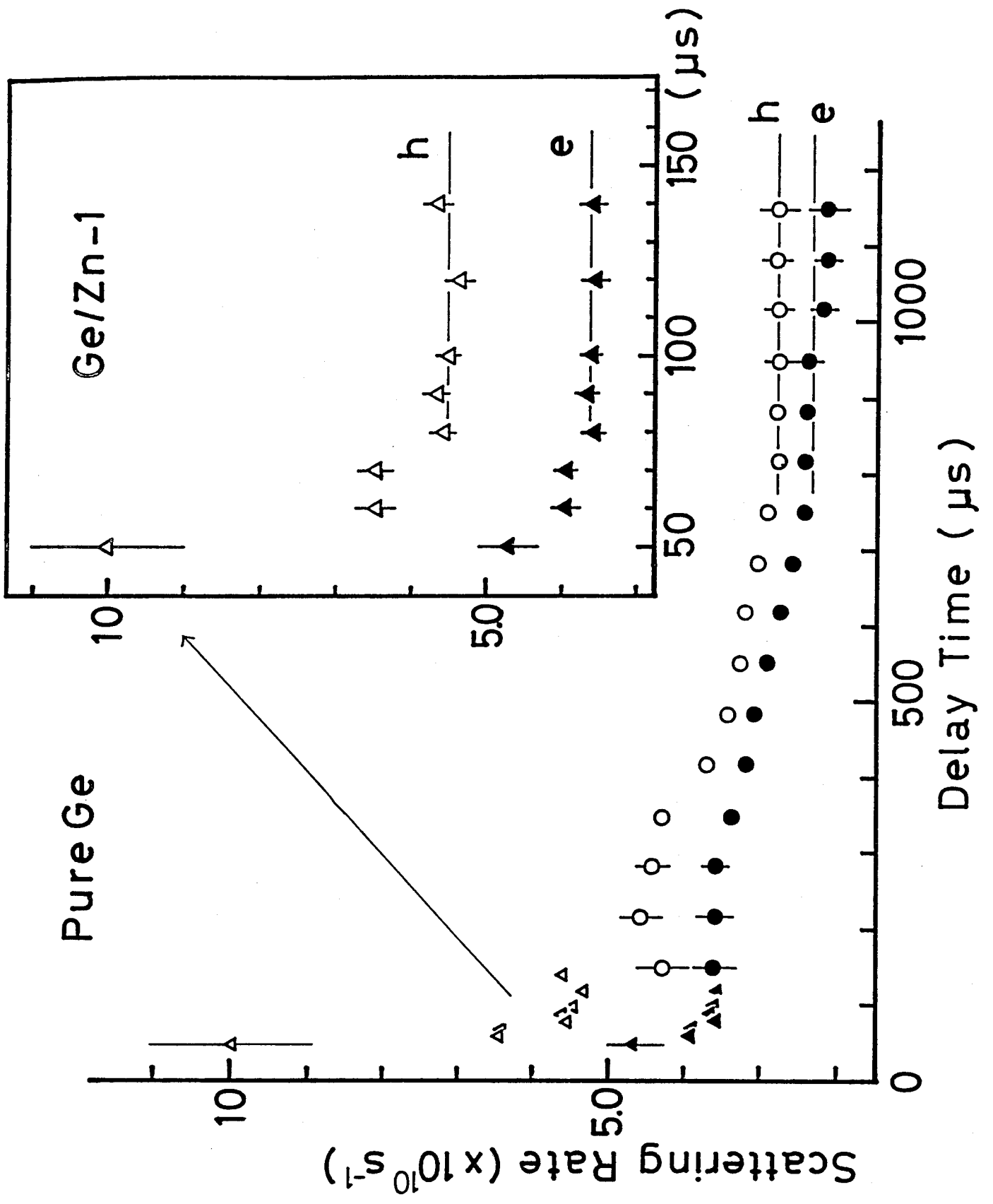


Fig. 52

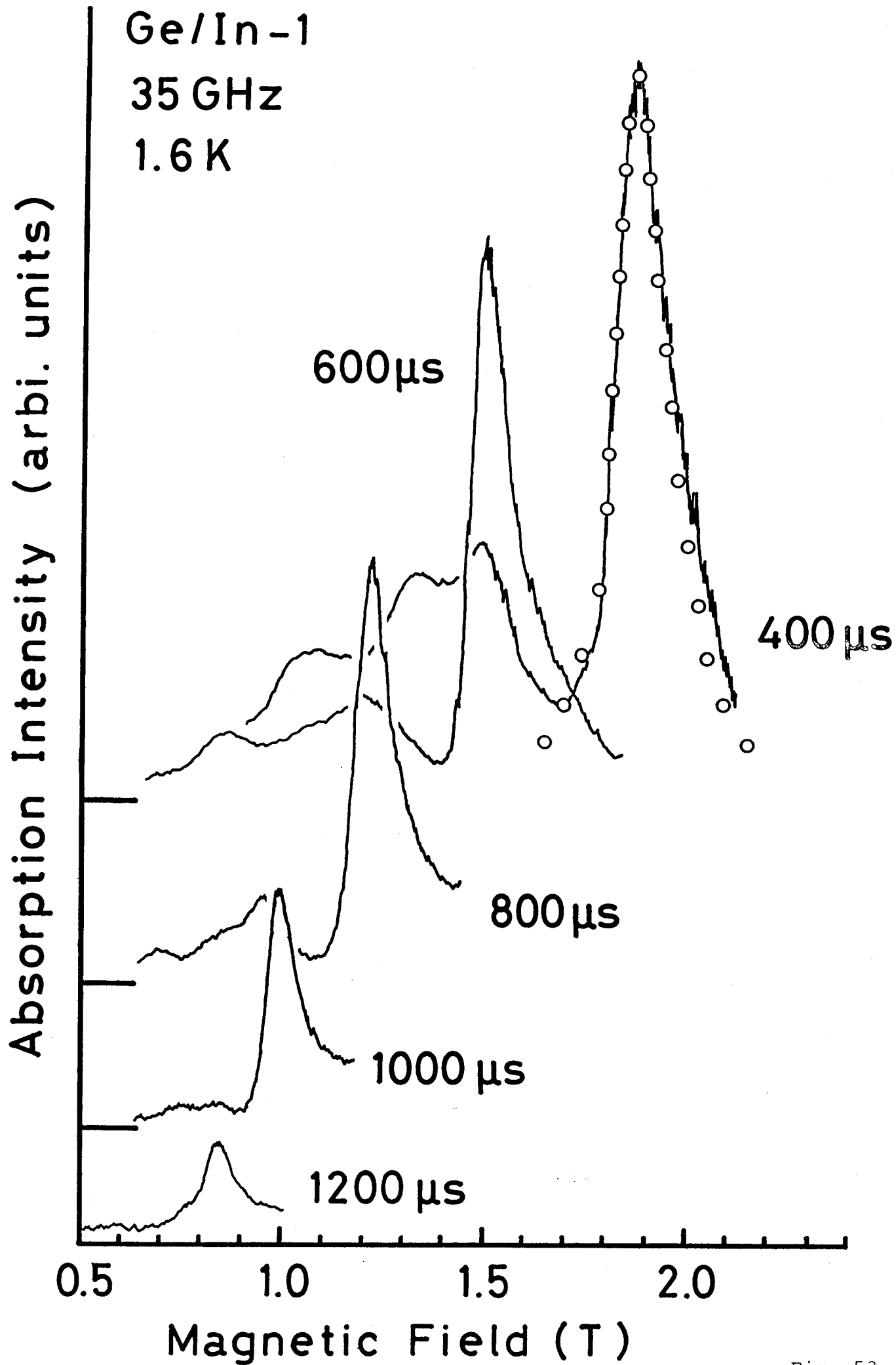


Fig. 53

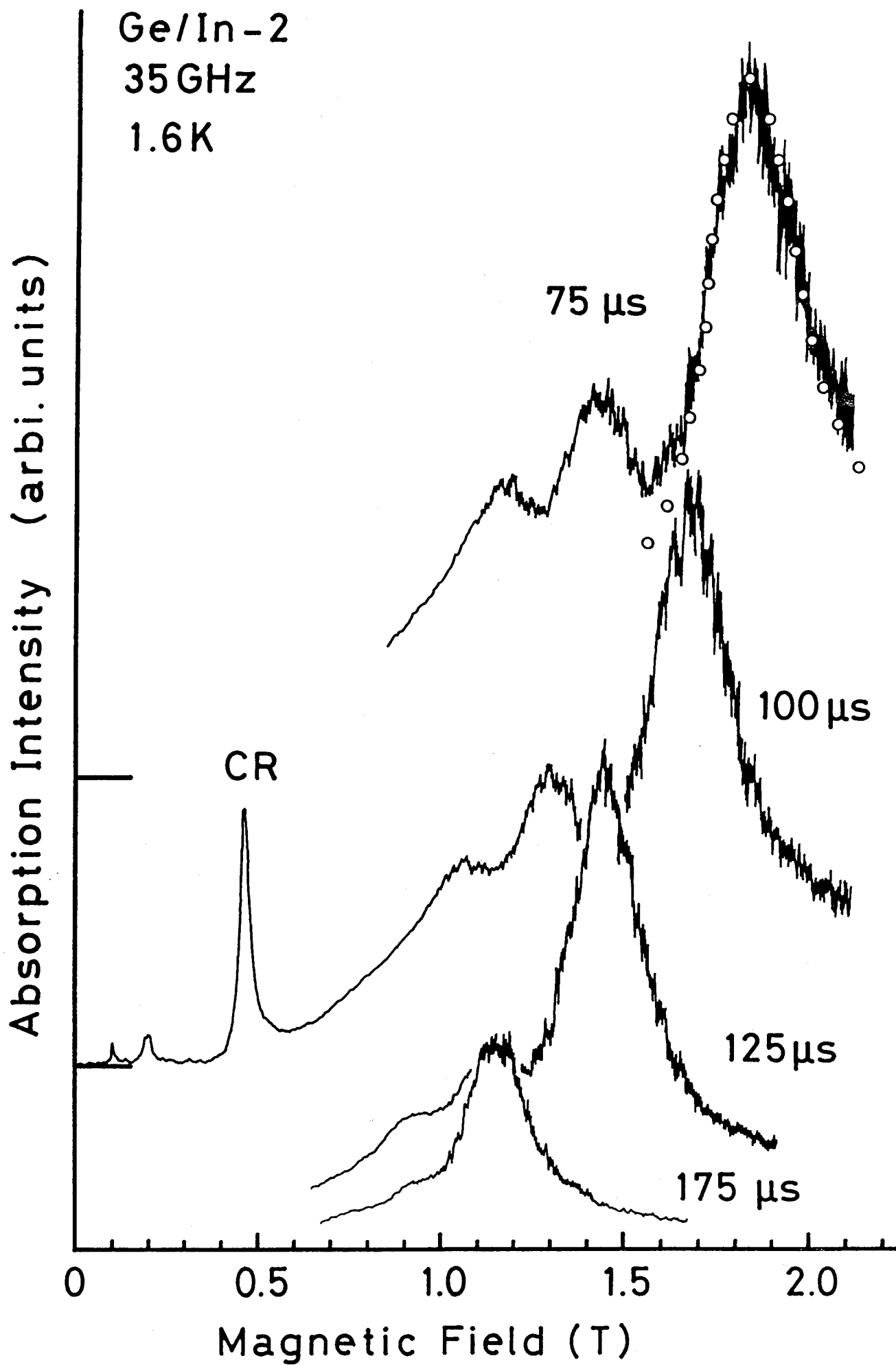


Fig. 54

1.6 K 35GHz

▲ Ge/In-1

△ Ge/In-2

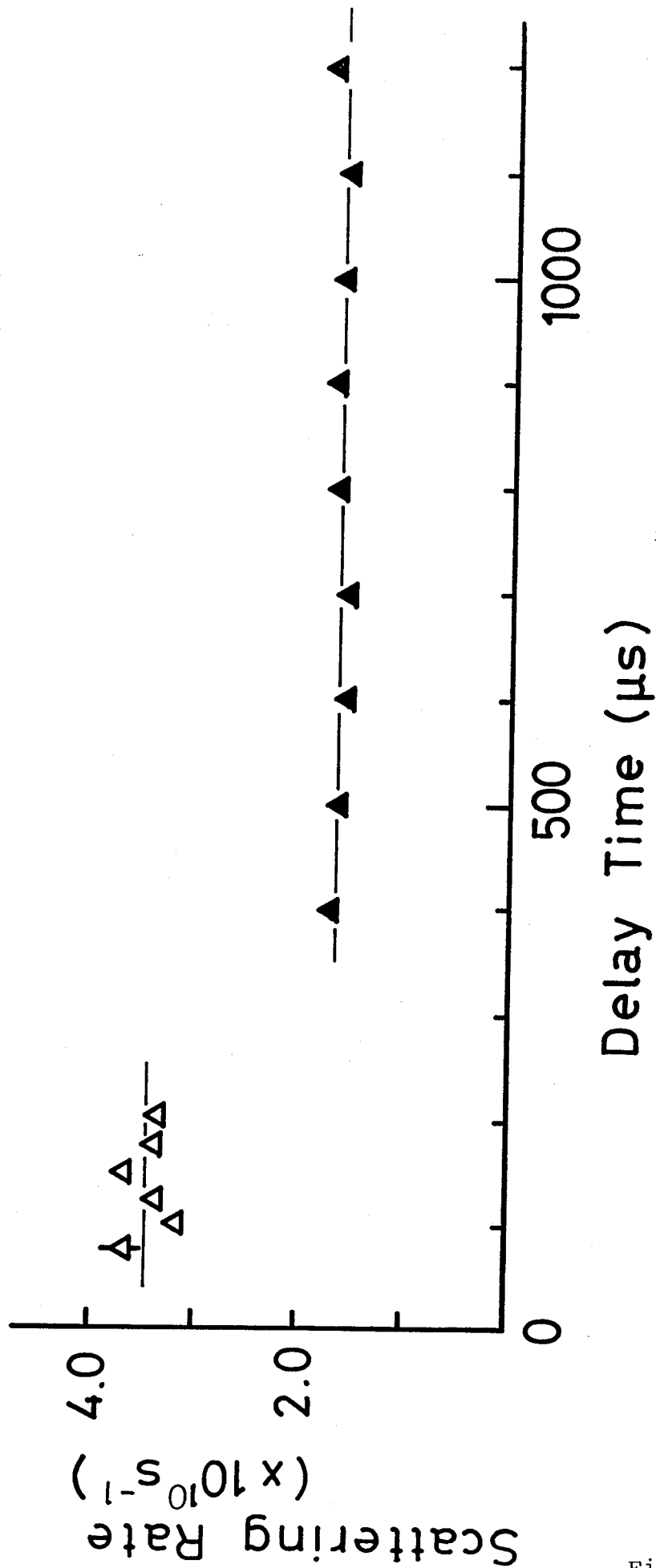


Fig. 55

Ge/Be 722 - 21.5

35 GHz

1.6 K

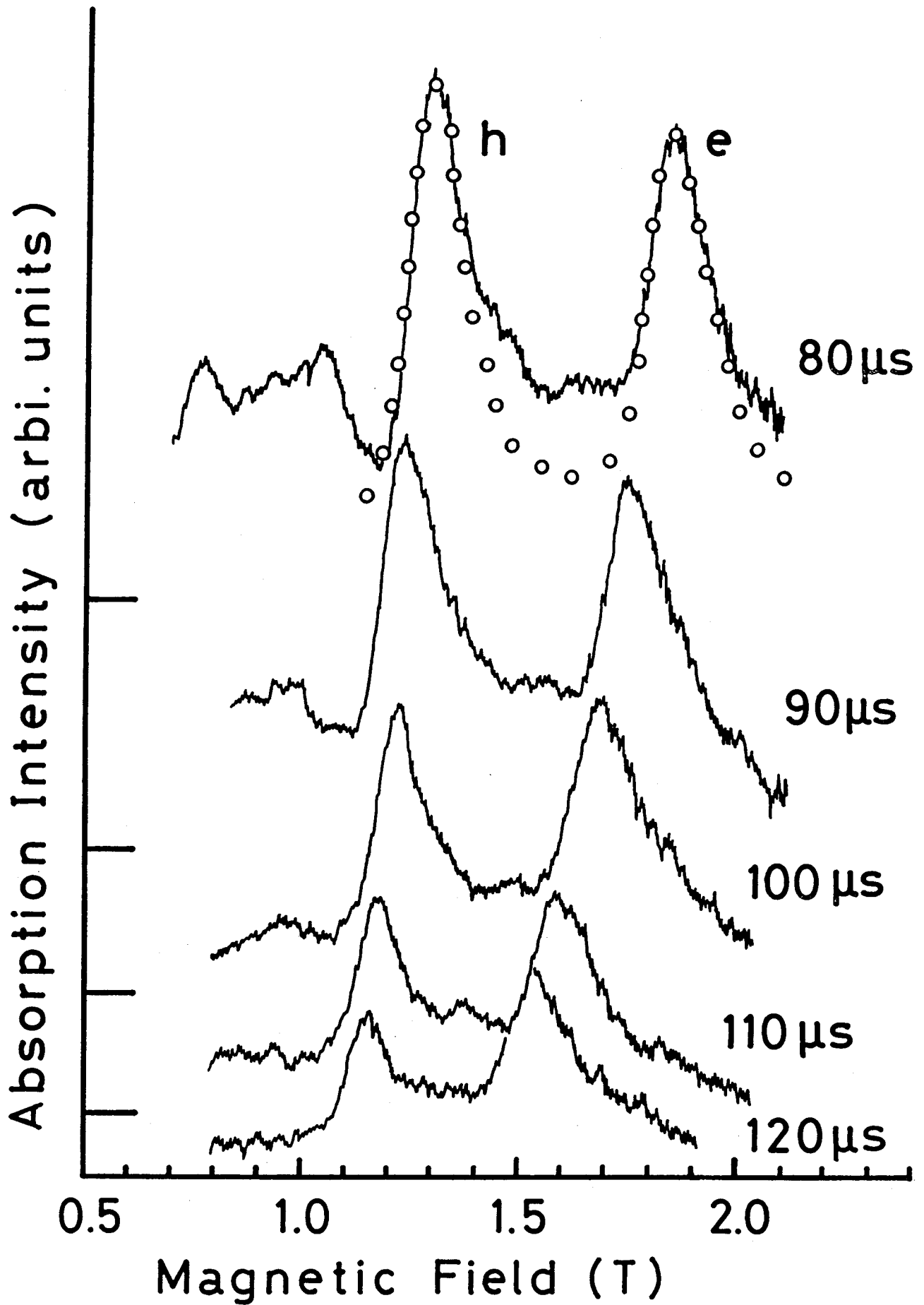


Fig. 56

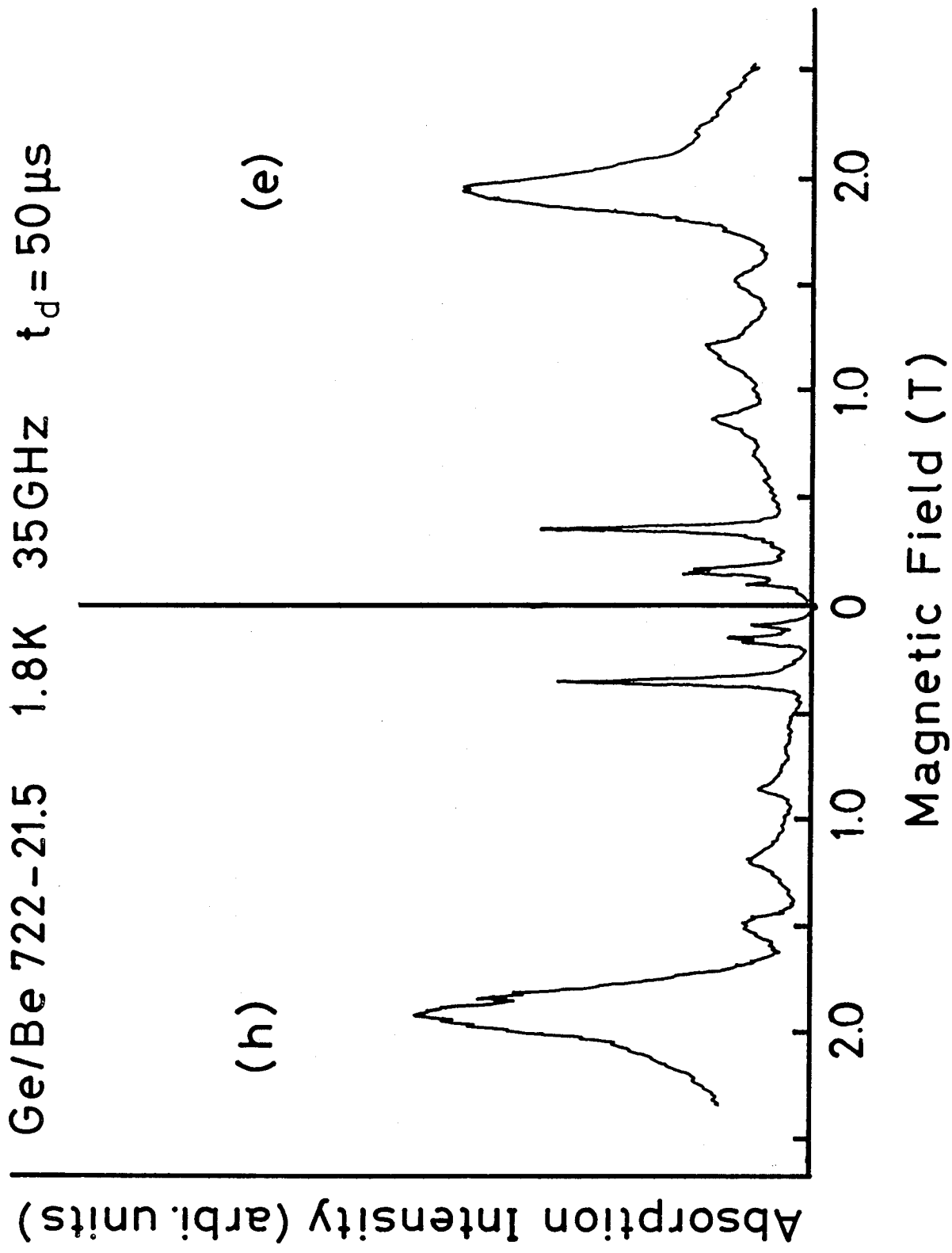


Fig. 57

Ge/Be 722-21.5 1.6 K 35 GHz

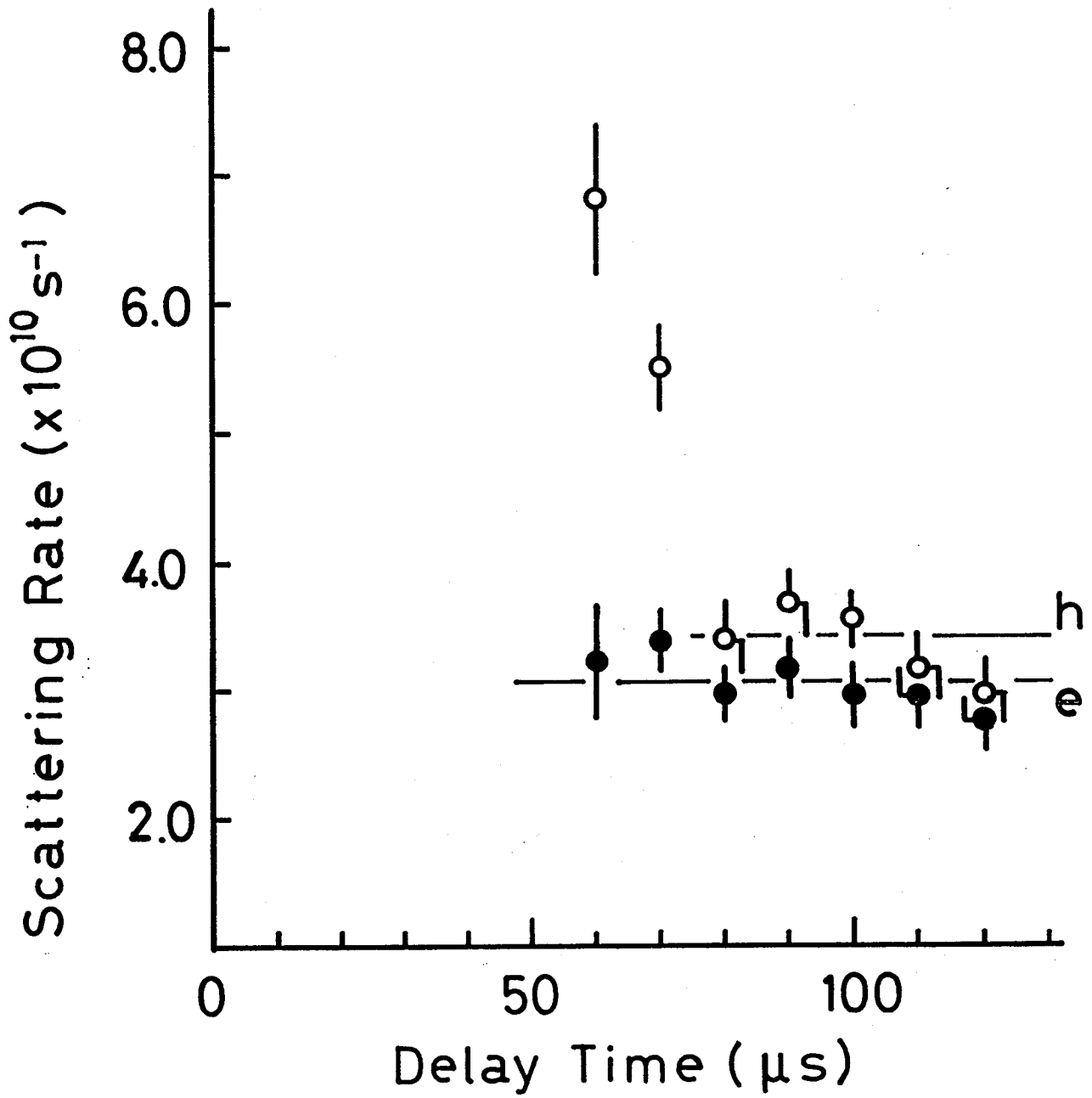


Fig. 58

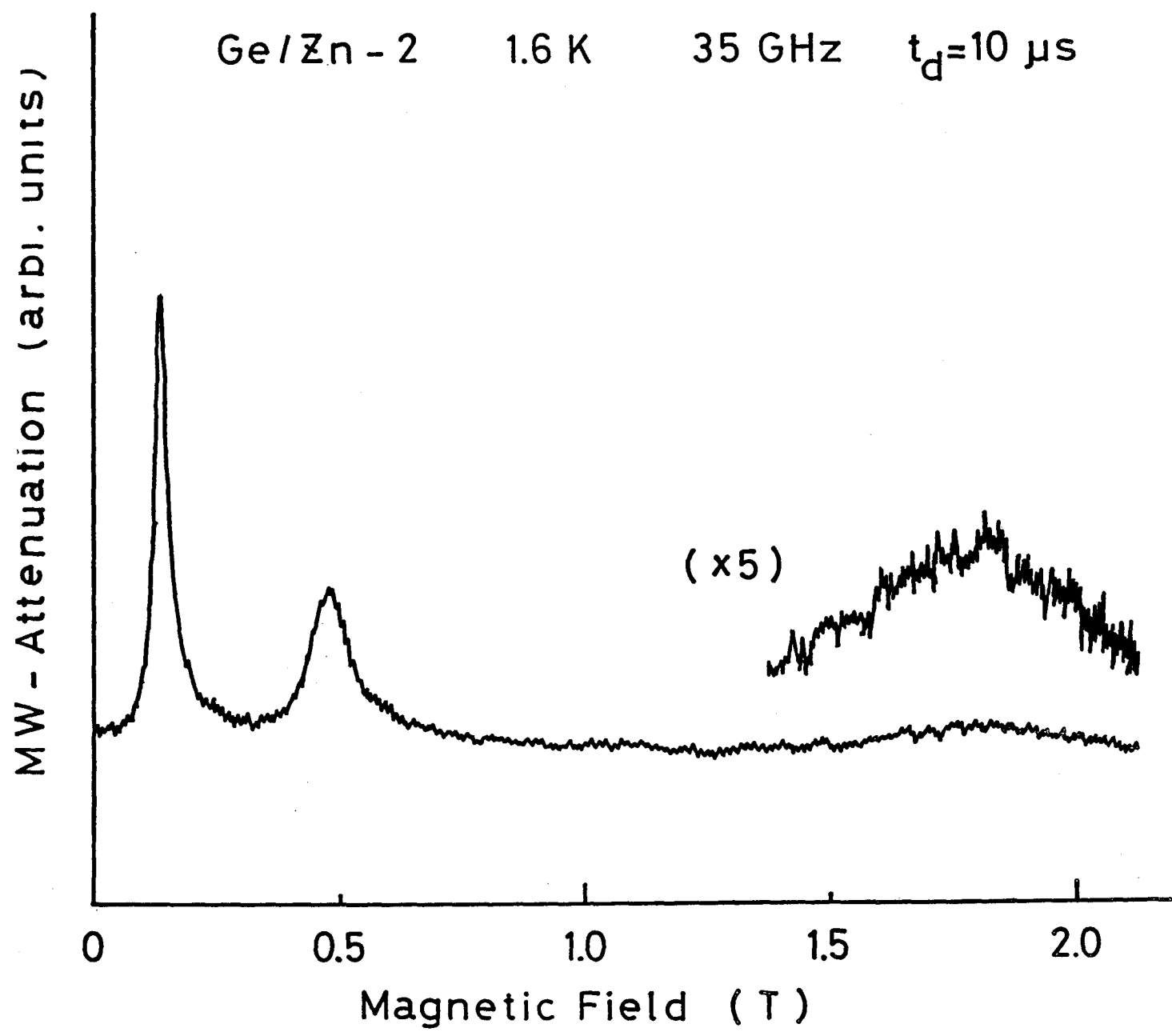


Fig. 59

Ge/Zn-1

1.6 K

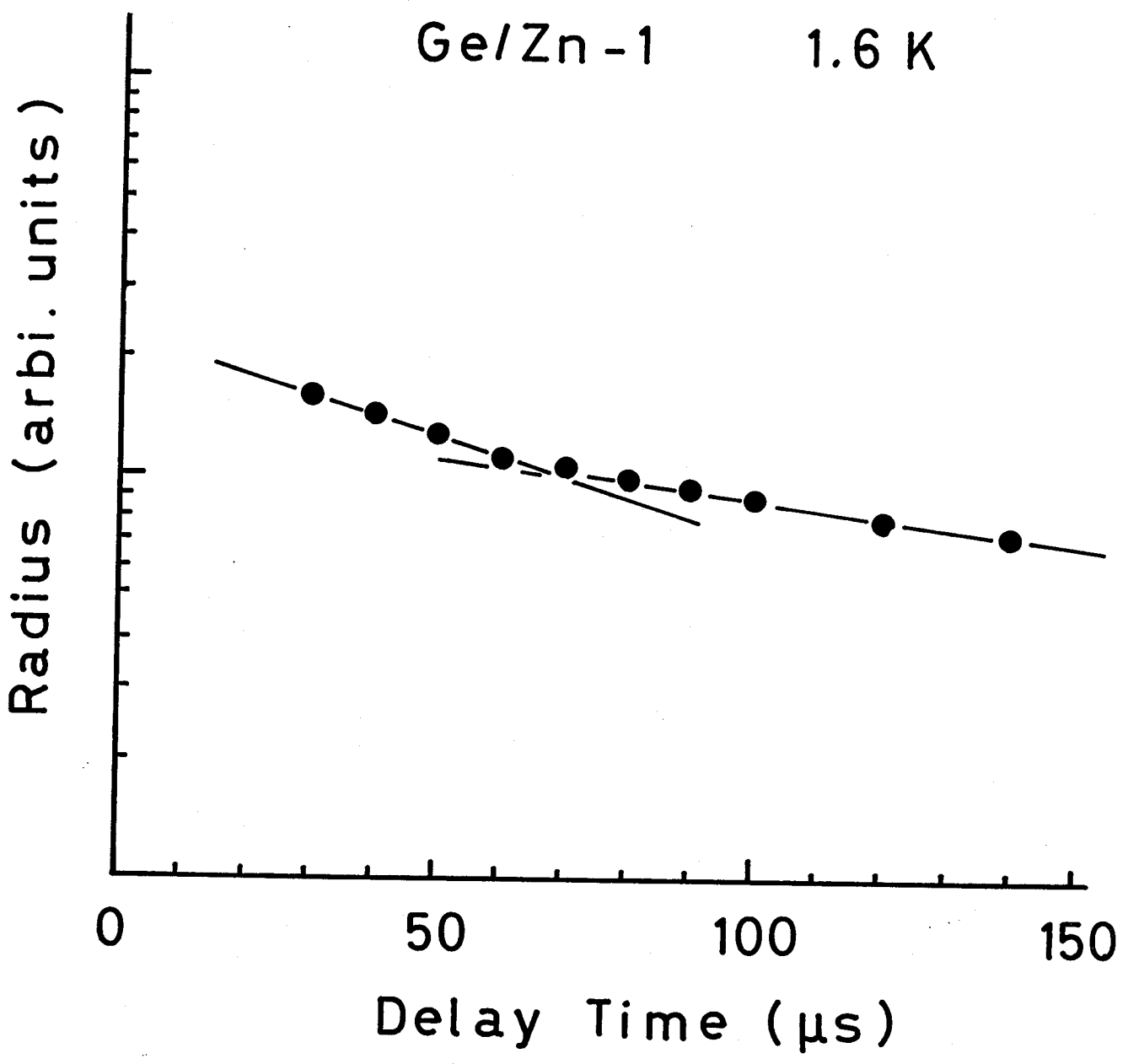


Fig. 60

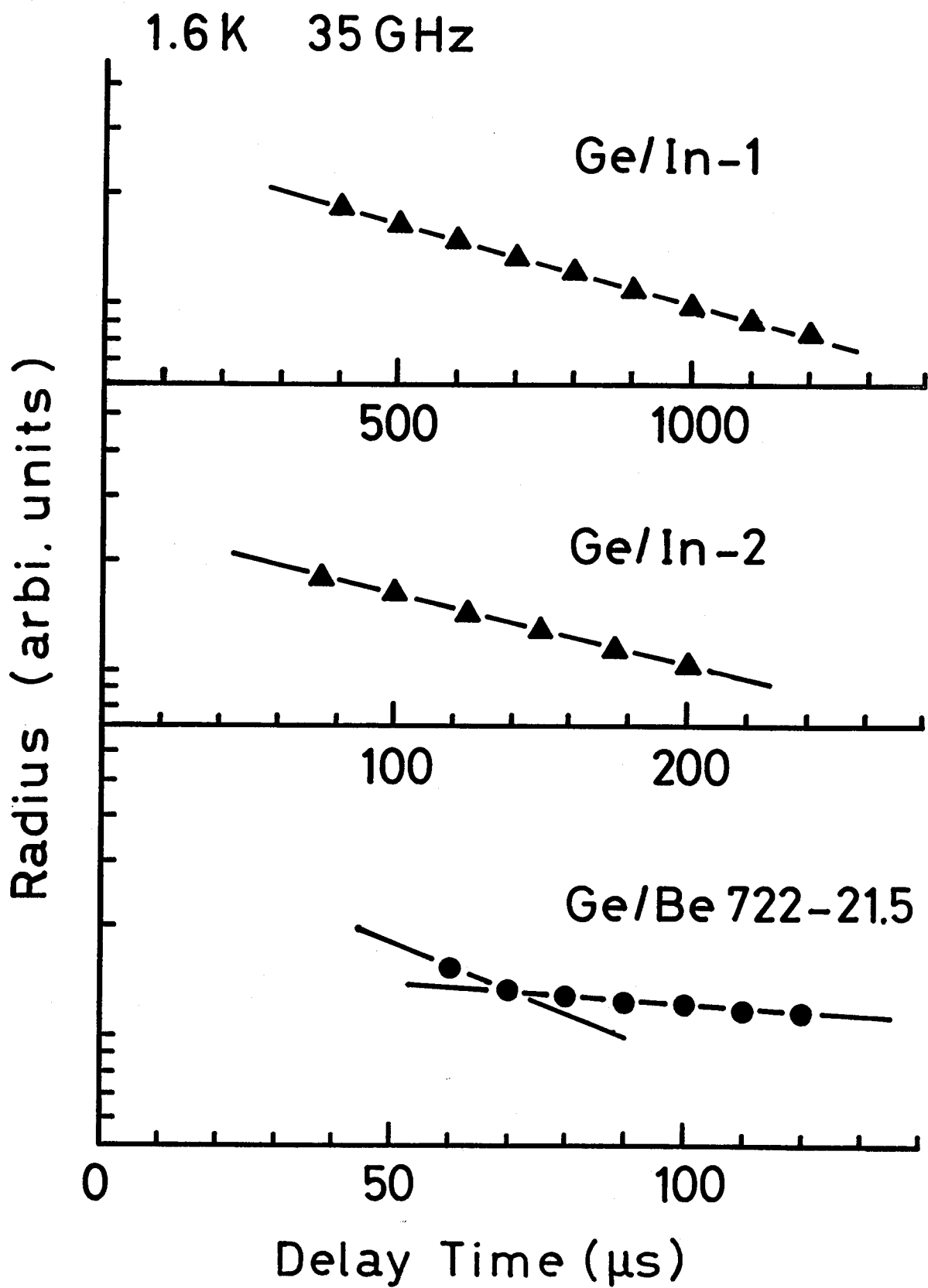


Fig. 61

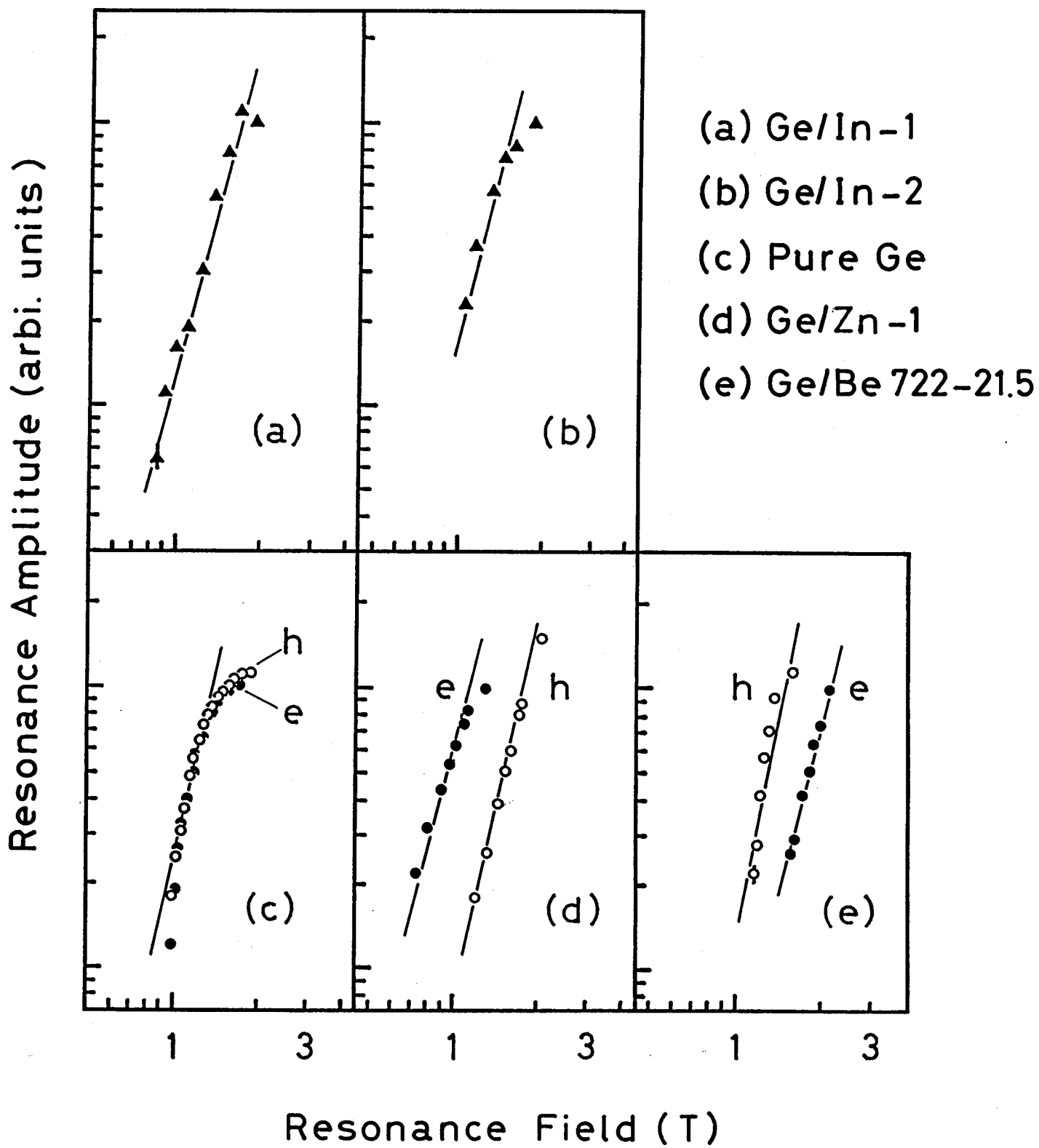


Fig. 62

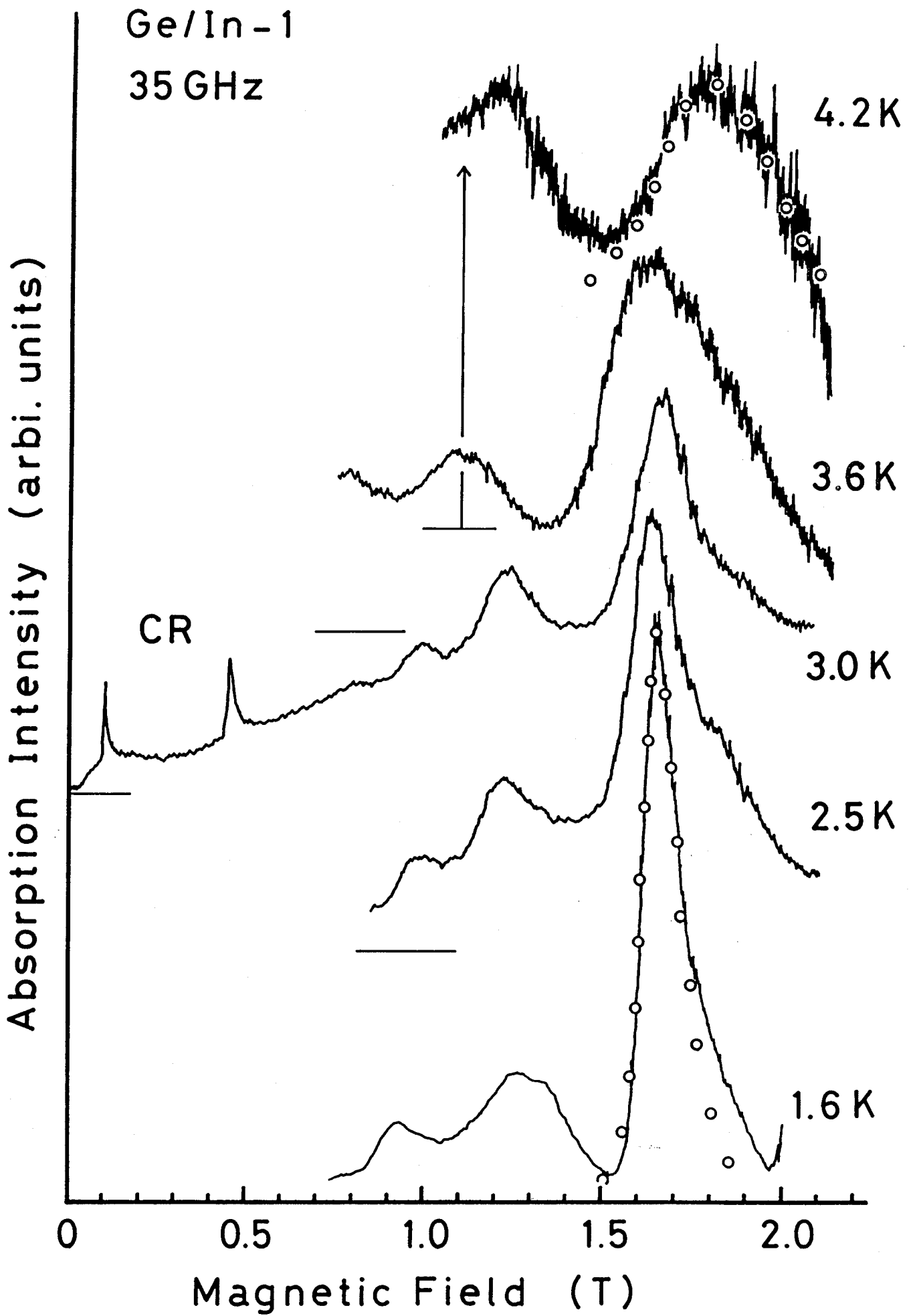


Fig. 63

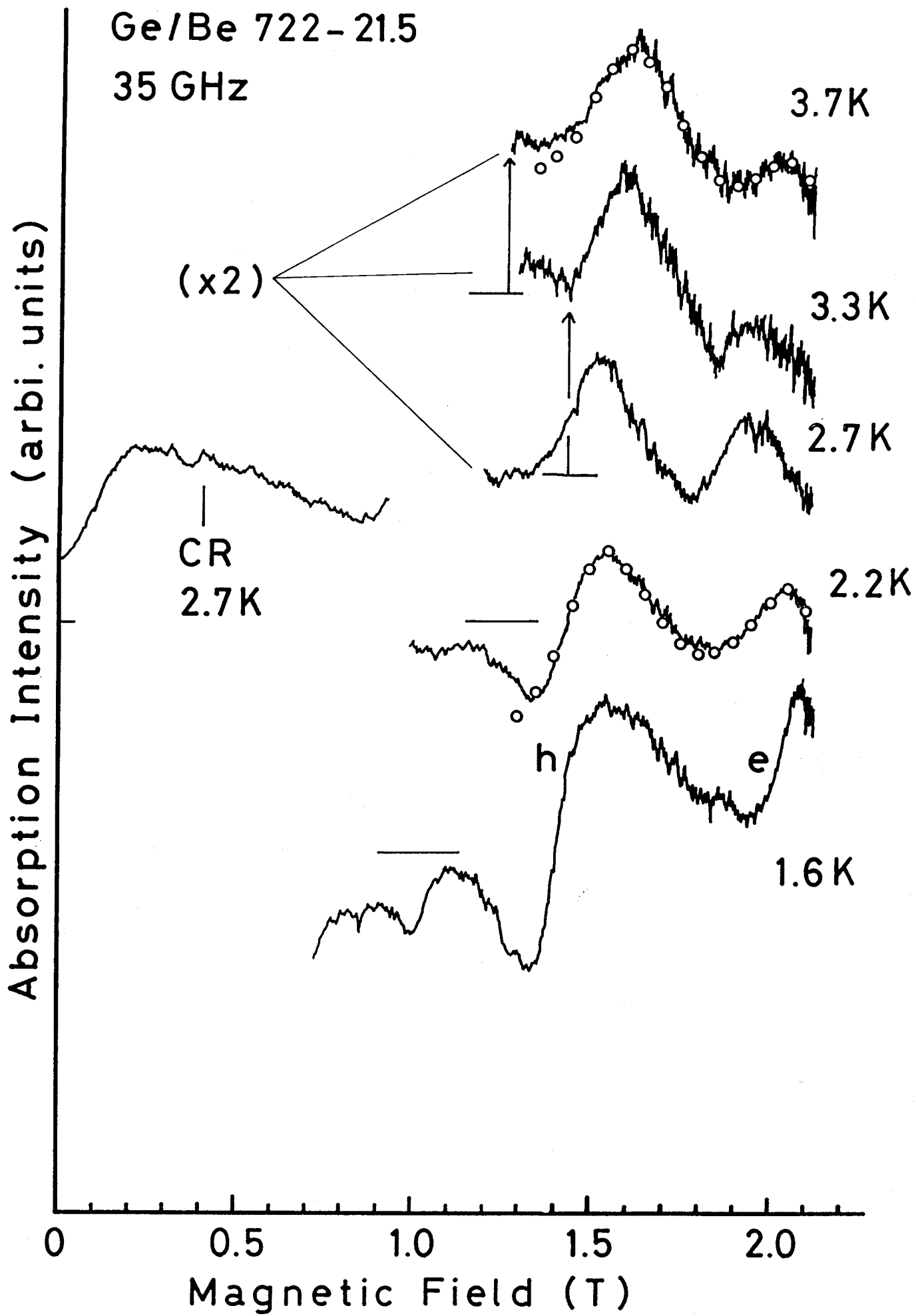


Fig. 64

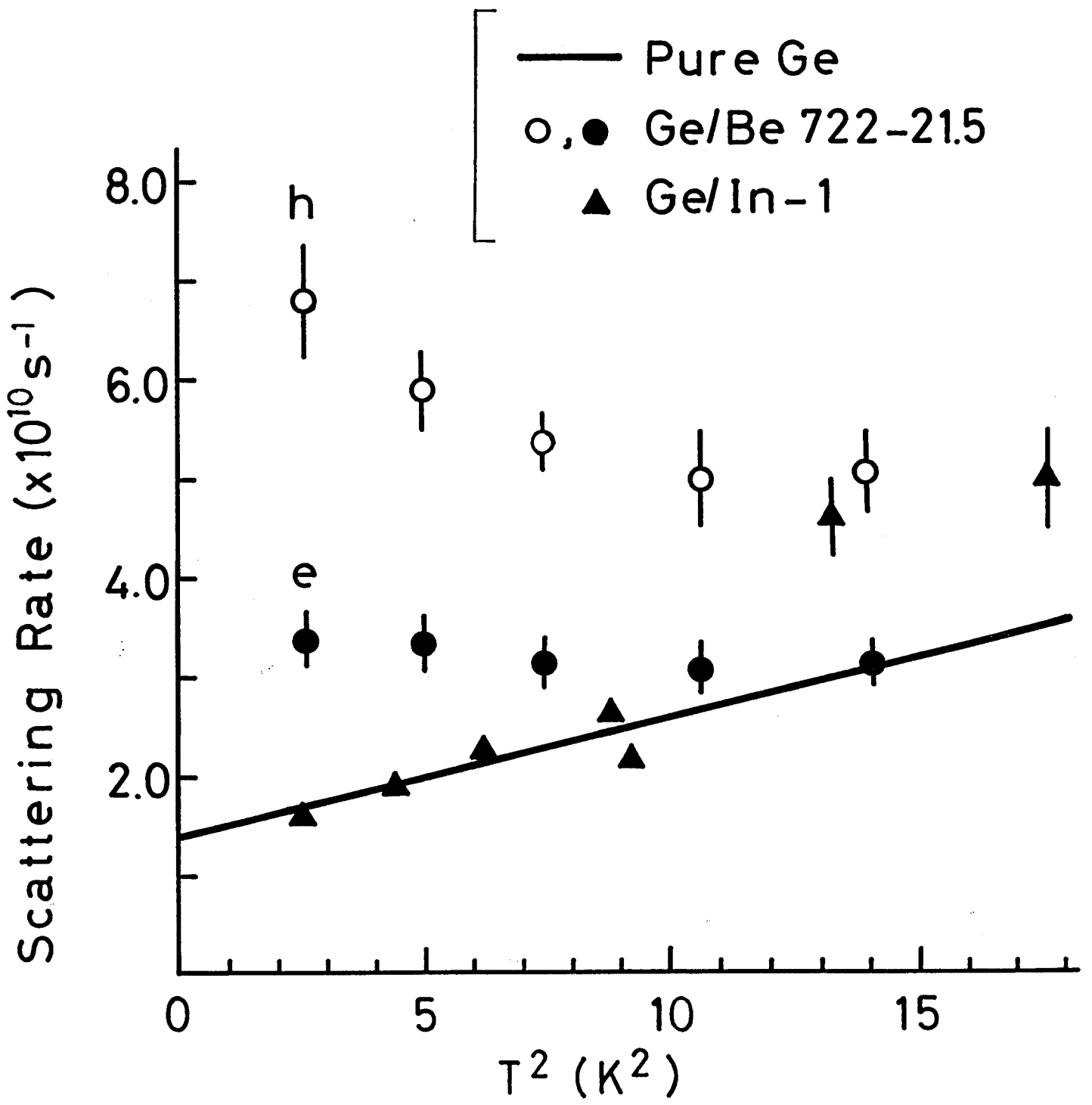


Fig. 65

Ge/Be 722-21.5      35 GHz

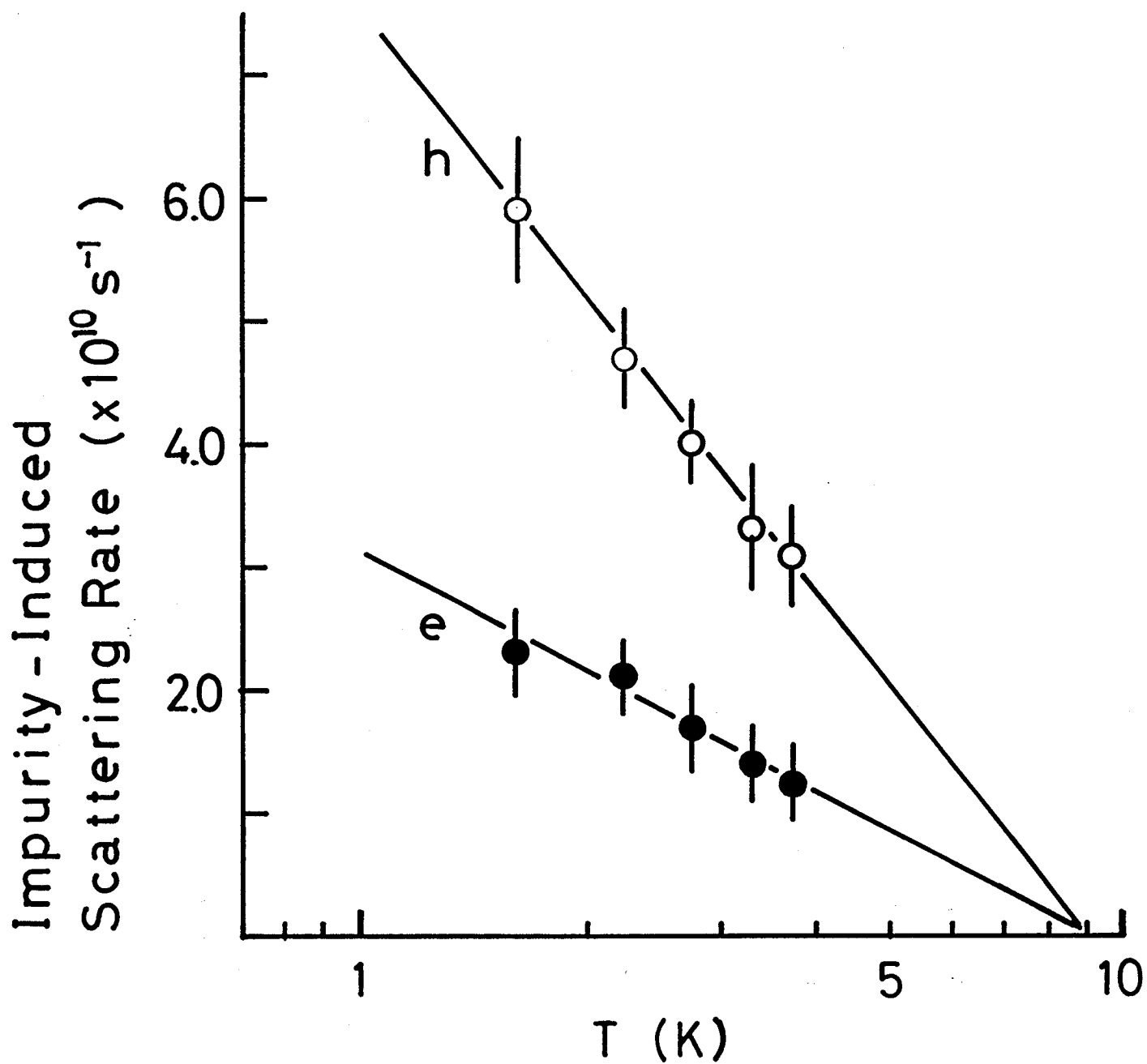


Fig. 66

Pure Ge 220  $\mu\text{m}$  (1360GHz)

Absorption Intensity (arbi. units)

4.2 K

1.8 K

0 1 2 3 4

Magnetic Field (T)

Fig. 67

$E_d + E_u/3 - a$	$E_u$	$ b $	$ d $
$-2.0 \pm 0.5$	$16.2 \pm 0.4$	$1.8 \pm 0.3$	$3.7 \pm 0.4$

Table 1 Deformation potentials in Ge in unit of eV. <sup>36)</sup>

Sample name	Dopant	Concentration (cm <sup>-3</sup> )	Classification and binding energies (meV)	Supplier
Ge/In-1	In	$6.0 \times 10^{13}$	single acceptor 11.2 <sup>73)</sup>	Toshiba
Ge/In-2		$3.7 \times 10^{14}$		
Ge/In-3		$1.8 \times 10^{15}$		
Ge/Be 722-21.5	Be	$4.5 \times 10^{13}$	double acceptor 1st. 24.77, 24.87 <sup>70)</sup> 2nd. 58.02 <sup>70)</sup>	Haller
Ge/Be 727-15.0		$1.0 \times 10^{15}$		
Ge/Zn-1	Zn	$1.2 \times 10^{14}$	double acceptor 1st. 32.98 <sup>71)</sup> 2nd. 86.514 <sup>72)</sup>	Toshiba
Ge/Zn-2		$2.1 \times 10^{15}$		
Ge/Zn-3		$3.2 \times 10^{16}$		

Table 2 List of doped Ge samples

Impurity	Be	Zn <sup>116</sup> )	In
Capture cross section (cm <sup>2</sup> )	$3.5 \times 10^{-15}$	$2.5 \times 10^{-15}$	$1.5 \times 10^{-16}$

Table 3 Free-exciton capture cross section  $\sigma_x$  by Be, Zn and In impurities obtained at 4.2 K.

Impurity	Be	Zn	In
Induced recombination rate per impurity ( $\text{cm}^3 \text{s}^{-1}$ )	$7.2 \times 10^{-10}$	$2.6 \times 10^{-10}$	$2.2 \times 10^{-11}$

Table 4 Induced recombination rate per impurity in SCEHL at 1.8 K.

Impurity	Be	Zn	In
Induced scattering rate per impurity ( $\text{cm}^3 \text{s}^{-1}$ )	$4.2 \times 10^{-4}$ (e,h)	$1.0 \times 10^{-4}$ (e) $2.3 \times 10^{-4}$ (h)	$4.9 \times 10^{-5}$

Table 5 Induced scattering rate per impurity in SCEHL at 1.6 K.  
Active polarizations in the separated modes are indicated as e and h.